JETP Letters, Vol. 75, No. 1, 2002, pp. 1–4. Translated from Pis'ma v Zhurnal Éksperimental'noĭ i Teoreticheskoĭ Fiziki, Vol. 75, No. 1, 2002, pp. 3–6.

Clusters in the Arrival Directions of 2×10^{17}-eV Cosmic Rays Detected at the Yakutsk EAS Array

A. V. Glushkov

Institute of Cosmophysical Research and Aeronomy, Yakut Research Center, Siberian Division, Russian Academy of Sciences, pr. Lenina 31, Yakutsk, 677891 Russia

e-mail: a.v.glushkov@ikfia.ysn.ru

Received November 26, 2001

Arrival directions of $(1.3–4) \times 10^{17}$-eV cosmic rays detected for zenith angles $\theta \le 53°$ at the Yakutsk array from 1974 to 2001 are analyzed. These directions exhibit numerous clusters correlating with the supergalactic plane.

PACS numbers: 98.70.Sa; 95.85.Ry

1. Primary cosmic radiation (PCR) of ultrahigh energies ($E_0 > 4 \times 10^{17}$ eV) is thought to consist primarily of charged particles, protons, and nuclei of various chemical elements. These charged particles are strongly mixed by the magnetic field of the galaxy and distributed almost isotropically over the celestial sphere. For this reason, it is difficult to find the local sources of PCR. The above concept can be questioned because the PCR content has not been measured directly yet and conclusions based on extensive air shower (EAS) data are ambiguous and inconsistent.

As was reported in [1, 2], the arrival directions of PCR with energies $E_0 > 4 \times 10^{17}$ eV exhibit numerous groups of showers in narrow solid angles. The distribution of these groups over the celestial sphere has a small-scale ordered structure that cannot be attributed to stochastic statistical processes. In my opinion, this structure can be attributed to the distribution of extragalactic point sources generating neutral particles of PCR. Some new evidence supporting this opinion will be presented below.

2. Characteristics under investigation and discussion. We analyze the small-scale anisotropy, i.e., local inhomogeneities ~5–10° in PCR, for $(1.3–4) \times 10^{17}$-eV EASs detected with zenith angles satisfying the condition $\cos\theta \ge 0.6$ at the Yakutsk array from 1974 to 2001. The analysis covers EASs whose arrival directions were determined at ≥4 stations and whose axes fell within the central array circle with a radius ≤1000 m. These events give small errors in the basic EAS parameters (direction and coordinates of the axis, E_0, etc.). The primary-particle energy E_0 was determined from the relationships

$$E_0 = (4.8 \pm 1.6) \times 10^{17} (\rho_{s,600}(0°))^{1.0 \pm 0.02} \text{ [eV]}, \quad (1)$$

$$\rho_{s,600}(0°) = \rho_{s,600}(\theta) \times \exp((\sec\theta - 1) \times 1020/\lambda_\rho) \text{ [m}^{-2}\text{]}, \quad (2)$$

$$\lambda_\rho = (450 \pm 44) + (32 \pm 15)\log(\rho_{s,600}(0°)) \text{ [g/cm}^2\text{]}, \quad (3)$$

where $\rho_{s,600}(\theta)$ is the charged-particle density measured by ground-based scintillation detectors at a distance of 600 m from the shower axis.

We analyzed 36 825 showers in five energy ranges with a step of $\Delta \log E_0 = 0.1$. In each of these ranges, we took seven independent samples of approximately equal size from ≈1000 events, whose only difference from each other is that their axes fell within different rings inside the central circle of the array. The presence of local shower groups in the celestial sphere was checked separately for each of the $5 \times 7 = 35$ samples as follows. We determined all "neighbors" spaced from the arrival direction of each shower by the angular distance $d \le 3°$. If this circle included $n \ge 3$ showers, their coordinates were averaged and these averaged coordinates were attributed to new points, referred to as nodes, which were used for further analysis.

Moreover, analyzing each of the five energy ranges separately, we sought those $m \ge 2$ nodes in any sample among the seven whose centers are spaced by $d \le 3°$. If such nodes were found, the arrival directions of all showers entering them were averaged and the averaged direction was attributed to a larger node, referred to as a cluster, which was used for further analysis. Figure 1 shows the map of cluster positions in the developed celestial sphere for showers of the energies $E_0 = 10^{17.2–17.}$ eV in galactic coordinates. Equal areas in the map correspond to equal sky areas. The solid line corresponds to the local supercluster of galaxies (supergalaxy) with the North Pole coordinates $\alpha = 286.2°$ and

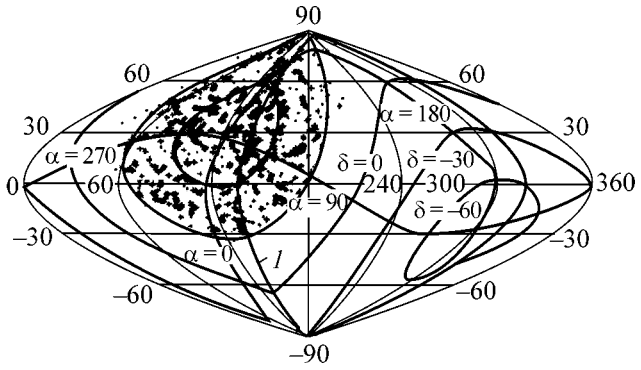

Fig. 1. Map of nodes and clusters for 1882 showers with $E_0 = 10^{17.2–17.3}$ eV and zenith angles $\theta \le 53°$ in galactic coordinates as determined from the Yakutsk EAS array data: (•) nodes with $m = 1$, (+) clusters with $m \ge 2$ nodes in circles of the radius $d = 3°$, and (*1*) supergalactic disk.

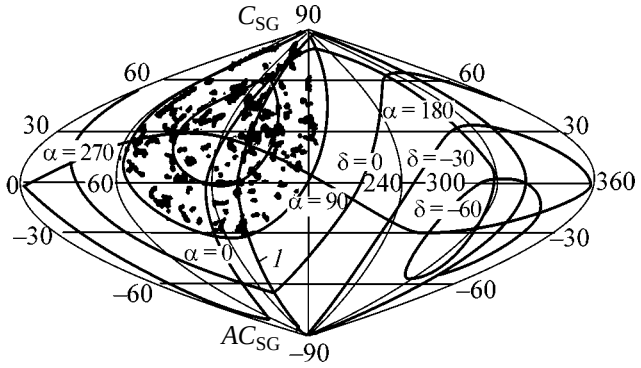

Fig. 2. Map of the clusters which include 2969 showers and are general for five groups with $E_0 = 10^{17.1–17.2}$, $10^{17.2–17.3}$, $10^{17.3–17.4}$, $10^{17.4–17.5}$, and $10^{17.5–17.6}$ eV in galactic coordinates; line *1* is the supergalactic disk, whereas C_{SG} and AC_{SG} are the center and anticenter of the supergalaxy, respectively.

$\delta = 14.1°$. For convenience of data recognition, equatorial coordinates are also shown. The points and crosses are the nodes with $m = 1$ and clusters with $m \ge 2$, respectively.

It is remarkable that most clusters come together at local clusters. A similar pattern is also observed for other PCR energies. The positions of clusters with different energies frequently coincide with each other. Figure 2 shows the map of the clusters common to all five above groups with $E_0 = 10^{17.1–17.2}$, $10^{17.2–17.3}$, $10^{17.3–17.4}$, $10^{17.4–17.5}$, and $10^{17.5–17.6}$ eV. They were found when 10–18 nodes from 35 independent samples, each including ≈1000 showers, had coinciding angular coordinates. The density of clusters near the galactic disk is lower than the density at high latitudes. In addition, the number of events in the $|b_G| \le 10°$ zone is much fewer than that near the same zone near the supergalactic disk.

The negative and positive correlations of clusters with the galactic and supergalactic disks, respectively, are evident in Fig. 3, which shows the distributions of the 2969 showers (clusters in Fig. 2) over their arrival latitudes (with a step of $\Delta b = 2°$) in galactic (b_G) and supergalactic (b_{SG}) coordinates. The lines are the Monte-Carlo calculations for the isotropic flux.

Figure 3a exhibits a pronounced dip for $|b_G| \le 10°$. The deficit of events in this region is $(395 – 625)/\sqrt{625} = 9.2\sigma$. In contrast, Fig. 3b exhibits a series of statistically significant peaks. Peak *2* is immediately in the supergalactic disk, it is over the expected line by $\approx 6.6\sigma$, and it is even more significant with the inclusion of dips lying on each of its sides. A number of other peaks lie symmetrically about the supergalactic plane. In particular, peaks *1* and *3*, *4* and *5*, and *6* and *7* are spaced from this plane by angles of ≈6.5°, ≈20°, and ≈33°, respectively. In principle, all the peaks marked by the arrows do not contradict the discrete division with a step of ≈6.5°.

The probability that each of the distributions in Fig. 3 is random is less than 10^{-6}. These results can be treated as evidence of the extragalactic origin of the PCR fraction associated with the clusters. The galaxy likely only absorbs this radiation, and this absorption is more intense in the disk. Other significant peaks and dips in Fig. 3b apparently indicate the complicated and inhomogeneous structure of extragalactic space, where the PCR sources forming clusters are located.

The events primarily contributing to peaks *1–3* will be analyzed in more detail. Figure 4 shows the distributions of the showers in these peaks in the ranges (*1*) $6° < b_{SG} < 10°$, (*2*) $–2° < b_{SG} < 4°$, and (*3*) $–12° < b_{SG} < –6°$over the supergalactic longitude (with a step of $\Delta l_{SG} = 2°$) measured counterclockwise from the axis directed to the anticenter. The most pronounced peaks are at $l_{SG} \approx$ (*a*) 76°, (*b*) 101°, (*c*) 117°, (*d*) 121°, (*e*) 127°, (*g*) 140°, (*f*) 145°, and (*h*) 171°. The positions of some peaks in the upper panel of Fig. 4 almost coincide with those in the middle and lower panels, among others. In addition, these peaks (along with others less significant) fit into a series with a step of ≈6.5°.

We emphasis one intriguing point. Figure 3c shows data from [3], where peaks *1–3* were also observed for $E_0 \ge 10^{19}$ eV. It is surprising that even individual details of the distributions for $E_0 \approx (1.3–4) \times 10^{17}$ eV and $E_0 \ge 10^{19}$ eV in supergalactic coordinates coincide with each other in the region $|b_{SG}| \le 30°$.

It was also shown in [3] that the relatively high densities of the clusters of galaxies and quasars, which are definitely associated with the large-scale structure of the universe, are observed in the regions of peaks *1–3*. The splitting of the arrival directions of PCR into the

peaks in Figs. 3b, 3c, and 4 can be treated as corroboration of the adiabatic ("pancake") Zel'dovich theory [4], where the geometry of the metagalactic structures is characterized by the presence of giant plane formations separated by large (~10^5 Mps^3) volumes free of galaxies. Einasto *et al.* [5] thought that this structure was of the "three-dimensional checkerboard" type.

According to Yakutsk EAS array data [6], the total flux of PCR with $E_0 \approx (1\text{–}4) \times 10^{17}$ eV does not exhibit statistically significant anisotropy and the amplitude and phase of the first right-ascension harmonic found by traditional harmonic analysis are equal to $(0.45 \pm 0.55)\%$ and $\varphi_1 = 192° \pm 70°$, respectively. The latter, despite the large uncertainty attributed to the PCR anisotropy, points to the supergalactic center (C_{SG} in Fig. 2).

The above results, along with the results from [6], can be explained by assuming that PCRs have two components. One of them is more intense than the other by a factor of ≈10 and likely includes charged particles strongly mixed by the magnetic field of the galaxy. The second component forming clusters apparently consists of neutral particles of extragalactic origin and, even being strongly diluted by the isotropic flux of the first component, affects the results presented in [6].

3. The above data indicate that some fraction of cosmic rays with $E_0 \approx (1\text{–}4) \times 10^{17}$ eV forms numerous clusters within solid angles with $d \le 3°$ (see Figs. 1, 2). These clusters negatively and positively correlate with the galactic and supergalactic disks, respectively (see Fig. 3). It can be assumed that the clusters point to some extragalactic pointlike sources of PCR, and these sources are definitely associated with the large-scale structure of the universe.

The primary particles forming the clusters are most likely neutral. Otherwise they would not correlate in direction with the sources of their origin because of the motion in the magnetic fields of the supergalaxy and, particularly, the galaxy. The fraction of these particles in the total PCR flux is approximately equal to 2969/36825 ≈ 0.08 and is likely close to unity for $E_0 \approx (1\text{–}4) \times 10^{17}$ eV and $E_0 \ge 10^{19}$ eV, respectively [2, 3, 7].

Events not involved in the clusters are distributed almost isotropically over the celestial sphere. This fraction of PCR likely consists of charged particles (protons and nuclei of various chemical elements) propagating through the galaxy due to diffusion. One of the intense sources is located near the galactic center [8–10]. It is still very difficult to observe other sources of charged particles, because their positions are strongly smeared by the magnetic field of the galaxy.

This work was supported by the Ministry of Sciences of the Russian Federation (support for the Yakutsk complex EAS array included under project no. 01-30 in the "Register of Unique Research and Experimental Instruments of National Significance").

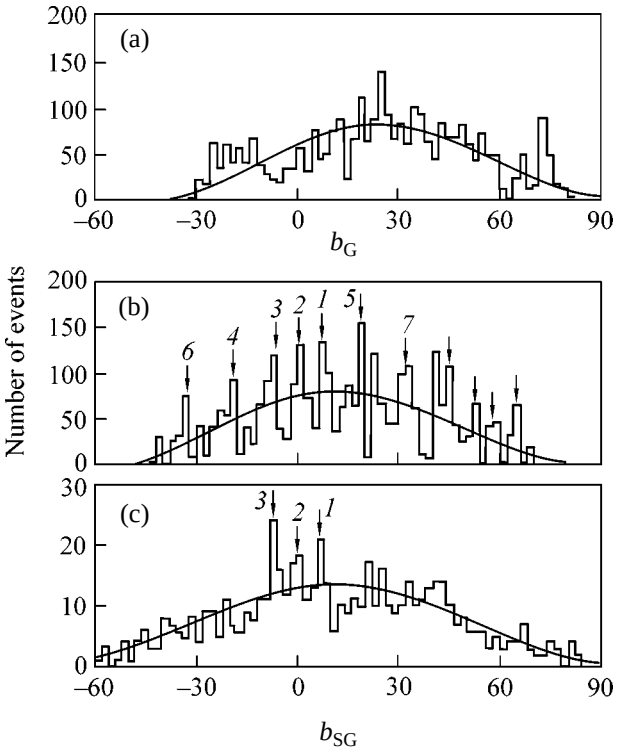

Fig. 3. Distributions of the 2969 showers in clusters shown in Fig. 2 over the latitude of their arrival in (a) galactic and (b) and (c) supergalactic coordinates; (c) data from [3] for EASs with $E_0 \ge 10^{19}$ eV; the lines are the distributions expected for isotropic PCR flux.

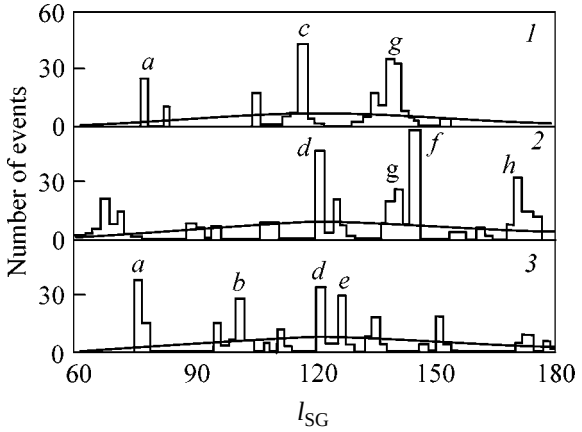

Fig. 4. Distributions of the showers in peaks *1–3* in Figs. 3b and 3c in the ranges (*1*) $6° < b_{SG} < 10°$, (*2*) $-2° < b_{SG} < 4°$, and (*3*) $-12° < b_{SG} < -6°$ over the supergalactic longitude l_{SG}. The most pronounced peaks are at $l_{SG} \approx$ (*a*) 76°, (*b*) 101°, (*c*) 117°, (*d*) 121°, (*e*) 127°, (*g*) 140°, (*f*) 145°, and (*h*) 171°. The lines are the distributions expected for the isotropic PCR flux.

REFERENCES

1. A. V. Glushkov, Pis'ma Zh. Éksp. Teor. Fiz. **48**, 513 (1988) [JETP Lett. **48**, 555 (1988)].
2. A. V. Glushkov and M. I. Pravdin, Pis'ma Astron. Zh. **27**, 577 (2001) [Astron. Lett. **27**, 493 (2001)].
3. A. V. Glushkov, Pis'ma Zh. Éksp. Teor. Fiz. **73**, 355 (2001) [JETP Lett. **73**, 313 (2001)].
4. Ya. B. Zel'dovich, Pis'ma Astron. Zh. **8**, 195 (1982) [Sov. Astron. Lett. **8**, 102 (1982)].
5. J. Einasto *et al.*, Nature **385**, 139 (1997).
6. M. I. Pravdin, A. A. Ivanov, A. D. Krasil'nikov, *et al.*, Zh. Éksp. Teor. Fiz. **119**, 881 (2001) [JETP **92**, 766 (2001)].
7. A. V. Glushkov and M. I. Pravdin, Zh. Éksp. Teor. Fiz. **119**, 1029 (2001) [JETP **92**, 887 (2001)].
8. N. Hayashida, M. Nagano, D. Nishikawa, *et al.*, Astropart. Phys. **10**, 303 (1999).
9. M. Teshima, M. Shikawa, M. Fukushima, *et al.*, in *Proceedings of the 27th International Cosmic Ray Conference, 2001*, p. 337.
10. J. A. Bellido, B. W. Clay, R. B. Dawson, and M. Johnston-Hollitt, astro-ph/0009039 (2000).

Translated by R. Tyapaev

JETP Letters, Vol. 75, No. 1, 2002, pp. 15–19. Translated from Pis'ma v Zhurnal Éksperimental'noĭ i Teoreticheskoĭ Fiziki, Vol. 75, No. 1, 2002, pp. 17–21.

Giant Third-Harmonic in Porous Silicon Photonic Crystals and Microcavities

T. V. Dolgova, A. I. Maĭdykovski, M. G. Martemyanov, A. A. Fedyanin, and O. A. Aktsipetrov*

Moscow State University, Vorob'evy gory, Moscow, 119899 Russia

**aktsip@shg.ru*

Received December 4, 2001

A giant enhancement (no less than by 10^3) of the optical third-harmonic generation in one-dimensional porous silicon microcavities and photonic crystals was observed experimentally. The enhancement is due to the resonant enhancement of the fundamental field in the cavity mode and the fulfillment of the phase matching condition at the photonic band gap edges of the photonic crystal and in the vicinity of the microcavity mode. © *2002 MAIK "Nauka/Interperiodica".*

PACS numbers: 42.65.Ky; 42.70.Qs

In recent years, the nonlinear optics of photonic crystals (PCs) and PC-based microcavities (MCs) has been progressing intensively [1]. Giant nonlinear-optical phenomena caused by giant effective dispersion at the edges of the photonic band gap and in the vicinity of the cavity mode, and also by the enhancement of optical fields inside PCs and MCs under optimal frequency–angular conditions, can be observed in such microstructures. In particular, multiple reflection interference in PCs can compensate the phase mismatch for fundamental and second-harmonic waves when one of the waves falls on the edge of the photonic band gap in the space of frequencies or wave vectors [2]. Such an effective fulfillment of the phase matching conditions leads to a resonant enhancement of second-harmonic generation in PCs composed, for example, of dielectric polystyrene spheres [3], alternate GaAs–AlGaAs [4] or ZnS–SrF_2 [5] layers, or alternate layers of porous silicon differing in porosity [6, 7]. At the same time, the spatial distribution of the electromagnetic field inside PCs and MCs can be adequately controlled. For example, the interference of waves with opposite projections of the wave vector onto the periodicity direction of the PC mirrors at a resonance of the external field with the MC mode leads to the formation of a standing wave inside the MC with an amplitude that resonantly increases in the vicinity of the cavity layer. The degree of field localization (enhancement), which is the measure of the quality factor of the MC, is determined by the parameters of the mirrors (photonic crystals) surrounding the cavity layer. An increase in the laser fluence inside the MC in the spectral (frequency or angular) vicinity of the MC mode leads to a resonant enhancement of the nonlinear-optical MC response (for example, to the giant second-harmonic generation in porous silicon [7] or zinc selenide [8] MCs) and to an enhancement of Raman scattering in GaAs–AlAs [9] or porous silicon [10] MCs. However, the enhancement of second-harmonic generation is limited by the destructive interference of second-harmonic waves generated by the cavity layer of a half-wavelength (for fundamental radiation) thickness; in this case, the PC layers nearest to the cavity layer make the main contribution to the second-harmonic signal. The nonlinear-optical effects that depend on a higher degree of the fundamental amplitude (for example, the optical third-harmonic generation (THG)) are free from this limitation.

This work presents the results of an experimental study on the giant THG in PC-based microcavities made of porous silicon. The resonant THG enhancement was found in angular TH intensity spectra in the vicinity of the cavity mode and at the edges of the photonic band gap. It is shown that the THG resonance in the mode is due to the combined action of the spatial localization of fundamental radiation in the vicinity of the cavity layer and the fulfillment of the phase matching condition. The enhancement of the standing fundamental wave amplitude in the resonant increase in the TH intensity in the MC mode is directly confirmed by near-field optical microscopy. The THG resonances at the edges of the photonic band gap are caused by the spatially uniform enhancement of the fundamental wave in PC mirrors of the MC and by the compensation of the phase mismatch between the fundamental and TH waves due to multiple reflection interference in the PC.

The samples of microcavities were prepared according to the conventional electrochemical procedure [11] by etching a wafer of heavily doped *p*-type silicon with the (100) crystallographic orientation and a resistivity of 0.01 Ω cm. A solution containing 15% of hydrofluoric acid, 27% of water, and 58% of ethyl alcohol was

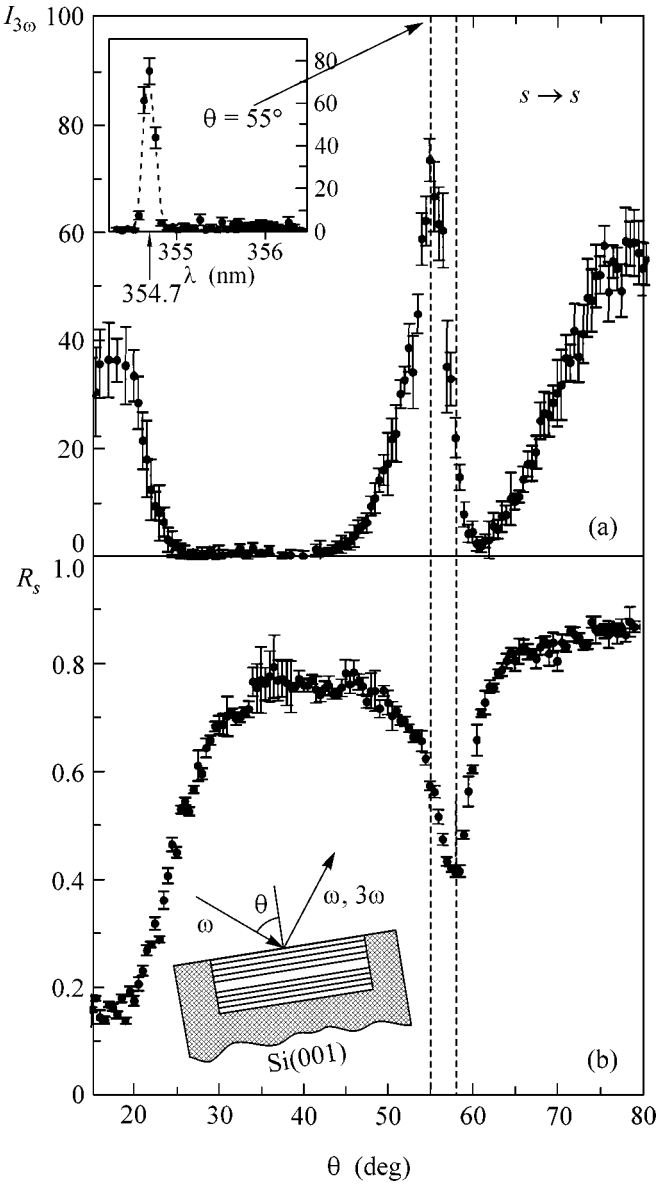

Fig. 1. (a) Intensity of the *s*-polarized TH radiation $I_{3\omega}$ measured in a porous silicon MC with $\lambda_{MC} \simeq 1300$ nm as a function of the angle of incidence θ of the *s*-polarized fundamental radiation ($\lambda_\omega = 1064$ nm). Dashed lines indicate the angular shift of the THG resonance from the position of the cavity mode. Inset: the spectrum of an optical signal in the vicinity of the TH wavelength measured at the THG resonance ($\theta = 55°$). (b) Angular spectrum of the reflection coefficient R_S of the *s*-polarized fundamental radiation from MC.

used as an electrolyte. The silicon wafer previously etched on both sides to remove the natural oxide was placed onto a flat copper cathode, and a platinum coil placed in the electrolyte above the silicon wafer surface in an electrochemical cell serves as the anode. The direct electric current was controlled by a galvanostat. To obtain a multilayer structure, the density of the current through the silicon wafer varies periodically, and, hence, the etching rate and the porosity (the volume fraction of air in the porous silicon) at the leading etch front also vary. As a result, the prescribed current density–time profile is transferred to the porosity–depth profile. A topographic image of a sample cleavage obtained using a scanning microscope with a piezoelectric quasi-friction force detector confirms the periodicity of the sample structures and the existence of well-defined boundaries between layers [7]. The microcavity samples under study with the microcavity mode at normal incidence $\lambda_{MC} \simeq 1300$ nm or $\lambda_{MC} \simeq 620$ nm represent a half-wavelength cavity layer confined between two PC mirrors composed of five pairs of quarter-wavelength porous silicon layers. Each pair consists of layers obtained by etching at current densities of 25 mA/cm^2 and 87 mA/cm^2. The corresponding porosities $f_{high} \simeq 0.60$ and $f_{low} \simeq 0.70$ are determined by porosity–current density calibration curves obtained in advance. The refractive indices of layers calculated with these porosities within the framework of the effective medium model at the fundamental wavelength comprise 2.0 and 1.65, respectively. The porosity of the cavity layer $f_{res} = f_{low}$. Uniform porous silicon films about 1.5 μm in thickness are prepared as reference samples.

A pulsed YAG:Nd^{3+} laser generating pulses with a duration of about 10 ns, the wavelength $\lambda_\omega = 1064$ nm, and a pulse energy of about 6 mJ was used. The polarized radiation of the laser passes through an infrared filter extracting the pumping and is directed at a sample clamped on a goniometer at an incidence angle θ. The goniometer provides a consistent revolution of the sample and the detection system in the range of incidence angles $0° < \theta < 90°$ with a minimum step of 0.5°. The radiation reflected from the sample passes through a system of ultraviolet filters 11 mm in total thickness, which extracts the radiation at the TH wavelength, and through a Glan prism, which controls the TH polarization state. Next, the signal is detected by a photomultiplier tube (PMT) and an electronic gated recording system connected with a computer. The possibility of mounting a monochromator with slits 0.05 mm in width after all the elements of the optical system is provided for checking the frequency spectrum of the reflected radiation. The angular spectrum of the linear reflection coefficient is measured in the identical alignment. For this purpose, the frequency of the fundamental radiation reflected from the sample is doubled by a quartz plate, because the PMT is not very sensitive in the IR region. To obtain the absolute normalization of the reflection coefficient, the fundamental radiation is directed to a PMT through all the elements of the optical system, excluding the sample.

The distributions of local fields inside a MC were characterized by near-field scanning optical microscopy. The sample cleavage under study is placed on a ceramic piezoelectric three-dimensional tube of the scanning microscope. A probing apertureless tip with a

radius of curvature of about 50 nm and made of an optical single-mode fiber is placed directly above the sample cleavage. The surface topography is traced by a feedback system with a tuning-fork resonant quasi-friction force detector. The fundamental radiation is supplied by a multimode optical fiber perpendicular to the sample surface as close to the MC cleavage as possible. The radiation collected by the probe is directed to the PMT cathode through a monochromator.

The THG experiments were performed for the geometry of fundamental and reflected TH waves polarized in the sample plane (*ss*-geometry). The choice of the geometry of an experiment is determined by the most pronounced manifestation of photonic properties for *s*-polarized waves. The corresponding component of the bulk cubic susceptibility of porous silicon $\chi^{(3)}_{yyyy}$ is not equal to zero, as distinct from $\chi^{(2)}_{yyy} \equiv 0$ where the *y* axis is perpendicular to the plane of incidence. Thus, the dipolar volume polarization $\mathbf{P}^{(3)}(3\omega)$ is the main source of third-harmonic generation in microcavities.

The intensity $I_{3\omega}$ of the third-harmonic reflected from a microcavity expressed in arbitrary units is shown in Fig. 1a as a function of the angle of incidence of the fundamental radiation on the sample. An enhancement at the edges of the photonic band gap ($\theta = 17°$ and $\theta = 75°$) and a narrow peak in the region of the cavity mode ($\theta = 55°$) are observed in the angular spectrum $I_{3\omega}(\theta)$. The enhancement of the TH intensity in the MC mode comprises no less than 10^3 as compared with $I_{3\omega}$ in the photonic band gap. The inset in Fig. 1 shows the frequency constitution of the radiation reflected from the MC and passed through a set of filters of the recording system. The composition was obtained with the use of a monochromator. A narrow (with a half-width of about 0.1 nm) spectral peak is observed at a wavelength of 354.7 nm. This peak corresponds to the third-harmonic for pumping with a wavelength of 1064 nm. Measurements of the reflected radiation spectrum in a wide range showed the reliability of the selected set of filters for extracting the third-harmonic: radiation at wavelengths differing from the TH was not detected. The linear reflection coefficient R_s of the infrared *s*-polarized fundamental radiation is shown in Fig. 1b as a function of the angle of incidence on a microcavity sample. The region of the photonic band gap in angular variables starts at approximately $\theta = 25°$ and corresponds to vanishingly small values of the third-harmonic intensity. A dip is observed in the angular reflection spectrum at an incidence angle of 58°. Analogous measurements of the angular spectra $I_{3\omega}(\theta)$ and $R_s(\theta)$ were carried out for a uniform silicon wafer with a thickness of 1.5 μm, which is comparable with the total thickness of the microcavity sample (Fig. 2). Effects associated with multiple reflection interference, namely, a broad peak in the angular third-harmonic spectrum and oscillations in the reflection coefficient are also observed in the curves obtained.

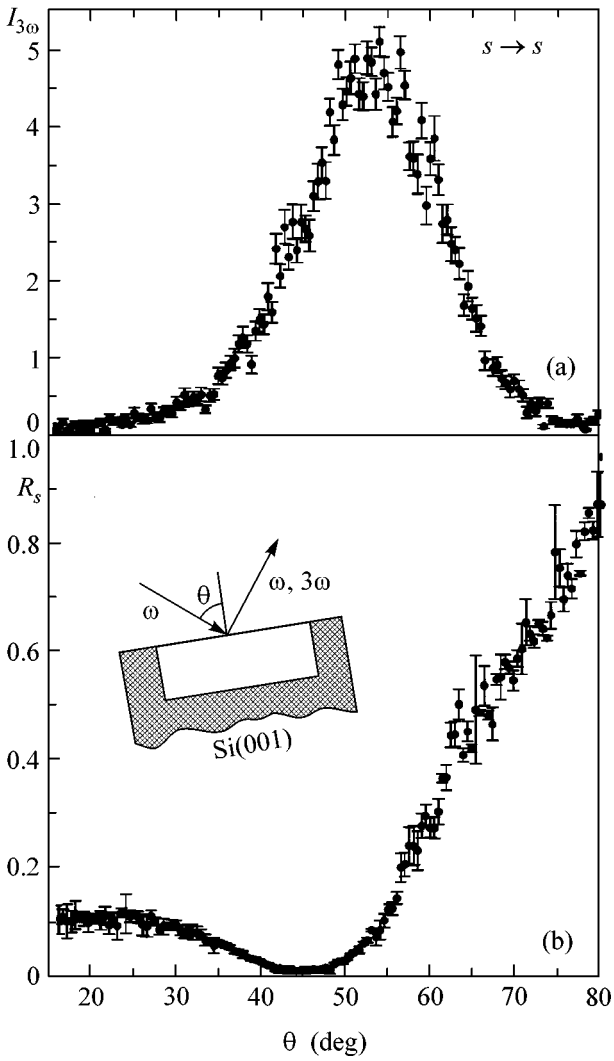

Fig. 2. Angular spectrum of the *s*-polarized TH radiation intensity $I_{3\omega}$ measured for a uniform porous silicon wafer 1.5-μm thick as a function of the angle of incidence θ of the *s*-polarized fundamental radiation. The TH intensity units are the same as in Fig. 1a. (b) Angular spectrum of the reflection coefficient R_s of the *s*-polarized fundamental radiation from a uniform porous silicon wafer.

The features of the angular spectrum of the third-harmonic generated by a microcavity are determined by the phase matching conditions, which signify the constructive interference of third-harmonic waves from each MC layer or, in other words, the equality of the effective refractive indices at the fundamental and third-harmonic frequencies [12]. These conditions are fulfilled in the regions of high effective dispersion, which correspond to fast variations in the angular spectrum of the linear reflection coefficient, and determine the enhancement of third-harmonic generation at the photonic band gap edges at $\theta = 17°$ and $\theta = 75°$. The

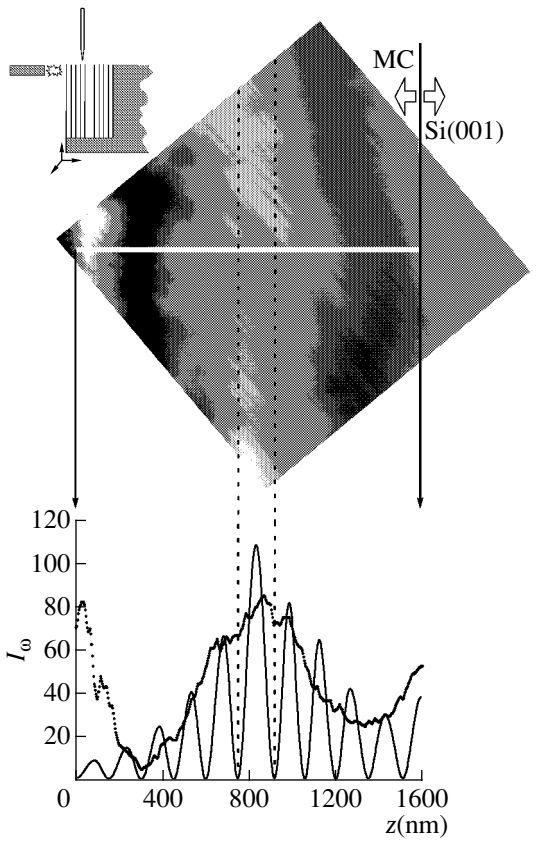

Fig. 3. At the top: spatial distribution of the optical field intensity at an MC cleavage with $\lambda_{MC} \simeq 620$ nm measured by a near-field optical microscope at resonance excitation by the radiation of a He–Ne laser at a normal to the MC. At the bottom: cross-section of the intensity image along the direction of PC periodicity (dots) and a model spatial distribution of the standing wave intensity in the cavity mode (solid lines). Dashed lines indicate the boundaries of the cavity layer.

weak manifestation of the photonic band gap edge in the angular dependence R_s at large angles θ is apparently associated with the rapid growth of the Fresnel coefficients in this region. The THG peaks at the photonic band gap edges are due to interference in the PC structure and are not associated directly with the existence or nonexistence of the cavity layer.

The giant enhancement of third-harmonic generation for a microcavity at $\theta = 55°$ is provided by a combination of the fulfillment of the phase matching condition in the region of the cavity mode and the localization of the fundamental field in the cavity and nearest layers. The position of the dip in the linear reflection coefficient (Fig. 1b) is determined by the angular position of the microcavity mode at which the localization of the field in the cavity layer is most strongly pronounced. The peak in the TH intensity spectrum is shifted with respect to this position by a value determined by the fulfillment of the phase matching condition. Both samples, namely, a photonic crystal microcavity and a uniform wafer, admit a similar consideration in terms introduced for a cavity. The interfaces of a uniform wafer with air and with the substrate serve as mirrors in this case. The reflection coefficients of such mirrors are considerably smaller than those for multilayer structures. In fact, when characterizing microcavities by the quality factor determined through the half-widths of THG resonance peaks at their half-maximum, one can see that this value in angular variables equals 10° for a uniform wafer and is 5 times smaller for a microcavity. The third-harmonic intensity reached in the MC mode is 15 times higher than in the maximum of the $I_{3\omega}(\theta)$ curve for a porous silicon film.

The localization of the field in the vicinity of the cavity layer was directly demonstrated by the measurement of the spatial two-dimensional distribution of the fundamental field intensity using a near-field microscope (Fig. 3). The image was obtained for a MC cleavage with $\lambda_{MC} \simeq 620$ nm at resonance excitation by the radiation of a He–Ne laser with $\lambda_\omega = 633$ nm at a normal to the MC surface. The bright strip in the vicinity of the cavity layer corresponds to the resonant increase in light intensity detected by the microscope probe. The dark strips in the image correspond to intensity minima and fall on the centers of the PC mirrors. The contrast between the minimum and maximum intensities, which characterizes the degree of field localization in the cavity, reaches 10. The bright spot in the near-surface region of the sample ($z < 200$ nm) is apparently a consequence of the scattering of radiation by the sample surface. The cross-section of the image in the direction perpendicular to the microcavity surface correlates well with the envelop of the model spatial distribution of the standing fundamental wave intensity calculated within the propagation matrix formalism (Fig. 3, at the bottom).

Thus, the localization of laser radiation in the vicinity of the cavity layer of microcavities with photonic crystal mirrors (at a resonance with the MC mode) and also inside photonic crystals (when the radiation wavelength and wave vector fall on the edge of the photonic band gap) leads to a giant enhancement of their nonlinear-optical response, in particular, to the generation of a giant third-harmonic. The matching of the phase velocities of the fundamental and third-harmonic radiations due to multiple reflection interference in the photonic crystals of the mirrors is another factor of the enhancement of the third-harmonic generation in microcavities.

The authors are grateful to N. Ota for help in preparing the microcavity samples and to V.A. Yakovlev for fruitful discussions.

This work was supported by the Russian Foundation for Basic Research, project nos. 00-15-96555, 01-02-16746, 01-02-17524, and 01-02-04018.

REFERENCES

1. K. Sakoda, *Optical Properties of Photonic Crystals* (Springer-Verlag, Berlin, 2001), p. 109.
2. N. Bloembergen and J. Sievers, Appl. Phys. Lett. **17**, 483 (1970).
3. J. Martorell, R. Vilaseca, and R. Corbalan, Appl. Phys. Lett. **70**, 702 (1997).
4. J. P. van der Ziel and M. Ilegems, Appl. Phys. Lett. **28**, 437 (1976).
5. A. V. Balakin, V. A. Bushuev, N. I. Koroteev, *et al.*, Opt. Lett. **24**, 793 (1999).
6. L. A. Golovan', A. M. Zheltikov, P. K. Kashkarov, *et al.*, Pis'ma Zh. Éksp. Teor. Fiz. **69**, 274 (1999) [JETP Lett. **69**, 300 (1999)].
7. T. V. Dolgova, A. I. Maĭdykovskiĭ, M. G. Martem'yanov, *et al.*, Pis'ma Zh. Éksp. Teor. Fiz. **73**, 8 (2001) [JETP Lett. **73**, 6 (2001)].
8. V. Pellegrini, R. Colombelli, I. Carusotto, *et al.*, Appl. Phys. Lett. **74**, 1945 (1999).
9. A. Fainstein, B. Jusserand, and V. Thierry-Mieg, Phys. Rev. Lett. **75**, 3764 (1995).
10. L. A. Kuzik, V. A. Yakovlev, and G. Mattei, Appl. Phys. Lett. **75**, 1830 (1999).
11. O. Bisi, S. Ossicini, and L. Pavesi, Surf. Sci. Rep. **38**, 1 (2000).
12. M. Centini, C. Sibilia, M. Scalora, *et al.*, Phys. Rev. E **60**, 4891 (1999).

Translated by A. Bagatur'yants

JETP Letters, Vol. 75, No. 1, 2002, pp. 20–22. Translated from Pis'ma v Zhurnal Éksperimental'noĭ i Teoreticheskoĭ Fiziki, Vol. 75, No. 1, 2002, pp. 22–24.

Ion Formation upon Water Excitation by IR Laser Radiation in the Range of OH Stretching Vibrations

D. V. Klochkov*, G. E. Kotkovskiĭ, A. S. Nalobin, E. S. Tananina, and A. A. Chistyakov

Moscow Institute of Engineering Physics (Technical University), Kashirskoe sh. 31, Moscow, 115409 Russia

** e-mail: klotch@mail.ru*

Received November 13, 2001

The ion formation and emission upon the excitation of liquid water in the range of OH stretching vibrations were observed and studied. The radiation source was a nanosecond parametric light oscillator tunable in the range of 2.7–3.3 μm. The ions were detected by an ion-mobility spectrometer. © *2002 MAIK "Nauka/Interperiodica".*

PACS numbers: 33.80.Eh; 79.90.+b; 78.30.Cp

Liquid water displays specific nonlinear optical and photophysical properties upon resonant laser excitation in the range of OH stretching vibrations. For example, the effect of liquid water bleaching under the action of intense ($q \sim 10^7$ W/cm^2) resonance IR laser radiation at wavelengths $\lambda = 2.94$ and 2.79 μm was observed in [1]. The study of the nonlinear transmission over the entire range of OH band using a tunable parametric light oscillator showed that the transmission nonmonotonically depends on intensity at $\lambda = 3.1$–3.4 μm, i.e., in the spectral range due to the associated water molecules [2]. Moreover, it was found that the excitation of associated water is accompanied by an increase in the Raman scattering signal at frequencies $\nu = 3100$–3400 cm^{-1} corresponding to the vibrations of associated molecules. One can hardly explain these results by equilibrium heating. It is more probable that the distribution of vibrational excitation among the water associates, whose molecules absorb radiation, and free molecules is nonequilibrium, at least, during the laser pulse.

This work is aimed at studying a new phenomenon which we observed upon IR laser excitation of the liquid water molecules in the range of OH stretching vibrations, namely, the phenomenon of ion formation and emission. This problem seems to be highly topical from the fundamental point of view, because it is a new nonequilibrium photoprocess initiated in a vibrationally excited molecular condensed medium. The study of this problem is topical in connection with the intensive development of a high-sensitive matrix-assisted laser desorption ionization (MALDI) method for analysis of complex organic and biological molecules [3, 4]. This method is based on the ionization of the molecules of a substance as a result of laser excitation of the surrounding (matrix) molecules, followed by the analysis of the results by the methods of mass spectrometry or ion-mobility spectrometry (IMS). At present, the physical principles of analysis for the vibrational excitation of a matrix are in their infancy.

EXPERIMENTAL METHOD

The vibrational excitation of water molecules was provided by a single-cavity $LiNbO_3$ parametric light oscillator (PLO) pumped by a YAG:Nd laser. The PLO radiation ($\tau_p \sim 7$ ns, $E_p = 5$ mJ) was tuned from 2.7 to 3.3 μm, which corresponded to the water absorption in the OH stretching range.

One can expect that the ion-formation process depends on the choice of the excitation spectral range, as was observed for the nonlinear transmission and Raman scattering of water. For this reason, the ionization in our experiments was accomplished at both high-frequency ($\lambda = 2.73$–2.84 μm) and low-frequency ($\lambda = 3.1$–3.3 μm) wings of the water absorption band. To provide the same thermodynamic conditions for the laser action in the regions of predominantly free and associated water, the radiation wavelengths were chosen so that the linear absorption coefficients in these regions were identical. The choice of wavelengths is illustrated in Fig. 1, where the water IR transmission spectrum in the range of OH stretching vibrations is shown. The laser intensity was varied in the range $q = 5$–20 MW/cm^2.

The ions were detected on an ion-mobility spectrometer. This method offers certain advantages over the traditional mass spectrometric method, because it is much more sensitive and also because it allows experiments with water to be conducted under natural conditions. The spectrometer operates on the principle of ion-mobility separation in the course of ion drift with a constant velocity $V = \mu E$ in a constant electric field E (μ is the ion mobility). The ion signal on the collector is detected as a function of drift time, thus forming the ion-mobility spectrum. Since the duration of ion-cloud

0021-3640/02/7501-0020$22.00

formation is determined by the duration of the laser pulse, it is much shorter than the characteristic time of ion drift from the ionization zone to the collector. Because of this, the instant of pulse action on the sample is taken as zero time. The laser ion-mobility spectrometer that we devised provides sensitivity at a level of 10^2–10^3 ion/pulse and has the resolution $R = t/\Delta t > 50$ [5], where t is the drift time of ions forming a certain peak and Δt is the peak FWHM. The ion drift occurs in an atmosphere of special purity grade nitrogen under normal conditions. The ionization was accomplished by the action of laser radiation on liquid water samples. A water layer with a thickness of ~1 mm was placed on a fluorite substrate inside the drift tube.

Both twice-distilled water and distilled water subjected to deionizing purification were used as samples.

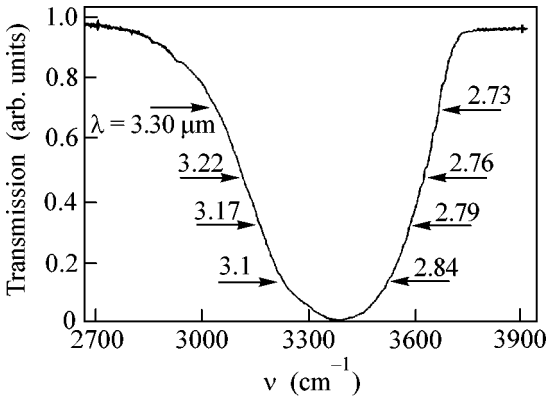

Fig. 1. IR transmission spectrum of water. Arrows indicate the wavelengths of exciting laser radiation used in the experiment.

RESULTS AND DISCUSSION

The action of IR laser radiation with q = 5–20 MW/cm^2 on twice-distilled water was found to induce the emission of positive ions from water if the radiation was resonant to the OH stretching vibrations of the H_2O molecule. The ion-mobility spectra obtained for different wavelengths are shown in Fig. 2. One can see that the emitted ions form a signal at drift times t_d > 20 ms, which correspond to the mobilities $\mu < 1$ cm^2/(V s). The amplitudes of ion signals depend on the laser wavelength. As the excitation wavelength increases in the range 3.1–3.3 μm, the maximum of the ion signal shifts to larger drift times (to smaller μ).

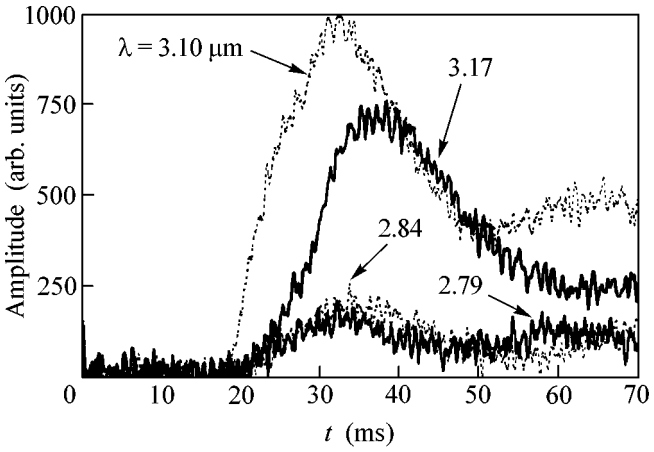

Fig. 2. Ion-mobility spectra recorded upon the action of laser radiation with different wavelengths and q = 13.7 MW/cm^2 on water.

The dependence of the integrated intensity of the ion signal on the excitation wavelength in the range of drift times t_d = 20–70 ms [μ = 1–0.3 cm^2/(V s)] is shown in Fig. 3. One can see from the comparison of the ion signals obtained with the same linear absorption coefficient for the associated (λ = 3.1–3.3 μm) and free (λ = 2.73–2.84 μm) water molecules that the ion signals in the first case are several times higher. This tendency persists in the whole range of excitation intensities (q = 5–20 MW/cm^2) used in the experiment. This result allows a conclusion to be drawn about the nonequilibrium nature of the observed effect. It cannot be explained solely by the nonlinear dependence of the water absorption coefficient on the laser intensity, because the absorption coefficient of associated water is always lower than for the free water in the range of intensities used [2].

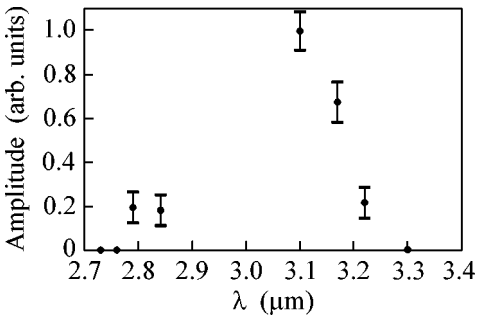

Fig. 3. Integrated intensity of the ion signal as a function of the wavelength of exciting radiation with q = 13.7 MW/cm^2.

It is worth noting that the mobilities of the experimentally detected ions are $\mu < 1$ cm^2/(V s). The water ions and the ions of water clusters are known to be much more mobile [$\mu > 1.8$ cm^2/(V s)]. Most likely, the ions observed in our experiments are molecular ions of a dissolved organic substance (DOS), which is always present in natural water whatever the degree of purification is [7].

The possible mechanism of DOS ionization consists of the proton transfer from the vibrationally excited water molecule to the impurity molecule. However, the ion signal can also be caused by the ions which are present in water from the very beginning, because many substances dissociate in water to form ions. To answer the question about the nature of the observed ions, experiments with deionized water were carried out.

A comparison of the ion spectra of twice-distilled water with the spectra of water subjected to deionizing purification indicates that, under the same conditions of laser action, the ion yield for the deionized water is even higher than for the laser-excited twice-distilled water. Therefore, one can conclude that the detected ions are formed as a result of vibrational excitation of water molecules by laser radiation. Otherwise, i.e., if we had detected the ions which were initially present in water, the removal of ions from water would have depressed the signal. As to the fact that the amplitude of the ion signal from the deionized water increases, compared to the plain twice-distilled water, the likely reason for this is that, in the course of deionization, water repeatedly passes through the columns with cationites and anionites and absorbs additional impurities.

In our opinion, the proton transfer from the excited water molecule to the DOS molecule is the most probable mechanism of ion formation. The organic molecules dissolved in water are hydrophilic by their nature, i.e., they are capable of associating water molecules. It then becomes clear why the effect is particularly pronounced when the associated molecules are directly excited (Fig. 3). In this case, the proton transfer from the excited water molecule to the DOS molecule is most probable. The experiments with hydrophobic molecules (toluene derivatives) specially dissolved in water also corroborate our assumption: despite the substantially higher concentrations of such molecules, the ion yield upon excitation of both associated and free water proves to be exceedingly low.

In summary, the effect of formation of the positive ions with mobilities $\mu < 1$ cm^2/(V s) upon the excitation of twice-distilled water by resonance IR laser radiation with wavelengths $\lambda = 2.73$–3.3 μm and intensities $q = 5$– 20 MW/cm^2 has been observed. The fact that, under the same thermodynamic conditions of laser excitation, the ion-formation efficiency in the case of vibrational excitation of associated molecules is several times higher than for the excitation of free molecules indicates that the observed effect is nonequilibrium.

This work was supported in part by the Ministry of Industry, Science, and Technology of the Russian Federation (project no. 08-02-48). We are grateful to V.V. Fadeev for helpful discussions.

REFERENCES

1. K. L. Vodop'yanov, Zh. Éksp. Teor. Fiz. **97**, 205 (1990) [Sov. Phys. JETP **70**, 114 (1990)].
2. Yu. A. Bykovskii, D. V. Klotchkov, V. B. Oshurko, and A. A. Chistyakov, Laser Phys. **8**, 172 (1998).
3. F. Kirpekar, S. Berkenkap, and F. Hillenkamp, Anal. Chem. **71**, 2334 (1999).
4. S. J. Lawson and K. K. Murray, Rapid Commun. Mass Spectrom. **14**, 129 (2000).
5. A. A. Chistyakov, H. H. Hill, D. V. Klochkov, *et al.*, J. Ion Mobility Spectrom. **4**, 160 (2001).
6. C. Shumate, R. H. St. Louis, and H. H. Hill, Jr., J. Chromatogr. **373**, 141 (1986).
7. E. M. Filippova, V. V. Fadeev, V. V. Chubarov, *et al.*, Appl. Spectrosc. Rev. **36**, 87 (2001).

Translated by V. Sakun

JETP Letters, Vol. 75, No. 1, 2002, pp. 23–25. From Pis'ma v Zhurnal Éksperimental'noĭ i Teoreticheskoĭ Fiziki, Vol. 75, No. 1, 2002, pp. 25–27.

Equation of State and Structural Phase Transition in $FeBO_3$ at High Pressure[1]

A. G. Gavriliuk*, I. A. Trojan*, R. Boehler, M. Eremets**, A. Zerr***, I. S. Lyubutin****, and V. A. Sarkisyan******

**Institute of High-Pressure Physics, Russian Academy of Sciences, Troitsk, Moscow oblast, 142092 Russia*

*** Max-Planck Institut für Chemie, 55020 Mainz, Germany*

**** Technische Universität Darmstadt, FB Material- und Geowissenschaften, FG Disperse Feststoffe, 64287 Darmstadt, Germany*

***** Shubnikov Institute of Crystallography, Russian Academy of Sciences, Leninskii pr. 59, Moscow, 117333 Russia*

e-mail: lyubutin@ns.crys.ras.ru

Received November 23, 2001

The evolution of X-ray diffraction patterns in $FeBO_3$ under high pressures up to 63 GPa has been investigated at room temperature in a diamond anvil cell. A structural phase transition at a pressure of 53 ± 2 GPa was found for the first time. The transition is of the first-order type with a hysteresisless drop of the reduced unit cell volume of about 8.6%. Apparently, the transition is isostructural. At pressures below the transition, the equation of state for $FeBO_3$ was fitted. In the third-order approximation of the Birch-Murnagan equation of state, the bulk modulus K and its first pressure derivative K' were found to be 255 ± 25 GPa and 5.0 ± 1.2, respectively. © *2002 MAIK "Nauka/Interperiodica".*

PACS numbers: 61.50.Ks; 64.70.Kb; 64.30.+t; 62.50.+p

Under ambient conditions, the crystal lattice of iron borate $FeBO_3$ has rhombohedral symmetry with space the group $R\bar{3}c$ (D_{3d}^6) and with lattice parameters a = 4.612 Å and c = 14.47 Å [1, 2]. Iron ions Fe^{3+} are in an octahedral oxygen surrounding, and interionic distances are (Fe–O) = 2.028 Å and (Fe–Fe) = 3.601 Å, while the angles of the bonds (O–Fe–O) are 91.82° and 88.18° [2]. $FeBO_3$ is an antiferromagnet with weak ferromagnetism and with a Neel temperature of about 348 K [3]. This material has very interesting electronic, magnetic, and magnetooptical properties. Recently, the transition from a magnetic to nonmagnetic state has been discovered at pressures of about 46 GPa in the $FeBO_3$ single crystal [4]. The nature and mechanism of this transition are not known yet. It is interesting whether this transition is accompanied by a structural transition, and it is important to investigate how changes of interionic distances and crystal structure under pressure influence the electronic and magnetic properties in this compound.

In the present paper, we have investigated in detail the room temperature X-ray diffraction spectra in $FeBO_3$ at high pressures up to P = 63 GPa using a diamond anvil cell (DAC). The powder sample was obtained by grinding the $FeBO_3$ single crystal. The diameter of culets of diamond anvils was about 300 μm. The diameter of the gasket hole was about 100 μm. At different pressure scans, tungsten or rhenium was used as the gasket material. As the pressure medium we used silicon organic liquid, which is quite appropriate for maintaining quasi-hydrostatic conditions. The gasket hole was filled with the sample powder to about one-third to ensure that all powder grains were surrounded by pressure liquid. The shift of ruby fluorescence was used to determine pressure. To estimate the pressure distribution along the sample, several ruby chips were placed inside the hole at different distances from the center. It was found that the pressure gradient at the sample was not more than 4–5 GPa at maximal pressures. The DAC applied in this study allowed us to collect X-ray data in an angle range of about 30 degrees of 2Θ. X-ray patterns were recorded in the transmission geometry on an image plate and were then treated by the standard procedure. As the X-ray source we used a rotating Mo anode equipped with specially designed focusing X-ray optics.

Figure 1 shows changes in the X-ray diffraction patterns of $FeBO_3$ with higher pressure. It can be seen that new peaks appear at about 52 Gpa, indicating the onset of phase transition to a new crystal structure. Both initial and new crystal structures coexist in the pressure range 52–55 GPa, apparently due to a pressure gradient. In the measured range of diffraction angles 2Θ, we found that the high-pressure phase at $P > 55$ GPa has a set of X-ray peaks similar to that of the low-pressure phase at $P < 52$ GPa (Figs. 1a and 1b). Figure 2 shows the experimental X-ray diffraction pattern obtained at

[1] This article was submitted by the authors in English.

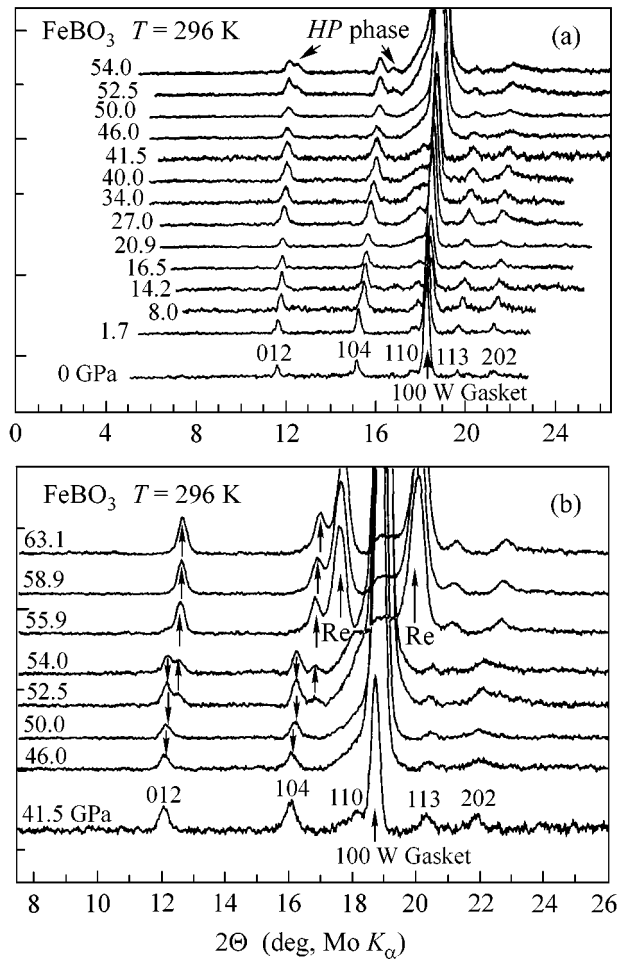

Fig. 1. Evolution of the X-ray diffraction pattern of $FeBO_3$ at high pressures: (a) below phase transition, (b) in the region of the phase transition and at higher pressures. The peaks of W and Re gaskets are also seen.

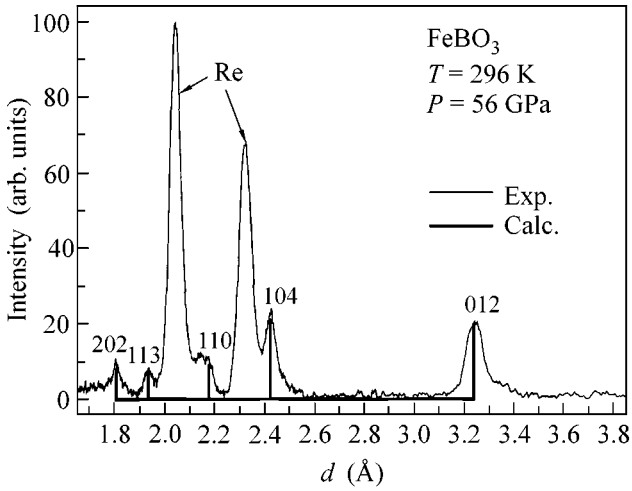

Fig. 2. X-ray pattern of the high-pressure phase of $FeBO_3$ at P = 56 GPa. The solid line is an experimental pattern, the bars are a theoretical calculation of interplanar d_{hkl}-spaces in a hexagonal representation for the $R\bar{3}c$ space group with the lattice parameters a = 4.3539 Å and c = 12.6642 Å. The other peaks fit well to reflexes of the compressed Re gasket.

56 GPa and positions of the calculated reflexes for the structure of space group $R\bar{3}c$. The calculated data fit the experimental peaks well when the lattice parameters a and c are 4.3539 Å and 12.6642 Å, respectively. Five reflexes of the new high-pressure phase fit very well to the same symmetry as the low-pressure phase. The interplanar distances and the peak intensities of the X-ray diffraction pattern of $FeBO_3$ recorded at 56 GPa are given in Table 1. However, the measured range of angles 2Θ is not enough to make a final conclusion; it is more likely that the transition is isostructural. Recently, Parlinski [5] calculated a possible change of the crystal structure in $FeBO_3$ using the density func-

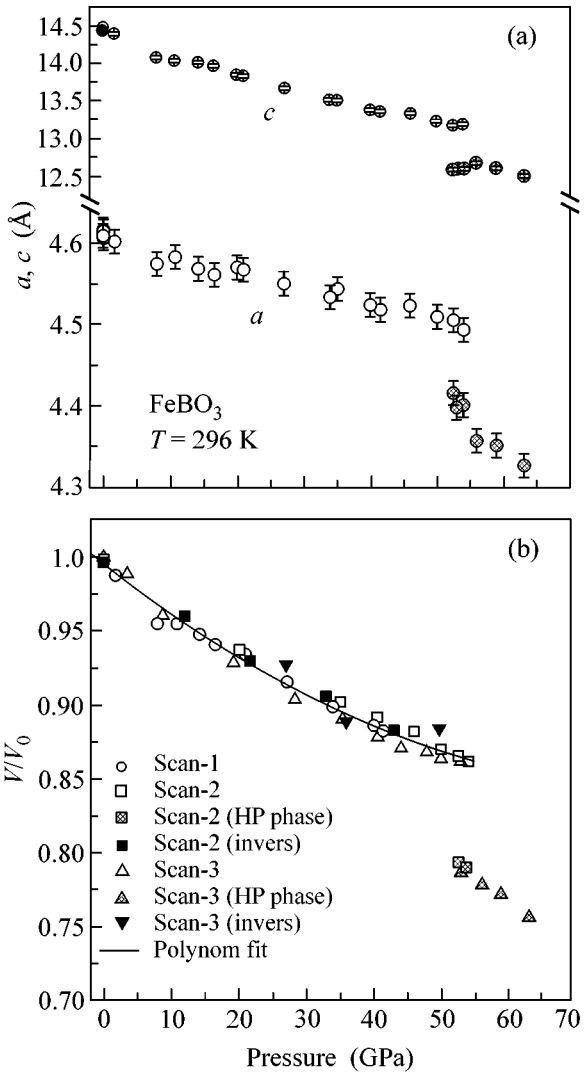

Fig. 3. The experimental pressure dependence of the unit cell parameters a and c and the reduced unit cell volume V/V_0 of $FeBO_3$ measured at room temperature in a DAC. The pressure medium is poly-ethyl-silicon. At pressures above the phase transition P > 52.5 GPa, the $V(P)$ relation was calculated assuming that the crystal structure of the high-pressure phase has the same symmetry as the low-pressure one.

tional theory and found that the phase transition to the same space group $R\bar{3}c$ should exist at a certain pressure.

Under this assumption, we calculated the unit cell volume and the $V(P)$ dependence for the high-pressure phase of $FeBO_3$. Figures 3a and 3b show the pressure dependence of the unit cell parameters a and c and the reduced unit cell volume V/V_0. It is obvious that the observed structural transition is of the first order; the drop of the V/V_0 value is about 8.6%. To determine possible hysteresis of the transition, we also measured X-ray diffraction patterns at the pressure release regime. It was found that the hysteresis is in the limit of pressure distribution along the sample due to nonhydrostaticity.

At pressures below the transition, four types of equations of state (the second-power polynomial, Murnagan, Birch–Murnagan, and Vinet) were fitted to the experimental dependence $V(P)$. The results of calculations are given in Table 2. It seems that the fit of the Birch–Murnagan equation of state with the bulk modulus $K = 255 \pm 25$ GPa and its first pressure derivative $K' = 5.0 \pm 1.2$ gives the most reliable result. The value of the bulk modulus is close to that estimated for an oxygen octahedron surrounding an iron ion in other iron oxides (≈280 GPa) [6, 7]. This correlates with a possible freedom of change in the crystal structure in $FeBO_3$. Under pressure, only compression of an oxygen octahedron is possible in $FeBO_3$. The same is valid for α-Fe_2O_3, in contrast, for example, to the rare-earth orthoferrites $RFeO_3$, where, in addition to compression, there is freedom of rotation of oxygen octahedrons.

Special attention should be paid to the problem of different values of pressure for the structural transition found in the present study at 53 ± 2 GPa and the magnetic transition found at 46 ± 2 GPa in [4]. The powder sample (a grained single crystal) was used in the present study, while a single-crystal specimen of $FeBO_3$ enriched with the isotope Fe-57 was used in the magnetic measurements [4]. It is important to verify whether the pressure difference of the structural and magnetic transitions is a sample effect or a physical effect. We are now carrying out Mössbauer spectroscopy experiments with the powder sample with the aim of clarifying this problem.

In summary, the X-ray diffraction spectra and $V(P)$ dependence for $FeBO_3$ were measured at room temperature at pressures up to 63 GPa. The bulk modules calculated using the Birch–Murnagan equation of state is 255 ± 25 GPa, and its first pressure derivative K' is 5.0 ± 1.2. At a pressure of 53 ± 2 Gpa, we observed the first-order phase transition (apparently of the isostructural type) with a unit cell volume decrease of about 8.6%. The isostructural character of the transition is in agreement with the density functional theory calculations [5]. The pressure value of the structural transition differs from that of the transition from a magnetic to nonmagnetic state, which was found recently in $FeBO_3$ [4].

Table 1. Interplanar distances, peak intensities, and the corresponding Miller indices of the high-pressure phase of $FeBO_3$ at $P = 56$ GPa calculated in an approximation of the space group $R3c$ with the unit cell parameters $a = 4.3539$ Å and $c = 12.66422$ Å. (Mo radiation, $T = 296$ K)

$h\,k\,l$	Intensity	d_{exp} (Å)	d_{calc} (Å)	$d_{calc} - d_{exp}$ (Å)
1 0 2	90	3.24420	3.23971	−0.00449
1 0 4	100	3.42443	2.42466	+0.00023
1 1 0	30	2.17300	2.17695	+0.00395
1 1 3	20	1.93562	1.93483	−0.00079
2 0 2	20	1.80583	1.80691	+0.00108

Table 2. The bulk modules K and its first pressure derivative K' calculated from different types of EOS fitted to experimental $V(P)$ of $FeBO_3$ measured at $T = 296$ K

Equation of state	K (GPa)	K'
second-power polynomial	273 ± 4	4.0 (fixed)
Murnagan	254 ± 23	4.6 ± 1.0
Birch–Murnagan	255 ± 25	5.0 ± 1.2
Vinet	250 ± 25	5.2 ± 1.2

We are grateful to Professor R. Rüffer for useful discussions. This work was partially supported by NATO grant no. PST.CLG.976560 and by the Russian Foundation for Basic Research, project nos. 00-02-17710-a, 01-02-17543-a, and 02-02-17364-a. This study was also partly supported by grant INTAS-710.

REFERENCES

1. Database PDF-II, record 21-0423; I. Bernal, C. W. Struck, and J. G. White, Acta Crystallogr. **16**, 849 (1963).
2. R. Diehl, Solid State Commun. **17**, 743 (1975).
3. R. Wolff, A. J. Kurtzig, and R. C. LeCraw, J. Appl. Phys. **41**, 1218 (1970).
4. I. A. Trojan, A. G. Gavriliuk, V. A. Sarkisyan, *et al.*, Pis'ma Zh. Éksp. Teor. Fiz. **71**, 26 (2001) [JETP Lett. **74**, 24 (2001)].
5. K. Parlinski, submitted to Eur. Phys. J. B.
6. R. M. Hazen and L. W. Finder, *Comparative Crystal Chemistry* (Wiley, New York, 1982).
7. A. G. Gavrilyuk, G. N. Stepanov, I. S. Lyubutin, *et al.*, Zh. Éksp. Teor. Fiz. **117**, 375 (2000) [JETP **90**, 330 (2000)].

JETP Letters, Vol. 75, No. 1, 2002, pp. 26–28. Translated from Pis'ma v Zhurnal Éksperimental'noĭ i Teoreticheskoĭ Fiziki, Vol. 75, No. 1, 2002, pp. 28–30.

Anomalous Behavior of Silver Atoms in Intercalation under a Two-Dimensional Graphite Film

N. R. Gall*, E. V. Rut'kov, and A. Ya. Tontegode

Ioffe Physicotechnical Institute, Russian Academy of Sciences, Politekhnicheskaya ul. 26, St. Petersburg, 194021 Russia

**gall@ms.ioffe.rssi.ru*

Received November 29, 2001

It is shown that silver atoms, the only ones of many atoms studied previously (Si, C, Mo, Pt, Cu, Ir, Ni, Au, Cs, K, Na, Ba, …), do not intercalate, that is, do not penetrate under a two-dimensional graphite film (2DGF) on a metal either upon direct depositing in the temperature range 300–2000 K or annealing of a previously deposited silver film. Intercalation becomes possible if silver is deposited on a 2DGF with previously intercalated cesium; in this case, silver atoms displace Cs atoms from under the 2DGF upon heating up to 1100 K. © *2002 MAIK "Nauka/Interperiodica".*

PACS numbers: 68.35.-p; 81.15.Cd

Intercalation under two-dimensional graphite films (2DGFs) on metals was first observed in our work in 1981 [1] and was described in detail in [2, 3]. It was found that a 2DGF on a metal behaves as a two-dimensional crystal that is weakly bound with the metal surface by van der Waals forces [4] and has the same structure as one layer in a graphite single crystal [5–7]. In this case, intercalation is spontaneous penetration of foreign particles (atoms [1–3] or fullerene molecules C_{60} [8]) adsorbed on a 2DGF under the film. The film itself only moves away from the metal surface remaining virtually unchanged, in the same way as graphite layers move apart upon intercalation of a graphite single crystal [9].

It was found that the regularities of intercalation are virtually independent of the nature of the metal substrate on which the 2DGF is formed (Ir, Re, Pt, …), but these regularities depend on the nature of the intercalated particles in a decisive way [2, 3]. Thus, atoms with low ionization potentials (Cs, K, Na, …) intercalate a 2DGF at room temperature with an efficiency of ~ 0.5; that is, half the number of atoms that arrive at the surface go under the layer. In this case, intercalation proceeds only after attaining a certain critical concentration N_c in the adsorbed layer (or the critical coverage $\theta_c = N_c/N_m$, where N_m is the monolayer concentration). For Cs, $\theta_c = 0.01$ [2], and the limiting concentration of atoms in the intercalated phase does not exceed one monolayer.

On the contrary, atoms with high ionization potentials (Si, C, Pt, Ir, Cu, Mo, …) intercalate under a 2DGF with efficiency close to unity (!) at $T \sim 1000$–1200 K. No concentration threshold has been found for intercalation, and either a thick multilayer intercalate film or a bulk compound composed of intercalate and substrate metal atoms, for example, rhenium silicide, forms under the graphite monolayer.

With the aim of extending the range of atoms that can intercalate under a 2DGF on a metal, we decided to use silver atoms, whose ionization potential V = 7.57 eV is intermediate with respect to the groups of atoms mentioned above, as an intercalate.

The experiments were performed using a high-resolution Auger spectrometer ($\Delta E/E < 0.1\%$) with a prism energy analyzer described in [10]. It was a possible to measure Auger spectra directly at a high substrate temperature in the range 300–2200 K. The following Auger peaks were used for quantitative estimations: Ag, the second peak of the doublet with E = 356 eV (peak-to-peak); Ir, the triplet with energies E = 154, 162, and 171 eV (from the top of the peak with E = 154 eV to the bottom of the peak with E = 171 eV); C, the peak with E = 272 eV (from the bottom of the peak to the background level); and Cs, the second peak of the doublet with E = 575 eV (peak-to-peak).

The two-dimensional graphite film was created on a substrate of textured polycrystalline Ir ($1 \times 40 \times 0.02$) mm^3 in size with the (111) face at the surface and heated by directly passing a current using the procedure described in [3]. The temperature was measured by a micropyrometer and by a linear extrapolation of the curve of temperature vs. ribbon heating current in the nonpyrometric region. Silver was deposited uniformly from thin metal filaments on the entire working surface of the ribbon. After training the source, only Auger peaks of silver were detected in the deposited layers.

The results of annealing a silver film ~ 1.5–2 monolayers in thickness deposited at room temperature on the surface of a 2DGF on iridium are displayed in Fig. 1. It is evident that the Auger signal of silver slightly varies up to temperatures of ~ 900 K and sharply drops

to zero at $T > 900$ K. In our opinion, this means that silver, which occurs on the graphite surface apparently as three-dimensional islands [9], is fully desorbed from the surface at the given temperature. In this case, Ag atoms do not penetrate under the graphite film to the intercalated state, because otherwise a distinct Auger signal of silver, though screened by graphite, would be undoubtedly observed. Furthermore, the graphite layer would prevent desorption, letting silver retain at the surface up to higher temperatures (see below) as was observed previously for Cs, K, and Ba [2]. The direct depositing of silver at temperatures above 900 K also leads to neither the appearance of its Auger signal nor a change in the intensities of Auger signals from the graphite film and the metal substrate.

This behavior is inherent only in silver atoms. All the other atoms that we studied under similar conditions intercalated under a 2DGF on a metal and accumulated under it in significant concentrations. By now, silver atoms are the only ones of many atoms examined in our studies that do not penetrate spontaneously under a graphite monolayer on a metal.

In spite of the fact that silver atoms do not intercalate directly a graphite monolayer on iridium, it seemed extremely interesting to accomplish intercalation of this kind. We found the conditions necessary for this purpose: it turned out that this is possible if silver is deposited on a graphite film previously intercalated by Cs to saturation, that is, containing intercalated (residing under the film) and adsorbed (lying on it) Cs atoms in approximately equal concentrations $N_{Cs} = (3–4) \times 10^{14}$ cm^{-2}.

The results of annealing such an adsorption system are presented in Fig. 2. The Auger signal of the substrate at room temperature is screened by two cesium layers and one silver layer, whereas the Auger signal of carbon is screened by a cesium monolayer and by the deposited silver. It is evident that the Auger signal of carbon completely regains its original value and remains unchanged up to $T = 1900$ K. This gives evidence that no adsorbates exist in the system over the graphite film at $T > 1100$ K. At the same temperatures, the Auger signal of cesium disappears and the signal of silver considerably decreases; however, the latter is retained at a definitely measurable level up to temperatures of 1900 K. Note for comparison that silver is fully desorbed from pure iridium in the absence of a graphite film at $T = 1100$ K within times on the order of 10 s.

To discuss the physical description of the process, note that a cesium film on a 2DGF in the absence of silver behaves as follows: heating up to $T = 700–800$ K leads to the complete desorption of Cs atoms lying on the graphite film and to a decrease in their concentration under this film down to the value $N_{cs} = 1 \times 10^{14}$ cm^{-2}. The intercalated Cs atoms that remained under the film turn out to be walled up there and are retained up to temperatures of 2000 K, at which these atoms are desorbed simultaneously with the thermal destruction of

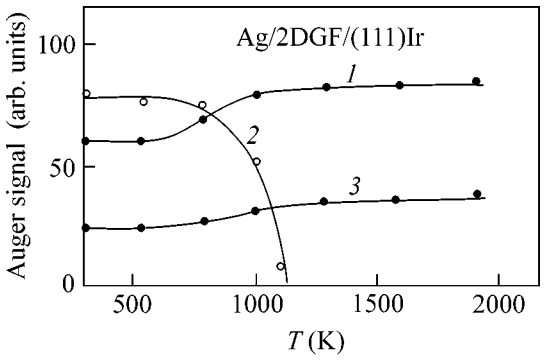

Fig. 1. Variations of Auger signals of (*1*) carbon, (*2*) silver, and (*3*) iridium in stepwise (with a spacing of 100 K) annealing of a silver film deposited on a 2DGF at room temperature. Annealing at each temperature for ~ 30 s.

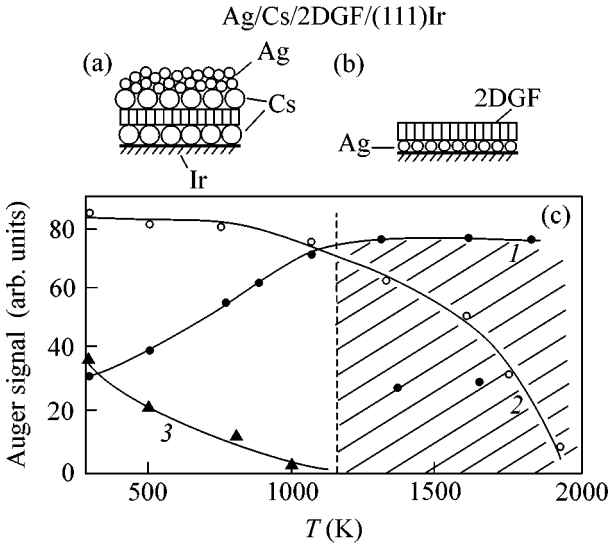

Fig. 2. Transformation of a silver film (2–3 monolayers) deposited at 300 K on a 2DGF with cesium intercalated to saturation. (a) and (b) structure of an adsorbed layer (a) before and (b) after heating; (c) variations of the Auger signals of (*1*) carbon, (*2*) silver, and (*3*) cesium in stepwise heating. Annealing at each temperature for 30 s.

the graphite film. The physical pattern described above was confirmed many times in our previous studies using Auger electron spectroscopy, thermal desorption spectroscopy, and catalytic dissociation of CsCl molecules [2–4].

Consider now the physical pattern of the processes that occur in annealing a silver film deposited on a 2DGF intercalated with Cs. The corresponding schematic drawings are presented in Figs. 2a and 2b. The adsorption of cesium at room temperature leads to both its intercalation under the 2DGF, where it resides with a concentration of $\sim(3–4) \times 10^{14}$ cm^{-2}, and its accumulation in the layer adsorbed over the graphite film with

approximately the same concentration [2]. The deposited silver is arranged over the graphite film and, possibly, chemically reacts with cesium (Fig. 2a). At temperatures of ~800–900 K, all the adsorbed cesium has probably left the surface already [2] and silver turns out to be adsorbed directly on the graphite surface apparently as droplets [11-12]. The occurrence of cesium in the annealing process opens the way for silver atoms to the intercalated state, where silver atoms accumulate and displace cesium to the surface, from where it desorbs rapidly (Fig. 2b). At $T > 1100$ K, all the impurity atoms (both Cs and Ag) are desorbed from the graphite surface and the silver atoms which arrived at the intercalated state remain walled up there and "live" up to very high temperatures, because the graphite layer prevents their desorption.

Thus, three new interesting phenomena have been observed: (1) the absence of the intercalation of a 2DGF on (111)Ir with silver atoms, (2) the occurrence of intercalation of this kind in the coadsorption of silver and cesium on a 2DGF on (111)Ir, and (3) the displacement of cesium from the intercalated state by silver atoms to the surface of the graphite film. It may be suggested that similar regularities of intercalation can also be expected for other atoms with intermediate ionization potentials (for example, rare earth elements).

This work was supported by the Russian State Program "Physics of Solid-State Nanostructures," project no. 99-2039.

REFERENCES

1. E. V. Rut'kov and A. Ya. Tontegode, Pis'ma Zh. Tekh. Fiz. **7**, 1122 (1981) [Sov. Tech. Phys. Lett. **7**, 480 (1981)].
2. A. Ya. Tontegode and E. V. Rut'kov, Usp. Fiz. Nauk **163**, 57 (1993) [Phys. Usp. **36**, 1053 (1993)].
3. N. R. Gall, E. V. Rut'kov, and A. Ya. Tontegode, Int. J. Mod. Phys. B **11**, 1765 (1997).
4. A. Ya. Tontegode, Prog. Surf. Sci. **38**, 201 (1991).
5. M. Eizenberg and J. M. Blakely, Surf. Sci. **82**, 228 (1979).
6. Hu Zi-Pu, D. F. Ogletree, M. A. Van-Hove, and G. A. Somorjai, Surf. Sci. **180**, 433 (1987).
7. R. Rossei, M. De Crescenzi, F. Sette, *et al.*, Phys. Rev. B **28**, 1161 (1983).
8. E. V. Rut'kov, A. Ya. Tontegode, and M. M. Usufov, Phys. Rev. Lett. **74**, 758 (1995).
9. M. S. Dresselhaus and G. Dresselhaus, Adv. Phys. **30**, 139 (1981).
10. N. R. Gall, S. N. Mikhailov, E. V. Rut'kov, and A. Ya. Tontegode, Surf. Sci. **191**, 185 (1987).
11. E. Ganz and K. Settler, Surf. Sci. **219**, 33 (1989).
12. C. Park, Surf. Sci. **203**, 395 (1988).

Translated by A. Bagatur'yants

JETP Letters, Vol. 75, No. 1, 2002, pp. 29–33. Translated from Pis'ma v Zhurnal Éksperimental'noĭ i Teoreticheskoĭ Fiziki, Vol. 75, No. 1, 2002, pp. 31–35.

Cyclotron Resonance for Electrons over Helium in a Resonator

V. B. Shikin

Institute of Solid State Physics, Russian Academy of Sciences, Chernogolovka, Moscow region, 142432 Russia

Received November 6, 2001; in final form, November 22, 2001

The cyclotron resonance (CR) problem for electrons over a helium film occupying the lower part of a resonator is solved. This problem is shown to represent an example of the well-known problem on the behavior of a system of coupled oscillators. For such oscillators, the coupling constant is determined as a function of the problem parameters with its minimal value in zero magnetic field and its maximal value at resonance conditions, when the cyclotron frequency coincides with one of the resonator modes. The details of the CR absorption of microwave energy by the coupled system formed by 2D electrons and a resonator are calculated. The results are discussed in application to the known CR experiments with electrons over helium. © *2002 MAIK "Nauka/Interperiodica".*

PACS numbers: 76.40.+b

The cyclotron resonance (CR) represents one of the basic techniques for studying the dynamics and the kinetic characteristics of various nondegenerate conducting systems. Its main properties are adequately determined in the Drude single-electron approximation:

$$j_x(\omega, \omega_c) = (\sigma'_{xx} + i\sigma''_{xx})E_\parallel, \tag{1}$$

$$\sigma'_{xx} = \frac{n_i e^2 \tau}{m} \frac{(1 + \omega^2\tau^2 + \omega_c^2\tau^2)}{(1 - \omega^2\tau^2 + \omega_c^2\tau^2)^2 + 4\omega^2\tau^2}, \tag{2}$$

$$\sigma''_{xx} = -(\omega\tau)\frac{n_i e^2 \tau}{m} \frac{(1 + \omega^2\tau^2 - \omega_c^2\tau^2)}{(1 - \omega^2\tau^2 + \omega_c^2\tau^2)^2 + 4\omega^2\tau^2}, \tag{2a}$$

where τ is the cyclotron relaxation time, $E_\parallel$ is the effective electric field in the sample, n_i is the free carrier density (three- or two-dimensional one), and ω and ω_c are the external and cyclotron frequencies of the problem.

At fixed values of ω and $E_\parallel$, the absorption of the microwave energy, $\dot{W}$, which is defined as

$$\dot{W} = \mathrm{Re}[E_\parallel j_x^*(\omega, \omega_c)], \tag{3}$$

contains information on the effective mass of a charge carrier (the position of the CR peak on the "magnetic axis", when measured in a varying magnetic field) and on the elastic relaxation time. This characteristic originates from the comparison of the halfwidth of the absorption line and the CR line with its height and, according to Eqs. (1)–(3), proves to be independent of the electron density.

In practice, one often deals with systems of finite density. In addition, to increase the sensitivity, the samples are placed in various kinds of microwave resonators (see the classical paper [1] on the CR in semiconductors and the papers [2–8] on the CR for electrons over helium). As a result, different corrections arise in the main scenario determined by Eqs. (1)–(3). For example, already the first publications describing the use of CR for measuring the electron and hole masses in semiconductors mentioned the possible shift of the CR line because of the "depolarization effect." Later on, this phenomenon was called the magnetoplasma effect. It consists in the plasma oscillations that accompany the excitation of the CR in finite samples. In this case, the combined resonance frequency ω_{cp} takes the form

$$\omega_{cp}^2 = \omega_p^2 + \omega_c^2, \tag{4}$$

where ω_p is the characteristic plasma frequency of the sample, which interacts with the given field $E_\parallel$.

The magnetoplasma effect can be easily taken into account by introducing the frequency ω_{cp} instead of ω_c in Eqs. (1) and (2). This effect is readily identified and is the object of numerous special studies (see [9–11]).

Another example of the perturbation of the CR dynamics is the dip effect for an electron over helium. According to the earlier publications [12, 13], the electron localization related to the deformation of the helium surface under it leads to a shift of the electron resonance frequency in a magnetic field:

$$\omega_{cd}^2 = \omega_d^2 + \omega_c^2,$$
$$\omega_d^2 = e^2 E_\perp^2 / 2\pi\alpha m l_H^2, \quad l_h^2 = c\hbar/eH. \tag{5}$$

0021-3640/02/7501-0029$22.00

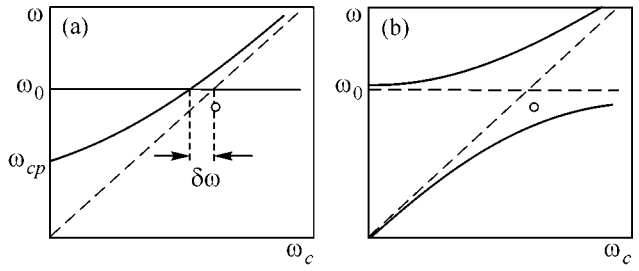

Fig. 1. (a) Schematic illustration of the resonance frequency shift in the 2D electrons–resonator system in the conditions of the effective renormalization for the eigenfrequency of electron oscillations: ω_c, ω_{cp}, and ω_0 are the cyclotron frequency, the combined frequency [Eq. (4)], and the eigenfrequency of the resonator; the point marked as zero corresponds to the reference point for the shift $\delta\omega$. (b) The anticrossing of the resonator eigenfrequency ω_0 and the electron cyclotron frequency ω_c.

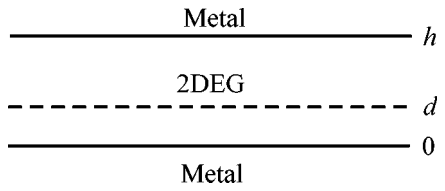

Fig. 2. Schematic representation of a resonator with a 2D electron system.

Here, ω_d is the eigenfrequency of the electron oscillations in the dip, $E_\perp$ is the pressing electric field strength, and α is the surface tension.

However, not all corrections fit in the pattern given by Eqs. (1)–(5) and adopted by the authors of the aforementioned paper [1]. When studying free carriers in resonators, one encounters some additional phenomena that affect the position and shape of the CR line and require their explicit introduction in the problem of the resonator dynamics to obtain a correct description. Qualitatively, the origin of such corrections is evident from Fig. 1. Figure 1a illustrates the formation of the shift $\delta\omega$ in the pattern given by Eqs. (1)–(5). Here, the resonator frequency is fixed and the shift occurs because of the nonlinear behavior of ω_{cd} [from Eqs. (5)] or ω_{cp} [Eq. (4)] with varying magnetic field.

Figure 1b presents the actual behavior of the resonator frequency and the frequency of an oscillating electron as functions of magnetic field in the presence of coupling between the oscillators. In the region of anticrossing, which results from the intersection of terms, the position of the resonance and its line shape deviate from the initial ones corresponding to the point marked as zero.

As far as the author of this paper knows, the scales of the anticrossing that accompanies the excitation of CR for electrons in a resonator have not yet been estimated. The solution of this problem is described below for the simplest model that retains all components of the electrons–resonator system.

1. Let us first consider an empty resonator formed by two infinite metal plates with the coordinates $z = 0$ and $z = h$ (Fig. 2). The principal E mode with $E_z = 0$, $E_y = 0$, and $E_x(z) \neq 0$ and with the boundary conditions

$$E_x(0) = 0, \quad E_x(h) = 0$$

has the structure

$$E_x(z) = E_o \sin(\pi z/h), \quad \omega_o/c = \pi/h, \tag{6}$$

where c is the velocity of light.

The same problem considered in the presence of 2D electrons localized with the density n_s along the plane $z = d$ becomes somewhat complicated. In this case, the electric field has two components: $E_x(z)$ in vacuum and $\epsilon_x(z)$ in the helium film. The dielectric constant of the latter is taken equal to unity for simplicity:

$$E_x(z) = E_1 \sin kz + E_2 \cos kz, \quad d \le z \le h, \tag{7}$$

$$\epsilon_x(z) = \epsilon_1 \sin kz + \epsilon_2 \cos kz, \quad 0 \le z \le d, \qquad k = \omega/c, \tag{8}$$

$$\epsilon_x(0) = 0, \quad E_x(h) = 0, \quad \epsilon_x(d) = E_x(d). \tag{9}$$

In addition, a vortex magnetic field with the components $h_y(H)$ and $H_y(z)$ appears in the problem. The discontinuity of this field at the boundary $z = d$ is related to the 2D electron current along the helium surface:

$$\partial\epsilon_x/\partial z = -ikh_y, \quad \partial E_x/\partial z = -ikH_y, \tag{10}$$

or

$$-ih_y = \epsilon_1 \cos kz - \epsilon_2 \sin kz, \qquad -iH_y = E_1 \cos kz - E_2 \sin kz; \tag{11a}$$

$$H_y(d) - h_y(d) = 4\pi j_x(d)/c, \tag{11b}$$

$$j_x(d) = \sigma_{xx} E_x(d), \quad \sigma_{xx} = \sigma'_{xx} + i\sigma''_{xx}. \tag{12}$$

Here, the components of the conductivity σ_{xx} are taken from Eqs. (2) and (2a).

Four boundary conditions [three from Eqs. (9) and one from Eqs. (11a) and (11b)] being set for the four coefficients ϵ_1, ϵ_2, E_1, and E_2 form a homogeneous system of equations, whose solution determines the principal E mode of an electron-loaded resonator:

$$f(kh, kd, \sigma) = 0,$$

$$f(kh, kd, \sigma) = \sin(kh) - i\sigma \sin(kd) \times [\sin(kd)\cos(kh) - \cos(kd)\sin(kh)], \tag{13}$$

$$\sigma = 4\pi\sigma_{xx}/c, \quad k = \omega/c.$$

Let us consider some limiting cases. When $\sigma \longrightarrow 0$, Eq. (13) is reduced to

$$\sin(kh) \simeq 0, \quad k_o = \pi/h. \tag{13a}$$

This result coincides with Eqs. (5). In the opposite limit $\sigma \longrightarrow \infty$, Eq. (13) is meaningful only when

$$[\sin(kd)\cos(kh) - \cos(kd)\sin(kh)] = 0 \quad \text{or} \quad k_1 = \pi/(h-d). \tag{13b}$$

It is also possible that the following factor is zero:

$$\sin(k_2 d) = 0, \quad k_2 = \pi/d. \tag{13c}$$

The two results are easily understood, because in the presence of a conducting plane $z = d$, two new resonators with the eigenfrequencies given by Eqs. (13b) and (13c) are formed instead of a single resonator.

If we take $n_s \approx 10^8$ cm^{-2} and $\tau \le 10^{-7}$ (which is typical of electrons over helium), the combination

$$\sigma_o = 4\pi\sigma_{xx}^o/c, \quad \sigma_{xx}^o = n_s e^2\tau/m \tag{14}$$

will be characterized by a scale close to unity. In other words, a renormalization of the resonator spectrum under the effect of 2D electrons is actually quite possible.

Let us estimate the scale of coupling for a conducting sample filling the whole volume of the resonator. This problem, being related to the CR measurements in semiconductors, is reduced to solving the equations that determine the skin depth in a bounded conducting medium. Performing the necessary calculations, we arrive at the expression

$$k^2 = \kappa\frac{\omega^2}{c^2} + \frac{4\pi i\sigma_{xx}^{(3)}}{c^2}\omega = \pi^2/h^2, \tag{15}$$

where κ is the dielectric constant of the sample.

According to Eq. (15), the coupling constant for three-dimensional samples approaches unity when the skin depth becomes equal to the distance h between the resonator plates. For samples with $\omega\tau \ge 1$, $h \sim 1$ cm, and $m^* \sim 0.1m$ (where m is the electron mass in vacuum), this condition is satisfied when the electron density is higher than 10^{12} cm^{-3}. The experiments described in [1] were performed with lower electron densities.

The comparison between the coupling scales (14) and (15) in systems of different dimension shows that, for the same value $h \sim 1$ cm and the same average distance r_s between the conducting electrons ($r_s \sim 10^{-4}$ cm), the characteristic relaxation times for electrons over helium are much (approximately two to three orders of magnitude) longer than the relaxation times in semiconductors. This explains the much greater scale of the 2D anticrossing, as compared to its three-dimensional analog.

Returning to the 2D case, we consider the limit $\sigma_o \ll 1$ in more detail. In this region, the initial transcendental equation (13) can be linearized. Assuming that the expressions

$$k = k_o + \delta k, \quad \sin k_o h = 0, \quad k_o \gg \delta k = \delta k' + i\delta k'', \tag{16}$$

[where k_o is determined by Eqs. (13a)] are valid, we obtain

$$\sigma k' \simeq \frac{\sigma_* \sqrt{x_o}(1 + x_o - y)}{h[(1 - x_o + y)^2 + 4x_o]}, \tag{16a}$$

$$\delta k'' \simeq -\frac{\sigma_*(1 + x_o + y)}{h[(1 - x_o + y)^2 + 4x_o]}, \tag{16b}$$

$$x = \omega^2\tau^2; \quad x_o = \omega_o^2\tau^2;$$

$$y = \omega_c^2\tau^2; \quad \sigma_* = \sigma_0 \sin^2 k_o d.$$

The function $\delta k'$ gives an idea of the behavior of the real part of the spectrum shown in Fig. 1b for finite values of the relaxation time. In this case, the asymptotic extensions of the two spectrum branches shown in Fig. 1b do not go to infinity, but smoothly pass into one another by going through zero at the point

$$y = 1 + x_o \tag{17}$$

and displaying two extrema at the points

$$y_\pm = 1 + x_o \pm 2\sqrt{(1 + x_o)}.$$

As for the function $\delta k''$, it has an extremum at the point

$$y = x_o - 1/4x_o, \quad x_o \gg 1, \tag{18}$$

which is close to the point determined by Eq. (17).

The similarity of dependences (16b) and (3) suggests that Eqs. (1)–(3) are equivalent to the more detailed calculations by Eqs. (6)–(16). However, the function $\delta k''$ given by Eq. (16b) is not the only one responsible for the details of absorption. As will be seen below, the effective field $E_\parallel$ from Eq. (3), which occurs at the charged surface of helium in the resonator, cannot be considered as a preset quantity. It must be calculated self-consistently and proves to depend in a resonance way on the external pumping amplitude. This statement, along with the anticrossing effect, is of most interest in the proposed pattern of the behavior of the electrons–resonator system and deserves special attention.

2. To reveal the properties of the field $E_\parallel$, it is necessary to go beyond the limits of the homogeneous spectral problem by including the pumping mechanism and the calculation of the actually observed quantities (e.g., the microwave signal reflection from the resonator) in the consideration. To realize this program with retaining the relative simplicity of the geometry shown in Fig. 2 along with the evidence of finite results, it is

expedient to use a simplified coupling between the resonator and the waveguide; namely, we introduce a finite electromagnetic transparency of the upper plate of the resonator and the corresponding probability for the penetration of part of the microwave signal, which is incident from outside on the plane $z = h$, inside the resonator.

Assume that the external field $T(z)$ has the structure

$$T_x(z) = E_o[\exp(+ik(z-h)) - R\exp(-ik(z-h))], \quad +\infty > z > h, \tag{19}$$

where E_o is the amplitude of the exciting field and R is the coefficient of reflection of the external signal from the plane $z = h$. Sewing together the external fields with their continuation in the resonator [specifically, the field $E_x(z)$ from Eq. (7)] at the aforementioned boundary by imposing the conditions

$$T_x(h) = E_x(h)$$
$$\text{and } H_y(h+0) - H_y(h-0) = 4\pi j_x^o(h)/c, \tag{20}$$
$$j_x^o(h) = \sigma_{xx}^m T_x(h)$$

(σ_{xx}^m is the finite conductivity of the upper electrode in Fig. 2), we arrive at the following expression for the coefficient R:

$$R = \frac{\gamma - i}{\gamma + i},$$
$$\gamma = \sigma_m + \frac{\cos(kh) + \sigma\sin(kd)\cos k(h-d)}{f(kh, kd, \sigma)}, \tag{21}$$
$$\sigma_m = \frac{4\pi}{c}\sigma_{xx}^m.$$

Here, the function $f(kh, kd, \sigma)$is determined by Eq. (13).

Evidently, when $\sigma_{xx}^m \longrightarrow \infty$, the reflection coefficient from Eqs. (21) tends to unity. When σ_{xx}^m is finite, the quantity R is sensitive to the resonator properties. In particular, for an empty resonator when $\sigma_{xx} \longrightarrow 0$, we have

$$R_o = \frac{\gamma_o - i}{\gamma_o + i}, \quad \gamma_o = \sigma_m + \cot(kh). \tag{21a}$$

If, in this case, the external frequency additionally satisfies the requirement

$$\sin(k_o h) \longrightarrow 0, \tag{22}$$

we obtain

$$R_o \longrightarrow 1 \tag{22a}$$

even when the conductivity of the upper electrode is limited (the total reflection of the external signal occurs at the lower plate of the resonator). Evidently, the resonance condition (22) coincides with Eq. (6).

The limiting form of R_o given by Eq. (21a) must be tested by special experiments, because the phenomenological conductivity σ_{xx}^m involved in Eqs. (21) is responsible for the coupling between the waveguide and the resonator.

As for the general form of R from Eqs. (21), its study represents an independent problem (a routine and fairly cumbersome one) that contains several external parameters. We only note that the structure of ReR from Eqs. (21) is more complicated than the structure of Eqs. (3) and (16b) for the reasons indicated above; the field $E_\parallel$ is not fixed, as in Eq. (3), but related to the pumping amplitude E_o in a resonance way. With R being determined, it is possible to represent this relation in an explicit form:

$$E_\parallel = E_o(1-R)\sin(kd)/f(kh, kd, \sigma), \tag{23}$$

where $f(kh, kd, \sigma)$ is determined from Eqs. (13). In addition, the resonance frequency is a floating function of external parameters. As a result, the microwave energy absorption is sensitive to the thickness of the helium film, the electron density, the degree of coupling with the waveguide, and the measurement procedure (the experiment can be performed at a fixed pumping frequency with a search for the resonance in varying magnetic field, or at a fixed magnetic field with a pumping frequency sweep). All these factors are absent in the CR pattern determined by Eqs. (1)–(3).

3. Thus, this paper solves the problem on the structure of the principal E mode of a strip-type resonator of infinite length with a 2D electron layer inside it and with an arbitrary magnetic field applied normally to the plane of the 2D system. The solution is based on the consideration of coupled oscillations of two oscillators, one of which is represented by the resonator mode and the other by the cyclotron motion of the electrons. The effective coupling constant, whose explicit form follows from the solution of the problem [see the expression for σ from Eqs. (13)], is found to be a varying quantity that passes through its maximum in the cyclotron resonance conditions and is sufficiently large to make the anticrossing effect noticeable in the behavior of the modes of the 2D-electron-loaded resonator [see Fig. 1b and Eq. (16a) describing the explicit behavior of the real part of the resonator spectrum].

The properties of the real part of the microwave energy absorption, ReR, by the electrons in the resonator are discussed in detail. The difference between its conventional, Eq. (3), and sequential, Eqs. (21), definitions is determined by the necessity of an accurate calculation of the effective field $E_\parallel$ at the charged surface of liquid helium in the resonator. As a result, the absorption line shape of the electron-loaded resonator proves to depend on the helium film thickness, the electron density, and the degree of coupling with the waveguide. These factors are absent in the description based on Eqs. (1)–(3), but they are present in the exper-

iments [4, 5]. Specifically, note the sharp decrease in the absorption observed with decreasing film thickness in one of the aforementioned experiments [4]. This effect is not described by system (1)–(3), whereas it is easily explained with allowance for the actual behavior of $E_\parallel$, according to Eq. (23). It is also of interest to discuss the paradox from the cited paper [4]. It was shown that, in the crystalline state, the 2D system exhibits increasing absorption with increasing electron density (see Fig. 3 from [5]). This statement contradicts common sense (with increasing density, an electron crystal must acquire dielectric properties and, hence, become less absorbing), as well as the corresponding calculations [14]. The resolution of the paradox again lies in the specific features of the 2D electron behavior in the resonator. The actual conductivity of an electron crystal obviously decreases with increasing density. However, according to Eq. (23), the field $E_\parallel$ increases (remember that, in the case of infinite conductivity of the 2D system, we have $E_\parallel \longrightarrow 0$). As a result, the effective absorption, which is proportional to $E_\parallel^2$, proves to be an increasing function of the electron density.

The results of this study can be useful for solving the old problem of explaining the origin of the CR line shift observed in the experiments [4]. This phenomenon consists in the regularly observed shift of the CR line toward smaller (compared to its unperturbed position) magnetic fields, and the value of this shift is approximately proportional to the square of the electric field $E_\perp$ pressing the electrons toward the helium surface. The popular interpretation of this phenomenon [4, 12, 13] suggests the formation of a dip under each electron with the eigenfrequency of electron oscillations proportional to the square of $E_\perp$ [see Eqs. (5)]. However, the following studies showed that, firstly, according to [15], the probability of the formation of a single-electron dip at the temperatures used in [4] is negligibly small. Secondly, this process has a threshold in $E_\perp$, which was not observed in [4]. Finally, according to the experiments [16–18], the dips on the helium surface appear and disappear only when the crystallization conditions are satisfied for the 2D electron system. It should also be mentioned that the data presented in [5] indicate (as in [4]) the presence of a shift of the CR line, but only in the electron crystallization region. Thus, the "dip-based" interpretation of the CR line shift [4] in the absence of Coulomb ordering should be abandoned, although, as yet, it has no alternative. The inclusion of the anticrossing in the consideration offers the possibility of eliminating the difficulties in interpreting the data [4] obtained for low densities of 2D electrons.

The real part of the reflection is virtually a blank spot in the experimental part of the problem under discussion. One should note only the publication [19] that discusses this part of the impedance of an electron-loaded resonator without offering any adequate interpretation. At the same time, combined measurements of both parts of the reflection (transmission) coefficient are very desirable, because these quantities contain several parameters, namely, the relaxation time, the average electron density, and the effective thickness of the helium film, whose values must be derived from the experimental data.

I am grateful to V.F. Gantmakher for discussing the results and for valuable comments. The work was supported in part by the INTAS Network, project no. 97-1643, and by the Russian Foundation for Basic Research, project no. 02-02-17082.

REFERENCES

1. G. Dresselhaus, A. Kip, and K. Kittel, Phys. Rev. **98**, 368 (1955).
2. C. C. Grimes and T. Brown, Phys. Rev. Lett. **32**, 280 (1974).
3. V. S. Édel'man, Pis'ma Zh. Éksp. Teor. Fiz. **24**, 510 (1976) [JETP Lett. **24**, 468 (1976)]; Pis'ma Zh. Éksp. Teor. Fiz. **26**, 647 (1977) [JETP Lett. **26**, 493 (1977)].
4. V. S. Édel'man, Zh. Éksp. Teor. Fiz. **77**, 673 (1979) [Sov. Phys. JETP **50**, 338 (1979)].
5. L. Wilen and R. Gianetta, Phys. Rev. Lett. **60**, 231 (1988).
6. E. Teske, Yu. Monarkha, M. Seck, and P. Wyder, Phys. Rev. Lett. **82**, 2772 (1999).
7. Yu. Monarkha, E. Teske, and P. Wyder, Phys. Rev. B **59**, 14884 (1999).
8. Yu. Monarkha, E. Teske, and P. Wyder, Phys. Rev. B **62**, 2593 (2000).
9. E. Batke, D. Heitman, and J. Kotthaus, Phys. Rev. Lett. **54**, 2367 (1985).
10. D. Glattli, E. Andrei, G. Devile, *et al.*, Phys. Rev. Lett. **54**, 1710 (1985).
11. E. Batke, D. Heitman, and C. Tu, Phys. Rev. B **34**, 6951 (1986).
12. V. Shikin, Zh. Éksp. Teor. Fiz. **60**, 713 (1971) [Sov. Phys. JETP **33**, 387 (1971)].
13. A. Cheng and P. Platzman, Solid State Commun. **25**, 813 (1978).
14. M. Dykman, J. Phys. C **15**, 7397 (1982).
15. F. Peeters and S. Jackson, Phys. Rev. B **34**, 1539 (1986).
16. F. Gallet, G. Deville, A. Valdes, and F. Williams, Phys. Rev. Lett. **49**, 212 (1982).
17. G. Deville, A. Valdes, E. Andrei, and F. Williams, Phys. Rev. Lett. **53**, 588 (1984).
18. D. Glattli, E. Andrei, and F. Williams, Phys. Rev. Lett. **60**, 420 (1988).
19. G. Mistura, T. Gunzler, S. Neser, and P. Leiderer, Phys. Rev. B **56**, 8360 (1997).

Translated by E. Golyamina

JETP Letters, Vol. 75, No. 1, 2002, pp. 34–36. From Pis'ma v Zhurnal Éksperimental'noĭ i Teoreticheskoĭ Fiziki, Vol. 75, No. 1, 2002, pp. 36–38.

Shifting the Quantum Hall Plateau Level in a Double Layer Electron System[1]

E. V. Deviatov*, A. A. Shashkin*, V. T. Dolgopolov*, H.-J. Kutschera, A. Wixforth**, K. L. Campman***, and A. C. Gossard*****

**Institute of Solid-State Physics, 142432 Chernogolovka, Moscow region, Russia*

*** Ludwig-Maximilians-Universität, D-80539 München, Germany*

**** Materials Department and Center for Quantized Electronic Structures, University of California, 93106, Santa Barbara, California USA*

Submitted December 6, 2001

We study the plateaux of the integer quantum Hall resistance in a bilayer electron system in tilted magnetic fields. In a narrow range of tilt angles and at certain magnetic fields, the plateau level deviates appreciably from the quantized value with no dissipative transport emerging. A qualitative account of the effect is given in terms of decoupling of the edge states corresponding to different electron layers/Landau levels. © *2002 MAIK "Nauka/Interperiodica"*.

PACS numbers: 73.43.-f; 72.20.My

Double-layer electron systems are attracting much interest by the presence of an additional degree of freedom associated with the third dimension. Strong interlayer correlations give rise to the appearance of novel states that are not observed in single-layer systems: (i) the even-denominator fractional quantum Hall effect [1–3], (ii) the many-body integer quantum Hall effect [4, 5], and (iii) broken-symmetry states [6]. All the states manifest themselves as quantum plateaux in the Hall resistance ρ_{xy} accompanied by zeroes in the longitudinal resistivity ρ_{xx}. Driving the system out of the dissipationless regime leads to deviations of ρ_{xy} from the quantized value; i.e., the behavior of ρ_{xy} is correlated with that of ρ_{xx}. A deviation of the quantum Hall plateau at filling factor $\nu = 3/2$ from the quantized value accompanied by nonzero ρ_{xx} was observed in a bilayer system with asymmetric hole density distributions [7]. Peaks at the low-field edge (so-called overshoots) of the quantum Hall plateaux, along with corresponding peaks in ρ_{xx}, were observed in wide parabolic GaAs quantum wells in the two-subband regime [8]. Similar overshoots were previously reported in GaAs/AlGaAs heterostructures with one occupied subband and explained in terms of decoupling/depopulation of the edge state associated with the topmost Landau level [9]. Normally, additional features on the quantum Hall plateau are comparable to corresponding ones in ρ_{xx}. However, whether or not the accuracy of the Hall resistance quantization is related solely to dissipative effects at this point is unclear. In principle, decoupling of the edge states can lead to a shift of the plateau level in the absence of dissipative transport as well. In the simplest case of a double layer electron system with two layers being in different quantum Hall states, the decoupling of the edge states belonging to different layers can be easily controlled, e.g., by the application of an in-plane magnetic field [8, 10].

Here, we perform precision measurements of the quantized Hall resistance at an integer filling factor in a double layer electron system in tilted magnetic fields. In a narrow region of tilt angles and at certain magnetic fields, we observe pronounced deviations of the quantum Hall plateau from the quantized value which are not accompanied by any additional features in the dissipative resistivity. The results are qualitatively explained by decoupling of the edge states corresponding to different electron layers/Landau levels, although the sensitivity of the effect to both tilt angle and magnetic field is unclear.

The samples are grown by molecular beam epitaxy on a semi-insulating GaAs substrate. The active layers form a 760-Å-wide parabolic well. In the center of the well a 3-monolayer-thick $Al_xGa_{1-x}As$ ($x = 0.3$) sheet is grown which serves as a tunnel barrier between both parts on either side. The symmetrically doped well is capped by 600-Å AlGaAs and 40-Å GaAs layers. The samples are $450 \times 50\ \mu m^2$ Hall bars that have a metallic gate on the crystal surface and ohmic contacts connected to both electron systems in two parts of the well. Applying a dc voltage between the well and the gate enables us to tune the carrier density in the well. The sample is placed in the mixing chamber of a dilution refrigerator with a base temperature of about 30 mK, so that the normal to its surface is tilted with respect to the magnetic field. The longitudinal and Hall resistivities of the bilayer electron system are measured as a function

[1] This article was submitted by the authors in English.

of either magnetic field B or gate voltage V_g using a standard four-terminal lock-in technique at a frequency of 10 Hz. The excitation current is kept low enough to ensure that measurements are taken in the linear regime of response. The data are well reproducible in different coolings of the sample.

For additional magnetocapacitance measurements, a small ac voltage (2.4 mV) at frequencies in the range 3–600 Hz is applied between the well and the gate and both current components are measured. In the low frequency limit, the imaginary current component reflects the thermodynamic density of states in a double-layer electron system, whereas the active component of the current is inversely proportional to the dissipative conductivity (for details, see Ref. [11]).

The positions of the magnetocapacitance minima in the ($B_\perp$, V_g) plane for filling factor $\nu = 2$, 3, and 4 are shown in Fig. 1 by circles for different tilt angles Θ of the magnetic field. Another fan chart (not shown in the figure) is determined by magnetocapacitance minima corresponding to gaps in the spectrum of the front electron layer only; these two fan charts allow determination of the front layer depopulation voltage V_g = –200 mV (bilayer onset) and the voltage V_g = 100 mV at which the quantum well becomes symmetric (balance point) [11, 12]. As seen from Fig. 1, discontinuities on the fan chart lines for $\nu = 2$ and $\nu = 3$ emerge with increasing tilt angle. This behavior is identical with that reported earlier on similar samples with the same quantum well design and interpreted for $\nu = 2$ in terms of the formation of the canted antiferromagnetic phase [13].

In Fig. 2(a), we show the Hall resistance ρ_{xy} as a function of the magnetic field around filling factor ν = 3 for gate voltages between –170 and –120 mV at a tilt angle $\Theta = 53°$. There exists a pronounced peak on the quantum Hall plateau although the longitudinal resistivity ρ_{xx} zeroes nicely. (We have checked, with the help of the magnetocapacitance measurements, that the dissipative conductivity shows no additional features either.) This peak on the plateau is not sensitive to a variation of V_g so that at a fixed magnetic field within the peak, the dependence of ρ_{xy} on gate voltage has a plateau at a level above the quantized value; see Fig. 2b. Such a behavior of the $\nu = 3$ quantum Hall plateau is observed in a narrow range of tilt angles: it is present for $\Theta = 50°$ and $\Theta = 53°$, while at $\Theta = 45°$ and Θ = 66.5°, the $\nu = 3$ quantum Hall plateau is found to be featureless.

Similar shifts of the quantum Hall plateau level accompanied by good zeroes in ρ_{xx} are also observed at filling factor $\nu = 2$ for $\Theta = 45°$, see Fig. 3a. In addition, near the splitting of the $\nu = 2$ fan chart line that arises with increasing Θ (Fig. 1), an additional peak appears in both ρ_{xx} and ρ_{xy} on the shifted plateau; see Fig. 3b.

In this case, the appearance of dissipative transport is naturally reflected by ρ_{xy} behavior.

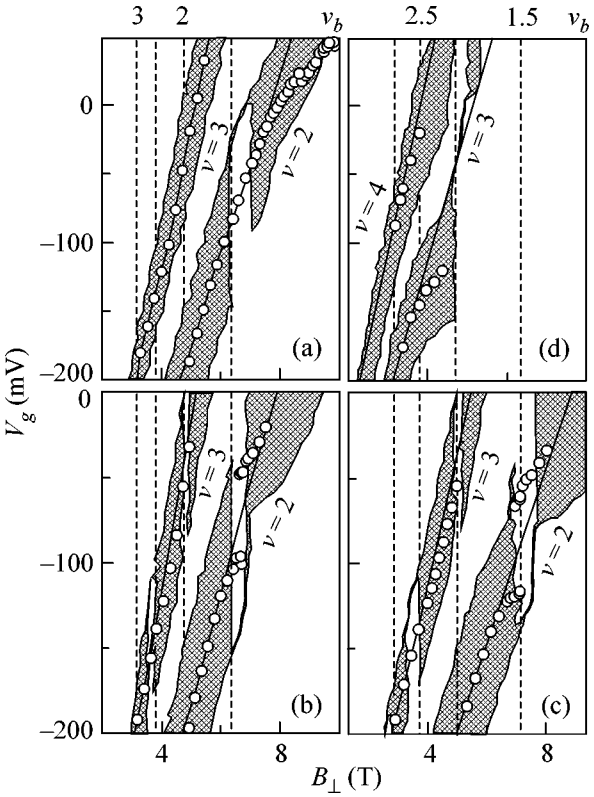

Fig. 1. Positions of the magnetocapacitance minima (circles) in the ($B_\perp$, V_g) plane for ν = 2, 3, and 4 at tilt angles (a) 45°, (b) 50°, (c) 53°, and (d) 66.5°. The dashed lines correspond to the indicated values of filling factor ν_b in the back electron layer. In the shaded areas, the deviation of ρ_{xy} from the quantized value does not exceed 0.05%

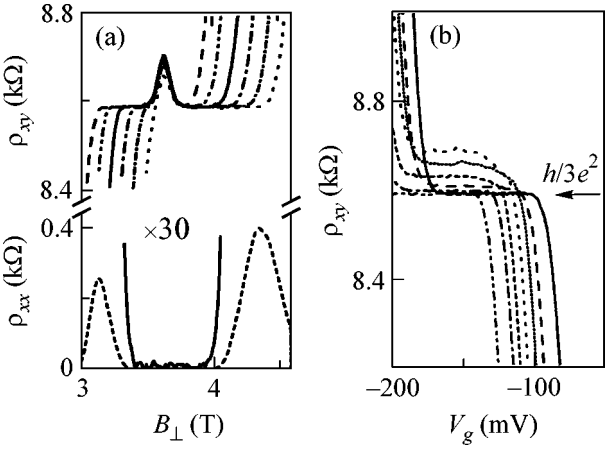

Fig. 2. Traces of ρ_{xy} for $\nu = 3$ at $\Theta = 53°$ as a function of $B_\perp$ at gate voltages –170, –160, –150, –140, –130, and –120 mV (a) and as a function of V_g at perpendicular components of the magnetic field 3.45, 3.55, 3.60, 3.65, 3.70, 3.75, and 3.85 T (b). Also shown in case (a) is the dependence of ρ_{xx} on $B_\perp$ at V_g = –150 mV

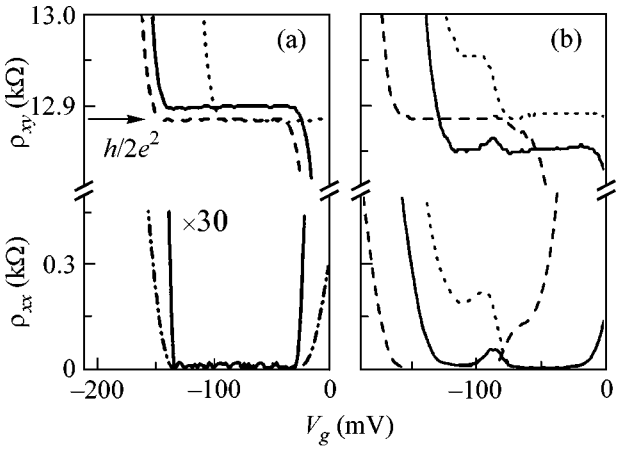

Fig. 3. Dependence of ρ_{xy} and ρ_{xx} on gate voltage for $\nu = 2$ at $\Theta = 45°$ for $B_\perp = 6.26$, 6.38, and 7.09 T and for $B_\perp = 6.50$ T, respectively (a) and at $\Theta = 53°$ for $B_\perp = 6.04$, 6.54, and 6.74 T (b)

The overall data on deviation of the quantum Hall plateaux from the quantized values are depicted in Fig. 1. The regions in which the plateau deviation does not exceed 0.05% are hatched. To our surprise, at some tilt angles these regions for the same ν are separated, forming regular vertical strips whose position corresponds to integer and half-integer filling factors ν_b in the back electron layer. Note that the electron density in this layer is practically unchanged with changing V_g because of the screening effect of the front electron layer.

In principle, one can expect possible shifts of the quantum Hall plateau level: at both integers ν_b and ν in an unbalanced bilayer electron system, two electron layers correspond to two lowest electron subbands with independent gaps in their spectrum at the Fermi level; i.e., the electron layers are independent. Therefore, the condition of inverse proportionality of their individual currents to ρ_{xy} can be broken, e.g., due to contact resistance, leading to distinct (decoupled) electrochemical potentials of the electron layers. Provided that the electrochemical potentials are not equilibrated along the edge of the sample including contact regions, the measured Hall resistance plateau can be above or below the quantized value even in the absence of dissipative transport. Similar arguments apply for the observed dissipationless states at noninteger ν_b and integer ν. In these states, the electron subbands are correlated as caused by wave function reconstruction in the unbalanced bilayer electron system [11, 12]. Subject to the absence of electrochemical potential equilibration between different Landau levels, the measured Hall resistance plateau can also be shifted.

However, from the above argumentation, it is not clear why deviations of the quantum Hall plateaux are observed in narrow intervals of the magnetic field that correspond to integer and half-integer filling factor ν_b. The sensitivity of the effect to the tilt angle of the magnetic field cannot be explained either. Thus, a more sophisticated interpretation of the experimental data is needed.

In summary, we have studied the behavior of the quantum Hall resistance plateaux at the integer filling factor in a bilayer electron system in tilted magnetic fields. In a narrow range of tilt angles and at magnetic fields corresponding to integer and half-integer filling factor ν_b, pronounced deviations of the quantum Hall plateau from the quantized value are observed which are not caused by dissipative transport. We give a qualitative account of the effect in terms of decoupling of the edge channels belonging to different electron layers/Landau levels, although its sensitivity to both tilt angle and magnetic field is unclear.

We gratefully acknowledge discussions with J.P. Kotthaus. This work was supported by the Deutsche Forschungsgemeinschaft, SFB grant no. 348; the Russian Foundation for Basic Research, projects nos. 01-02-16424 and 00-02-17294; and INTAS, grant no. YSF002. The Munich–Santa Barbara collaboration was also supported by a joint NSF–European grant and the Max-Planck research award.

REFERENCES

1. J. P. Eisenstein, G. S. Boebinger, L. N. Pfeiffer, *et al.*, Phys. Rev. Lett. **68**, 1383 (1992).
2. Y. W. Suen, L. W. Engel, M. B. Santos, *et al.*, Phys. Rev. Lett. **68**, 1379 (1992).
3. Y. W. Suen, H. C. Manoharan, X. Ying, *et al.*, Phys. Rev. Lett. **72**, 3405 (1994).
4. S. Q. Murphy, J. P. Eisenstein, G. S. Boebinger, *et al.*, Phys. Rev. Lett. **72**, 728 (1994).
5. T. S. Lay, Y. W. Suen, H. C. Manoharan, *et al.*, Phys. Rev. B **50**, 17725 (1994).
6. H. C. Manoharan, Y. W. Suen, T. C. Lay, *et al.*, Phys. Rev. Lett. **79**, 2722 (1997).
7. A. R. Hamilton, M. Y. Simmons, F. M. Bolton, *et al.*, Phys. Rev. B **54**, R5259 (1996).
8. K. Ensslin, A. Wixforth, M. Sundaram, *et al.*, Phys. Rev. B **47**, 1366 (1993).
9. C. A. Richter, R. G. Wheeler, and R. N. Sacks, Surf. Sci. **263**, 270 (1992).
10. S. R. Renn, Phys. Rev. B **52**, 4700 (1995).
11. V. T. Dolgopolov, A. A. Shashkin, E. V. Deviatov, *et al.*, Phys. Rev. B **59**, 13235 (1999).
12. E. V. Deviatov, V. S. Khrapai, A. A. Shashkin, *et al.*, Pis'ma Zh. Éksp. Teor. Fiz. **71**, 724 (2000) [JETP Lett. **71**, 496 (2000)].
13. V. S. Khrapai, E. V. Deviatov, A. A. Shashkin, *et al.*, Phys. Rev. Lett. **84**, 725 (2000).

JETP Letters, Vol. 75, No. 1, 2002, pp. 37–40. From Pis'ma v Zhurnal Éksperimental'noĭ i Teoreticheskoĭ Fiziki, Vol. 75, No. 1, 2002, pp. 39–43.

Base Pair Dynamic Assisted Charge Transport in DNA[1]

E. I. Kats*, ** and V. V. Lebedev*, ***

** Landau Institute for Theoretical Physics, Russian Academy of Sciences, ul. Kosygina 2, Moscow, 117940 Russia*

*** Institut Laue-Langevin, BP 156 Grenoble, France*

**** Department of Physics, Weizmann Institute of Science, 76100 Rehovot, Israel*

Submitted November 23, 2001

A one-dimensional model with time-dependent random hopping is proposed to describe charge transport in DNA. It permits the investigation of both diffusion of electrons and their tunneling between different sites in DNA. The tunneling appears to be strongly temperature-dependent. Observations of a strong (exponential) as well as a weak distance dependence of the charge transfer in DNA can be explained in the framework of our model. © *2002 MAIK "Nauka/Interperiodica".*

PACS numbers: 87.14.Gg; 34.70.+e

Electronic transport is the basis for a wide range of important biological processes in DNA. Besides, the phenomenon has a fundamental physical interest, since the transport properties of biomolecules are expected to differ considerably from those of macroscopic conductors. Lastly, very recently, material scientists have also turned their attention to charge migration in DNA for the development of DNA-based molecular technologies.

Although the first attempts to measure DNA conductivity [1] and to present a theory of the phenomenon [2] were made almost 40 years ago, the question concerning charge transport through DNA remains unsettled, and there is an impressive quantity of unexplained or partially explained data. Different publications frequently report contradictory results. Two kinds of techniques for acquiring information on charge transport in DNA are used. First, direct or indirect electrical conductivity measurements on micrometer-long DNA ropes are performed [3–7]. Experimental results obtained in this technique are ambiguous. DNA conductivity σ was reported as almost metallic, of the order $10^4\ \Omega^{-1}\ \mathrm{cm}^{-1}$[3] (in a recent publication [4], the authors claim they observed even proximity-induced superconductivity in DNA) or semiconducting with $\sigma \simeq 0.1\ \Omega^{-1}\ \mathrm{cm}^{-1}$ [6]. Very recently, experimental techniques have progressed to the point where the conductivity of individual 10-nm-long double-stranded molecules was measured [7], and the result implies that DNA is a good insulator. Clearly this frustrating situation with conductivity measurements means that there are many relevant factors which can influence the charge transport in DNA in different ways and which are hardly controlled in real experiments. The second technique, related to fluorescence quenching measurements on DNA strands doped with donor and acceptor molecules [8–23], seems more reliable, and it is our main concern here. In this technique, photoexcitation of a donor associated with the stack of base pairs in some fashion allows transfer of an electron to the stack. The migrating electron is trapped finally at the acceptor site, and charge transfer is monitored by the yield of a chemical reaction accompanying the trapping process. The transfer rate is usually assumed to be characterized by a simple exponential law $\exp(-\beta x)$, where x is the donor-acceptor separation. Fitting to this law gives values of β ranging from 0.1 Å^{-1} to 1.4 Å^{-1}.

It is common knowledge that DNA can be treated as a one-dimensional linear chain of stacked base pairs. We believe that in the ground state every base pair contains bound electrons only. Then the charge is carried through DNA by excited electrons (or holes), which can jump between the base pairs. Below, we propose a simple model which, for our purposes, reflects basic features of the electron transport in DNA. The picture includes the following ingredients.

(i) The excited electron states at the base pairs are separated by an energy spacing larger than the temperature and therefore are hardly excited thermally.

(ii) Thermal motions of the DNA base pairs are elastic vibrations with a characteristic frequency ω_b.

(iii) Efficient charge transfer between neighboring base pairs takes place for rare events.

(iv) The Coulomb interactions between the electrons and holes can be neglected for describing the hopping transport.

Let us explain point (iii) in more detail. For the static equilibrium DNA helix charge, hopping is expected to be negligibly small, since there is no significant electronic overlapping between adjacent base pairs. Nevertheless, sometimes, due to thermal fluctuations, exclusively favorable configurations for hopping of the base pairs occur, when efficient hopping is possible. If the separation between the pairs is larger than the ampli-

[1] This article was submitted by the authors in English.

tude of their thermal vibrations, then the probability of such events (which can be called "contacts") is small. Duration of the contact can be estimated as the characteristic oscillation time ω_b^{-1}.

Now we discuss the correspondence of the assumptions listed above and experimental data. As a guideline, we use not only data known from the DNA literature but also the data obtained for a wide range of organic linear chain polymers of stacked planar molecules (for a review see [24]). The contacts are related to mutual displacements and orientations of adjacent base pairs. Probably, hopping matrix elements are mostly sensitive to the relative rotations (twist fluctuations) of the base pairs (see, e.g., [25]). The characteristic frequency of these fluctuations, ω_b, is usually estimated as being in the region 10^{11}–10^{12} s^{-1}. A small probability of the contacts is confirmed by experiment showing that the characteristic electronic hopping time τ is larger than ω_b^{-1}; in the experiments [8, 10, 17, 18] $\omega_b\tau = 10^2$–10^3. Our first assumption (i) requires $\Delta E > T$, where ΔE is the spacing, in the spectrum of electron excitations for a base pair. The magnitude of ΔE can be measured directly; for the experiments [8–23] $\Delta E > 500$ K. Therefore, the inequality is satisfied. Rough macroscopical estimations at the Coulomb interaction U_c, as well as ab initio molecular orbital calculations of U_c, give few meV [26], and thus the Coulomb energy appears to be smaller (though of the same order) than $\hbar\omega_b$. We believe that it is enough to justify neglecting the Coulomb interaction.

The above reasoning leads to a one-dimensional hopping Hamiltonian for the electrons:

$$\mathcal{H} = \hbar\sum_i (\xi_i a_i^+ a_{i+1} + \xi_i^* a_{i+1}^+ a_i). \qquad (1)$$

Here a_i and a_i^+ are electronic annihilation and creation operators at the site (i.e., the base pair) with the number i, and ξ_i are the hopping amplitudes, which are time-dependent quantities. The equations for the Heisenberg operators a_i are

$$\partial_t a_i = -i\xi_i a_{i+1} - i\xi_{i-1}^* a_{i-1}. \qquad (2)$$

We assume that different ξ_i possess independent statistics, since ξ_i are related to independent thermal pair base fluctuations. The hopping matrix element ξ_i can decompose into a constant part $\langle\xi_i\rangle$, which describes the coherent charge carrier motion in a completely rigid lattice, and a fluctuating part. Since the probability to jump is appreciable during rare events, the coherent part of ξ can be neglected in comparison with its fluctuating part.

Note that theoretical models based on hopping Hamiltonians similar to Eq. (1) are widely used to describe charge transport in solid-state physics (see, e.g., [27, 28]). For most problems, in this case the description corresponds to electron migration in a steady energy landscape, including thermally activated jumps over barriers and quantum tunneling through the barriers. This is quite different from our case.

We assume that DNA molecules can be treated as homogeneous ones. Though the molecules are constructed from four different nitrous bases, experimental data [8–22], as well as numerical first principle calculations [26, 29, 30], show that the sequence of base pairs is not a decisive factor determining electron transport in DNA. Quantitatively, this condition can be formulated as $\delta E < \hbar\omega_b$, where δE is an energy spacing between the (lowest excited) electron energy levels at different base pairs. The values of δE, known mainly from numerical electronic structure calculations [26, 29, 30], are of the order of meV. Thus, δE is smaller than $\hbar\omega_b$ for ω_b given above, which justifies the picture. In addition, some experiments (see, e.g., [23]) are performed for artificial homogeneous DNA, where $\delta E = 0$. One expects that, due to the hopping, electron diffusion occurs on large time scales. For ξ, treated as white noise, it was demonstrated in the papers [31, 32]. Though our case is essentially different, there is good reason to believe that the same behavior should be observed on time scales larger than the hopping time τ.

Below, we examine the particular case related to the fluorescence measurements reported in the papers [8–23]. The donors are photoexcited, and effects related to the excited electron motion to the acceptors are monitored. The energetic gaps δE_d and δE_a between the donor and the acceptor and the base pairs between them are crucial for the hopping rate. The values of δE_d and δE_a (known mainly from ab initio numerical calculations [15, 26, 29, 30]) can be estimated as 10^2 meV. We see that the inequalities δE_d, $\delta E_a \gg \hbar\omega_b$ are satisfied. The electron is always bound to the acceptor site more strongly than to a standard base pair, which is $\delta E_a > 0$. As for the donors, the sign of δE_d can be either positive or negative. If δE_d is negative, then the scheme of the electronic charge transfer from the donor to the acceptor is quite simple. Initially, the electron leaves the donor, jumping to the neighbor site, and then jumps between the standard base pairs, finally being trapped at the acceptor. The case $\delta E_d > 0$ is more complicated. In order to have a driving force for the donor–acceptor charge transfer process, the final state with the charge bound to the acceptor should be energetically favorable; that is, the inequality $\delta E_a > \delta E_d$ has to be satisfied. However, there are some base pairs in-between which play the role of the potential barrier for the electron. Therefore, there are two possibilities for the electron to reach the acceptor. The first possibility is for it to jump initially from the donor to the neighboring site and then to move to the acceptor by multistep hopping over the standard base pairs. The second possibility is by unistep (direct) quantum tunneling from the donor to the acceptor through the barrier.

Since $\delta E_d \gg \hbar\omega_b$, the probability for the electron to jump from the donor to the neighboring base pair due to the dynamics of ξ is negligible. At $\delta E_d > 0$, such a jump is possible if the electron absorbs a high-frequency phonon with the frequency $\omega_{ph} \sim \omega_d$ ($=\delta E_d/\hbar$). Correspondingly, at $\delta E_d < 0$, the electron jump from the donor is accompanied by emitting high frequency phonons. Such dynamical vibrations with periods as short as tens of femtoseconds (i.e., phonons with $\omega_{ph} \sim 10^{14}$ s^{-1}) were reported in the literature [33–35]. Since $\hbar\omega_{ph} > T$, occupation numbers of such phonons are small. Thus, for $\delta E_d > 0$, the probability for the electron to jump from the donor to the neighboring site contains two small factors: the probability of the contact and the probability of absorbing the high frequency phonon. This corresponds to the experimental situation where only a small fraction of the electrons are transported from the donor to the acceptor.

When the electron leaves the donor, it starts to jump between the donor and the acceptor. It can return to the donor or arrive at the acceptor. If $\delta E_d < 0$, then the probability to return to the donor is negligible. We assume that even at $\delta E_d > 0$ the probability of the electron to jump to the donor or to the acceptor is smaller than the probability to jump to the standard base pair. There are two reasons for this assumption. First, the donors and the acceptors have chemical structures different from the standard base pairs, which hinders the contacts. Second, the jump has to be accompanied by phonon emission, which diminishes its probability. The same is valid for the acceptor. Thus, before being finally trapped at the acceptor site, the electron jumps many times back and forth over the base pairs between the donor and the acceptor, "smeared out" homogeneously over all the intermediate base pairs. Then the relative probability for the electron to arrive at the acceptor is determined by the ratio of the probabilities for the electron to jump to the donor and to the acceptor from adjacent base pairs. This relative probability appears to be independent of the separation x between the donor and the acceptor. That explains why the rate of charge transfer sometimes is almost insensitive to the relative loading of donors and acceptors (see, e.g., [36, 37]). The above picture implies that the total donor–acceptor charge transfer time should be larger than the electronic hopping time τ, and this conforms to experimental data (see, e.g., [8]).

Now we consider the quantum tunneling for an electron strongly attached to the donor, which is the case for $\delta E_d > 0$. Though the potential barrier depends on time, at the condition $\delta E_d \gg \hbar\omega_b$, the probability of the electron tunneling from the donor to the acceptor can be calculated using the adiabatic approximation. To examine the tunneling process, one should consider the quasi-stationary electron state bound at the donor. In the context of our picture, we assume $\xi \ll \omega_d$. Then the energy of the bound state is close to $-\delta E_d$. Substituting ∂_t by $i\omega_d$ in Eq. (2), one obtains for the state

$$a_i = -\frac{\xi^*_{i-1}}{\omega_d} a_{i-1}, \quad i > 0; \qquad a_i = -\frac{\xi_i}{\omega_d} a_{i+1}, \quad i < 0, \tag{3}$$

where we used the condition $\xi \ll \omega_d$. Then, the probability for the electron to be at the site n is determined by the average

$$\langle a_n^+ a_n \rangle = \omega_d^{-2n} \left\langle \left| \prod_{i=1}^{n} \xi_{i-1} \right|^2 \right\rangle. \tag{4}$$

Quantum averaging and averaging over the statistics are performed upon deriving Eq. (4). In addition, at the derivation we substituted $\langle a_0^+ a_0 \rangle \approx 1$, which is justified by $\langle a_n^+ a_n \rangle \ll 1$. Note that probability (4) is determined by the simultaneous statistics of ξ. Remember that different ξ_j are assumed to be statistically independent. Therefore, the average on the right-hand side of Eq. (4) is a product of $\langle|\xi_j|^2\rangle$. For standard pairs, the quantities can be regarded as site-independent ones. Therefore, the probability of the electron being at the nearest site to the acceptor is proportional to $\langle|\xi|^2\rangle^n/\omega_d^{2n}$, where n is the number of the standard pairs between the donor and the acceptor.

The jump of the electron from the bound state to the acceptor is accompanied by phonon emission. However, the only x-dependent factor in the probability of the process is related to the average charge occupation number of a site n near the acceptor, which was established above. Thus, for the probability we obtain the exponential law $\exp(-\beta x)$ with

$$\beta = a^{-1} \ln(\omega_d^2/\langle|\xi|^2\rangle). \tag{5}$$

Here, ξ is the hopping probability for the standard base pairs and a =3.4 Å is the distance between the base pairs in DNA. Note that ω_d depends on the donor type, whereas the average $\langle|\xi|^2\rangle$ is mainly related to base pair vibrations. It follows from the above consideration that the exponential law implies the condition $\beta > a^{-1}$. This conclusion is in agreement with most published experimental data. As reported in [21], the value $\beta = 0.1$ Å^{-1} (thus smaller than a^{-1}) is probably related to an attempt to fit a complex behavior (including two processes: diffusion and tunneling) by a simple exponential law.

Let us stress that the quantum tunneling analyzed above is not the standard (static) tunneling described in textbooks. We have to deal with dynamic tunneling, which will be effective only when, due to fluctuations of ξ, there occurs some kind of bridge from the donor to the acceptor. We found that the exponential law is in fact explained by the small probability of having such a

bridge, which is realized when many contacts between base pairs occur simultaneously. In addition, the probability of this kind of tunneling is strongly dependent on the temperature via $\langle|\xi|^2\rangle$. It is natural to assume that it exponentially depends on the relative displacement u of the neighboring base pairs. Then (in the harmonic approximation), $\ln\langle|\xi|^2\rangle$ contains a term, proportional to $\langle u^2\rangle$, which is proportional to the temperature T. Thus, we arrive at the expression

$$\beta a = c_1 - c_2 T, \tag{6}$$

where c_1 and c_2 are temperature-independent factors. They can be extracted from the paper [20]: $c_1 \approx 4$, $c_2 \approx 0.01$ K^{-1}. The values are in agreement with rough estimates $c_1 \sim a/b$, $c_2 \sim k_B/M\omega_b^2 b^2$, where k_B is the Boltzmann constant, M is the base pair mass, and b is the electronic penetration length. It can be estimated as $b \sim \hbar/\sqrt{mE} \sim 1$ Å, where m is the effective electron mass and E is its binding energy at the base pair.

To conclude, for the electron which is strongly bound to the donor, we established two different charge transfer mechanisms: diffusion and tunneling. Diffusion leads to a charge transfer probability independent of the donor–acceptor distance x. However, the probability contains the small factor related to the electron jump from the donor to a neighboring site. The tunneling leads to the exponential dependence of the probability on x (with the temperature-dependent length β^{-1}). Therefore, it is not efficient for large distances. Thus, the exponential law has to be observed for small distances x, whereas for large distances the charge transfer rate has to be independent of the donor–acceptor distance. Just this kind of behavior was reported very recently [23]. For the case of an electron weakly bound to the donor, the hopping should always dominate over quantum tunneling. This explains why the rate of charge transfer sometimes does not behave exponentially even for small x [36, 37].

Note that in some cases the interaction of light, ionizing radiation, or chemically active reagents with DNA can result in the loss of an electron at a specific site with the formation of a hole. In this case, the charge transport through DNA can be provided by holes (see, e.g., [14]). The key issues for positive charge carrier transport are the same as for the electrons. As far as the physical picture of charge transport is concerned it is essentially the same for both kinds of carriers, and it can be described in the framework of the same approach.

The research presented in this publication was made possible in part by the Russian Foundation for Basic Research, project no. 00-02-17785. Fruitful discussions with A. Iosselevitch, Yu. Evdokimov, V. Golo, D. Bicout, and T. Costi are gratefully acknowledged.

REFERENCES

1. S. D. Eley and D. L. Spivey, Trans. Faraday Soc. **58**, 411 (1962).
2. J. Ladik, Acta Phys. Acad. Sci. Hung. **11**, 239 (1960).
3. H. W. Fink and C. Schonenberg, Nature **398**, 407 (1999).
4. A. Yu. Kasumov *et al.*, Science **291**, 280 (2001).
5. Y. Okahata, T. Kobayashi, K. Tanaka, and M. Shimomura, J. Am. Chem. Soc. **120**, 6165 (1998).
6. P. Tran, B. Alavi, and G. Gruner, Phys. Rev. Lett. **85**, 1564 (2000).
7. D. Porath, A. Bezryadin, S. de Vries, and C. Dekker, Nature **403**, 635 (2000).
8. M. R. Arkin *et al.*, Science **273**, 475 (1996).
9. F. D. Lewis *et al.*, Science **277**, 673 (1997).
10. P. F. Barbara and E. J. C. Olson, Adv. Chem. Phys. **107** (1999).
11. E. Meggers, M. E. Michel-Beyerle, and B. Giese, J. Am. Chem. Soc. **120**, 12950 (1998).
12. D. N. Bertrand, S. Priyadarshy, and S. M. Risser, Chem. Biol. **4**, 3 (1997).
13. C. Wan *et al.*, Proc. Natl. Acad. Sci. USA **96**, 6014 (1999).
14. P. T. Henderson, D. Jones, G. Hampikian, *et al.*, Proc. Natl. Acad. Sci. USA **96**, 8353 (1999).
15. J. Jortner, M. Bixon, T. Langenbacher, and M. E. Michel-Beyerle, Proc. Natl. Acad. Sci. USA **95**, 12759 (1998).
16. F. C. Grozema, Y. A. Berlin, and L. D. A. Siebels, Int. J. Quantum Chem. **75**, 1009 (1999).
17. D. B. Hall, R. E. Holmkin, and J. K. Barton, Nature **382**, 731 (1996).
18. D. B. Hall and J. K. Barton, J. Am. Chem. Soc. **119**, 5045 (1997).
19. M. R. Arkin, E. D. A. Stemp, S. C. Pulver, and J. K. Barton, Chem. Biol. **4**, 369 (1997).
20. A. K. Felts, W. T. Pollard, and R. A. Friesner, J. Phys. Chem. **99**, 2929 (1995).
21. K. Fukui and K. Tanaka, Angew. Chem. Int. Ed. Engl. **37**, 158 (1998).
22. C. Wan, T. Fiebeg, O. Schiemann, *et al.*, Proc. Natl. Acad. Sci. USA **97**, 14052 (2000).
23. B. Giese, J. Amaudrut, *et al.*, Science **412**, 318 (2001).
24. D. Jerome and H. Schultz, Adv. Phys. **31**, 299 (1982).
25. R. Bruinsma, G. Gruner, M. R. D'Orsogona, and J. Rudnik, Phys. Rev. Lett. **85**, 4393 (2000).
26. L. Ducasse, A. Fritsch, and F. Castet, J. Phys. IV **10**, 3 (2000).
27. J. Callaway, *Quantum Theory of the Solid State* (Academic, New York, 1974).
28. J. Appel, Solid State Phys. **21**, 193 (1968).
29. P. J. de Pablo *et al.*, Phys. Rev. Lett. **85**, 4992 (2000).
30. J. J. Ladik, Phys. Rep. **313**, 171 (1999).
31. H. Haken and P. Reineker, Z. Phys. **249**, 253 (1972).
32. H. Haken and G. Strobl, Z. Phys. **262**, 135 (1973).
33. M. B. Hakim, S. M. Lindsay, and J. Powel, Biopolymers **24**, 1185 (1984).
34. E. B. Brauns, C. J. Murphy, and M. A. Berg, J. Am. Chem. Soc. **120**, 2449 (1998).
35. N. V. Hud and M. Polak, Curr. Opin. Struct. Biol. **11**, 292 (2001).
36. C. J. Murphy *et al.*, Science **262**, 1025 (1993).
37. J. W. Evensoon and M. Karplus, Science **262**, 1247 (1993).

JETP Letters, Vol. 75, No. 1, 2002, pp. 41–54. Translated from Pis'ma v Zhurnal Éksperimental'noĭ i Teoreticheskoĭ Fiziki, Vol. 75, No. 1, 2002, pp. 44–59.

Dissipation of Strong Langmuir Turbulence in Nonisothermal non-Maxwellian Plasma

L. N. Vyacheslavov*, V. S. Burmasov, I. V. Kandaurov, É. P. Kruglyakov, O. I. Meshkov, and A. L. Sanin

Budker Institute of Nuclear Physics, Siberian Division, Russian Academy of Sciences, pr. Akademika Lavrent'eva 11, Novosibirsk, 630090 Russia

** e-mail: vyachesl@inp.nsk.su*

Received November 15, 2001; in final form, December 5, 2001

The regime of strong Langmuir turbulence characterized by the plasma nonisothermality and by the presence of an appreciable non-Maxwellian hot-electron component was experimentally studied. Turbulence was excited in the preliminary produced plasma by the relativistic electron beam. Thomson scattering of laser IR radiation served as the main diagnostic method. The spatial spectra of the Langmuir turbulence and of the attendant ion-sound turbulence were studied using Thomson collective scattering. Thomson incoherent scattering was used for studying the plasma electron distribution function and searching for the local dips of plasma density. Stark spectroscopy of turbulent microfields and the method of observation of plasma radiation at the double plasma frequency were also used. Based on the experimental data, the mechanism of Langmuir oscillation damping by plasma electrons was analyzed. The Langmuir wave conversion induced by the ion-sound turbulence is the most probable channel for energy transfer from the turbulence to plasma electrons, the low-frequency fluctuations being the direct consequence of the strong Langmuir turbulence. © *2002 MAIK "Nauka/Interperiodica".*

PACS numbers: 52.35.Ra; 52.70.Kz

1. At present, it is generally accepted that wave collapse [1] is the main mechanism of energy transfer along the spectrum of Langmuir turbulence (LT) from the long-wavelength pumping region to the short-wavelength region where the Langmuir oscillations are absorbed by plasma electrons. The essence of this mechanism is that the electron-plasma oscillations trapped by the local dips of plasma density induce an avalanche-like decrease in the size of the initial dip and lead to the simultaneous shortening of the wavelength of trapped oscillations, resulting in a decrease (at a fixed frequency) in the phase velocity. The collapse process terminates after the trapped oscillations are slowed down to an extent where they can be rapidly absorbed by plasma electrons through the Landau damping mechanism. The wave-collapse equations [1] were used in many subsequent works, where the presence of collapse in the two- and three-dimensional compression geometries was confirmed both analytically and numerically and the understanding of the physics of wave collapse was refined (see reviews [2–4]). Over the last 15 years, new numerical results have amplified the picture of the collapse-induced energy transfer mechanism and have found experimental confirmation. This is primarily the nucleation process [5] and the two-component theory of strong LT [6]. According to this theory, the collapse is preceded by the nucleation phase of trapping and accumulation of Langmuir oscillations in the dips of plasma density until the modulation instability threshold is reached by the trapped wave packets. In this case, the major part of the turbulent Langmuir oscillations is localized in the dips, which occur either in the nucleation state or at different stages of the collapse process. This theory is most frequently used for describing the strong LT, but it does not take into account some of the important effects in full measure. The key effect consists of the formation of non-Maxwellian electrons, because it is the direct consequence of the strong LT and is particularly pronounced at high levels of turbulence pumping. The presence of an external magnetic field and of the additional ion-sound turbulence, which often accompany LT in nature and in experiment, also materially complicate the theoretical analysis. For this reason, the LT picture falls far short of being studied in detail, especially in the presence of all these factors. It is worth noting that the above-mentioned effects were theoretically studied in some works that preceded publications [5, 6]. The mechanisms of strong LT suggested in these works did not take into account the leading role of wave collapse in the energy transfer. This implies the presence of a large non-Maxwellian hot-electron component [7], the ion-sound turbulence accompanying LT [8], and the presence of an external magnetic field simultaneously with the forced low-frequency density fluctuations [9]. Publications where the action of the above-mentioned mechanisms are the subject of experimental investigation are unknown to us. This fact has motivated this

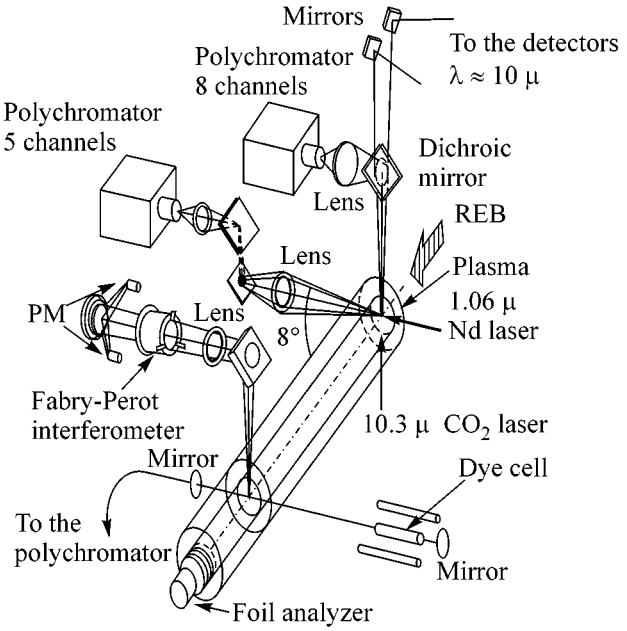

Fig. 1. Scheme of the experiment. Diagnostic section of Thomson scattering is positioned at a distance of 12 cm from the point of electron-beam injection into plasma. Spectroscopic diagnostics is at a distance of 95 cm from the point of REB injection.

work and stimulated our attempt to fill the gap in studying strong LT.

The experimental work was based on the method developed for heating dense plasma by a relativistic electron beam (REB). Under these conditions, the LT is intensively pumped and the criteria for the developed steady-state LT, for which the dimensions of the turbulent region and the turbulence lifetime far exceed all characteristic scales and times of nonlinear processes, are met rather easily. The presence of an external magnetic field is typical of such experiments, while the fast heating of plasma electrons creates conditions ($T_e \gg T_i$) which are favorable for the accumulation of weakly decaying ion-sound oscillations. Moreover, it is known from the previous work (see, e.g., [10]) that the interaction of REB with plasma is accompanied by the formation of intense superthermal "tails" in the electron distribution function. All these factors allowed us to reproduce the LT regime we were interested in.

Parameters of the experiment

Plasma	
Density	$n_e = 1–2 \times 10^{15}$ cm^{-3}
Initial temperature	$T_0 = 1$ eV
Final electron temperature	$T_e = 20–60$ eV
Magnetic field	$B_0 = 25$ kG $\omega_{pe}/\omega_{ce} = 5/1$
REB	
Density	$n_b = 3–5 \times 10^{11}$ cm^{-3} $n_b/n_e = 3–5 \times 10^{-4}$
Electron energy	$E_b = 600$ keV $E_b/T_e = 1–3 \times 10^4$
Duration	$\tau_b = 200$ ns $\tau_b\omega_{pi} = 10^4$
Diameter	$d_b = 1.8$ cm $d_b\omega_{pe}/2\pi c = 20$

The development of diagnostic techniques for the detailed study of the LT processes was the essential point in the preparation of the experiments described in this work. To accomplish this task, Thomson scattering of laser radiation was used and the appropriate diagnostic systems were devised. The other methods of investigation complementary to the Thomson scattering were also developed and used. The characteristic features of the diagnostic complexes developed for our experiments are described in section 2. The experimental setup is briefly described in the same section, where the main parameters of plasma and electron beam are also given. The experimental results on measuring the parameters of turbulent plasma are reported in section 3. The data obtained are discussed in section 4, where the pumping and absorption of Langmuir oscillations, as well as the formation and the role of the short-wavelength ion-sound turbulence, are analyzed. The main conclusions about the turbulent energy dissipation processes are formulated in section 5.

2. EXPERIMENTAL SETUP AND DIAGNOSTIC TECHNIQUE

The experimental scheme and arrangement of the diagnostic apparatus is shown in Fig. 1, while the plasma and REB parameters are given in the table. The REB is injected along the plasma column placed in a longitudinal magnetic field. To generate REB with a small angular divergence, a magnetoisolated foilless diode was devised [11]. Laser radiation in the diagnostic systems of the Thomson collective and noncollective scattering probes the plasma column at a distance of 12 cm from the point of REB injection. The details of the diagnostic system are described in [12] and briefly outlined below.

a. Thomson Scattering

Thomson scattering is well known as a powerful tool for studying plasma oscillations and the details of the electron distribution function. At the same time, this method has been used quite rarely in the experiments on the interaction of electron beams with plasmas. The Thomson collective scattering (Salpeter parameter $\alpha \gg 1$ [13]) of microwave radiation was used for the diagnostics of a Langmuir wave more than 30 years [14, 15]. Since the Bragg conditions in the microwave region can be met over a broad range of oscillation wavenumbers

only if the plasma dimensions are large enough, the Thomson scattering in the microwave region was used in the subsequent work only in the study of the ionosphere [16]. The narrow-directed electron-plasma waves were detected in the Thomson scattering experiments on the interaction of laser radiation with plasmas [17, 18], and it was only recently that publications appeared on the use of laser scattering for the measurement of the relatively broad spatial spectrum of Langmuir waves in laser-heated plasmas [19]. The collective scattering of IR lasers has also long been used for the observation of the low-frequency plasma waves [20, 21].

The Thomson incoherent scattering ($\alpha \ll 1$) is also the standard technique for measuring plasma temperature and density on many experimental setups, but only few works are devoted to the diagnostics of the nonequilibrium electron distribution functions.

Collective scattering. The Thomson collective scattering method was described in detail in [12, 22], so we will report only its most important characteristics. The radiation source is a pulsed CO_2 laser ($\lambda = 10.3$ μm, 10 J, 70–2000 ns) that can operate under collective conditions ($\alpha \gg 1$) for practically any scattering angle and, therefore, covers a broad range in the spatial spectrum of plasma oscillations of interest. The detection system was based on photoconductors and operated in the video detection mode, except for the experiment on the observation of the long-wavelength ion sound, where the wave-mixing technique was used. A notch filter cell filled with gaseous ammonia (NH_3) was used to suppress the radiation at a nonshifted frequency and to reliably separate the satellites corresponding to the scattering from the Langmuir waves. Because of this, it was rather easy to implement a system for simultaneously collecting radiation from 12 different scattering angles for multichannel detection of the **k** spectrum of electron–plasma oscillations. The diagnostics can operate in two modifications, viz. measurements of the **k** and ω spectra. To observe the ion-sound waves, two different variants of the same measurement scheme were applied, depending on the region of the spatial spectrum [12, 23]. The detection of the oscillations with small k was performed using the ammonia filter. The modification of this technique for the ion-sound frequency range required that the CO_2 laser frequency be tuned to the exact coincidence with the NH_3 absorption line and the ammonia pressure in the cell be lowered in order to reduce the filter stopband width.

Diagnostics based on Thomson incoherent scattering. The radiation source is a pulsed neodymium glass laser ($\lambda_1 = 1.06$ μm, 30–40 J, 10–60 ns; $\lambda_2 = 0.53$ μm, 15 J, 10 ns). Three different systems were used for collecting and analyzing the scattered radiation:

for measuring the temperature and density of the main plasma component in the region occupied by the turbulence (scattering angle 90°);

for the multichannel detection of the density dynamics with enhanced spatial and time resolutions (scattering angle 90°); and

for studying the non-Maxwellian part of the electron distribution function (scattering angle $\theta = 8°$).

The radiation scattered by an angle of 90° was analyzed in different experiments using one of the two detecting systems [24]. In the first of these, which was designed to measure the density and temperature of the main plasma component, the radiation was decomposed over the spectral channels using a polychromator based on the diffraction grating. The second system detected the scattered radiation integrated over the spectrum, but it had a higher aperture and better spatial and time resolutions. This system was constructed for the direct observation of small-scale dynamic dips of plasma density which appear due to the modulation instability mechanism. In these experiments, the duration of the probe pulse was specially increased to 60 ns to keep track of the density dynamics during a single laser pulse. The experimentally determined spatial resolution of a 25-channel detection system was equal to 200 μm, and the time resolution was 4 ns [25].

The use of a small scattering angle $\theta \ll 90°$ for studying the energetic but relatively low-density non-Maxwellian electrons has the following advantages over the traditional 90°-scattering scheme:

a decrease in the spectral width of the scattered radiation by a factor of $\sim\sin(\theta/2)$ increases the ratio of its spectral density to the spectral density of plasma background radiation. An additional effect of using small angles is provided by the increase in the ratio of effective volumes from which the scattered radiation and the plasma background radiation are collected. In sum, the spectral density of the scattered radiation increases relative to the spectral density of plasma light by a factor of 130 for the scattering angle $\theta = 8°$;

the small-angle scattering geometry (Fig. 2) allows one to study the angular distribution of non-Maxwellian electrons by choosing the angle ϕ for the region where the scattered radiation is detected;

a decrease in the spectral width for the scattering angle of 8° allows the use of a nonrelativistic formula with a rather high accuracy (see, e.g., [26]) in the calculation of the scattered radiation spectrum up to electron energies of ≈10 keV, thereby greatly simplifying the reproduction of the desired nonequilibrium distribution function.

A drawback of the small-angle scattering is that the spatial resolution ΔL decreases by a factor of $\sin(\theta)$. The value $\Delta L \approx 10$ mm obtained in our experiments is slightly smaller than the diameter (15–18 mm) of the region occupied by turbulence.

b. Other Diagnostic Techniques

Stark spectroscopy of turbulent microfields. While the Thomson scattering is sensitive to the fluctu-

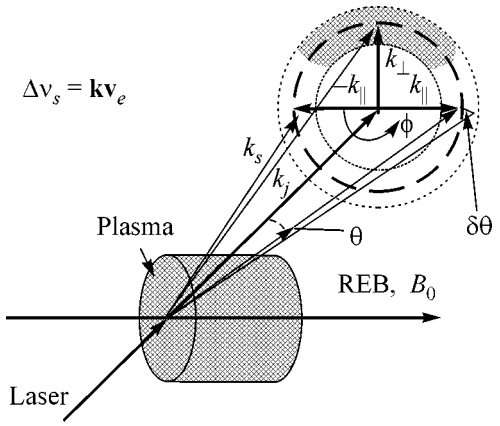

Fig. 2. Geometry of small-angle Thomson incoherent scattering. A region formed by the ends of wave vectors of the scattered radiation whose spectrum is used for the analysis of the distribution function of electrons moving at large angles to the magnetic field is hatched.

ations of the plasma refractive index, which are mainly determined by the electron-density fluctuations, the spectroscopic technique allows the detection of the changes in the spectral line profiles which are caused by the fluctuating electric fields in turbulent plasma. In the study of turbulence, the spectroscopic methods present less possibilities than the Thomson scattering, because they do not allow one to study the spatial spectra of fluctuations and place rather rigid limitations on the turbulence level above which the changes in the line profiles become strongly nonlinear, which rules out the possibility of gaining any quantitative information about the magnitudes of intense turbulent fields. Moreover, even in the linear regime, the structure of the Stark profile depends on the particular shape of the field spectrum, on the ratio of the high- and low-frequency field components, and on the presence of a magnetic field, thereby strongly hampering the interpretation of the spectroscopic data. Nevertheless, Stark spectroscopy is independent of the Thomson scattering and, hence, is of interest as a supplement to the collective laser scattering. In some publications, Stark spectroscopy served as the main tool for studying the LT in a moderately dense plasma [27, 28]. In this work, two spectroscopic methods were used [29]: emission spectroscopy and intracavity laser absorption spectroscopy. The first method has a better time resolution, whereas the second is distinguished by higher spectral and spatial resolutions. In both cases, the hydrogen H_α line was used, because it is rather intense and weakly sensitive to the quasi-static ion fields.

The method of electron absorption in thin foils for the analysis of high-energy electrons escaping from plasma. In our case, the sensitivity of the Thomson incoherent scattering technique was insufficient for studying the electrons with energies well above 10 keV. The diagnostics of such electrons was performed using their absorption in thin foils, as was done in the preceding experiments on a parametrically similar setup [30]. The essence of the method is that the electrons escaping from plasma through the exit face of the setup traverse a stack of four (in our case) thin foils. Plasma is separated from the analyzer by a separating foil. The electron currents absorbed in the foils are measured using resistors. The first measuring 9-μm-thick aluminum foil determined the lower boundary of the electron-energy resolution, which was equal to 20 keV. The signals were processed by the method close to that used for the signals of the Thomson 8°-scattering. A model energy distribution function was chosen for the incident electrons in such a way that the calculated currents from the foils most closely corresponded to their experimentally measured values. While processing data, this function was taken to be the same for different foil sets used in the measurements.

The foil analysis technique is inferior to the laser scattering method in data quality. It does not provide the spatial resolution, and its data are inevitably integrated over the plasma length. Moreover, there is an uncertainty in the interpretation of the results because of the lack of reliable data on the angular distribution of the incident electron flow. However, in spite of a considerable uncertainty, the method provides useful information about the high-energy portion of non-Maxwellian electrons.

Observation of the plasma microwave radiation. The microwave background radiation of plasmas with LT is their most frequently investigated property. In astrophysics, radio emission in certain cases is the only detected evidence of the processes occurring in turbulent plasma. In many laboratory experiments on the interaction of laser and electron beams with plasmas, the radiation near the electron-plasma frequency and its harmonics are also observed. For these reasons, we attempted to compare the experimental radiation power with the power calculated from the experimental LT spectra. This comparison can be correctly and easily carried out for the second harmonic of ω_{pe}. The spontaneous emission power at frequency $2\omega_{pe}$ is given by the expression [31]

$$\frac{dP}{d\Omega} = \frac{\pi}{2\sqrt{3}m_e n_e c} \times \int \frac{(k^2 - 2\mathbf{k}\cdot\mathbf{k}_1)^2[\mathbf{k}\times\mathbf{k}_1]^2}{k_1^2(k^2 + k_1^2 - 2\mathbf{k}\cdot\mathbf{k}_1)} W^L_{\mathbf{k}_1} W^L_{\mathbf{k}-\mathbf{k}_1} d\mathbf{k}_1 \Bigg|_{k=\sqrt{3}\omega_{pe}/c}, \quad (1)$$

where $W^L_{\mathbf{k}}$ is the experimentally measured Langmuir wave spectrum.

Under our conditions, the radiation near $2\omega_{pe}$ occurs in the submillimeter spectral region (λ = 470 μm). Because of this, it was detected using a cooled InSb-

based detector and a spectral filter comprised of three sequentially arranged copper-covered brass gratings with a 380×380 μm.

3. EXPERIMENTAL RESULTS

a. Langmuir Oscillations

The observed frequency shift of a blue satellite in the Thomson collective scattering spectrum uniquely identified plasma-density fluctuations as Langmuir oscillations [22]. Major attention in the experiments was given to the study of the spatial oscillation spectrum. The wave-vector spectra were detected for various sections of a three-dimensional spectrum in the **k** space [32]. The results of measuring along and across the region of Langmuir oscillations directly interacting with the electrons of relativistic beam are shown in Figs. 3 and 4.

A broad spectrum along the $k_\perp v_b/\omega_{pe} = 1$ line includes the waves both resonant and nonresonant to the REB (Fig. 3). A peak of resonance oscillations exceeding, at its maximum, the equilibrium level by more than 10 orders of magnitude is clearly seen in the spectrum together with a broad oscillation spectrum decreasing as k^{-4} beyond the resonance with the electron beam. The experimental data were obtained by averaging over 10 shots; the indicated error is the standard deviation.

The spectrum measured along the maximum in the resonance region is shown in Fig. 4. By tuning the angle of incidence of the laser probe radiation, the range covered along the normal wave-vector component reached two orders of magnitude, and a more than 11-order-of-magnitude excess of spectral density over the equilibrium level was detected. At $k_\perp v_b/\omega_{pe} \gg 1$, the spectrum drops as $(k_\perp v_b/\omega_{pe})^{-3.6}$. The curves fitted to the experimental points were used in the subsequent calculations involving the experimental LT spectra. In doing so, it was assumed, in accordance with the experimental data, that the spectrum of nonresonance waves was isotropic [32].

The results of Thomson collective scattering are consistent with the results of spectroscopic measurements. The duration of H_α-line broadening coincides with the duration of the REB injection into plasma and with the lifetime of the collective scattering signal (Fig. 5). It should be emphasized that the probe pulse duration (~1 μm) well exceeds the lifetime of the scattering signal. The observed broadening was close to the value $\Delta\lambda = (\lambda_{H_\alpha})^2 \omega_{pe}/2\pi c$, which is limiting for the H_α line [33] and equal to 5 Å for the plasma density $n_e = 1.5 \times 10^{15}$ cm^{-3}. It is also worthy to note that the spectral measurements were taken at the plasma column section which was situated well past the REB injection point, as compared to the section where the Thomson scattering measurements were made (Fig. 1). Special measurements showed that the intensity of resonance oscillations at this point was several times lower. A fast decrease in the broadening almost simultaneously with the termination of turbulence pumping rules out the possible explanation of this variation in the H_α-line profile by the Doppler effect.

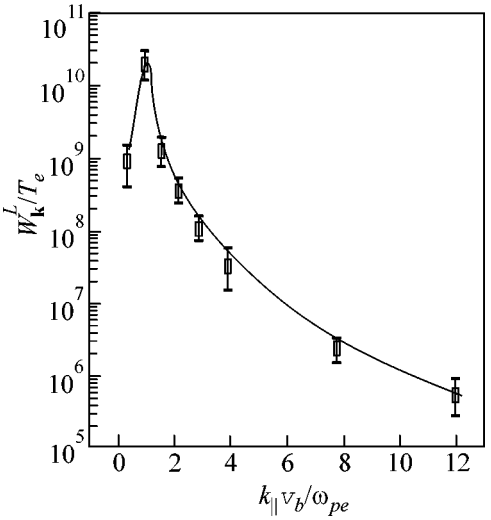

Fig. 3. Langmuir oscillation spectrum along the line $k_\perp v_b/\omega_{pe} = 1$. The curve fitted to the experimental points drops at $k_\parallel v_b/\omega_{pe} \gg 1$ as $(k_\parallel v_b/\omega_{pe})^{-4}$.

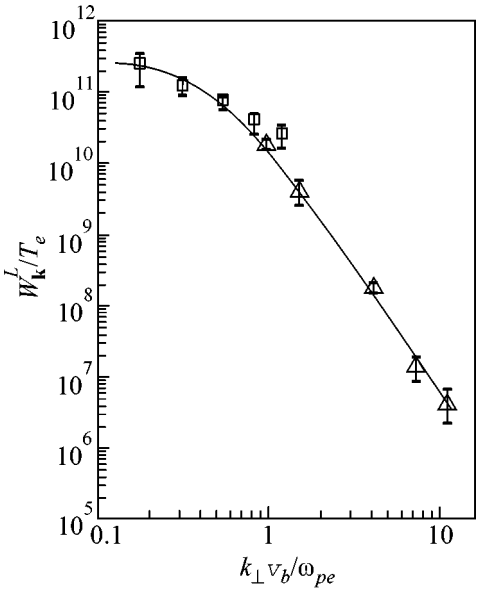

Fig. 4. Spectrum along the line $k_\perp v_b/\omega_{pe} = 1$. Angle of incidence of the laser beam to the REB direction: γ = (□) 30° and (△) 90°.

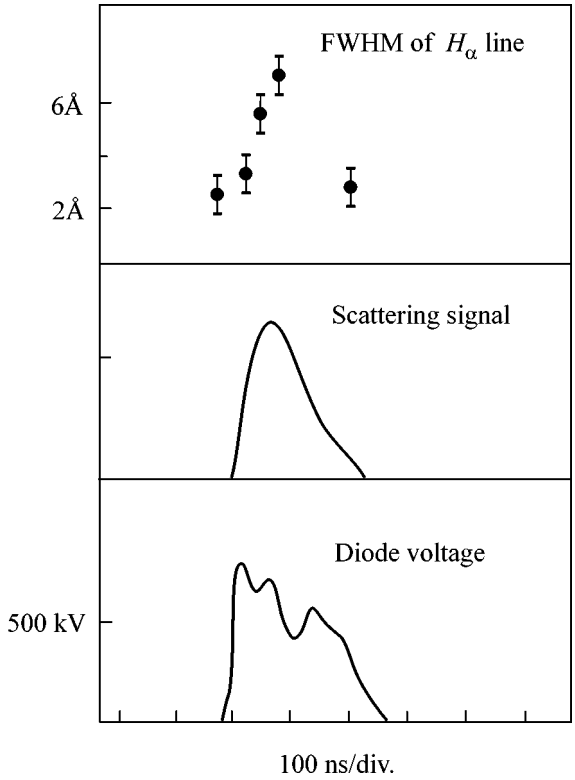

Fig. 5. Time-dependent (top) FWHM of the H_α line, (middle) scattering signal for the CO_2 laser radiation, and (bottom) voltage at the electron-beam generator diode.

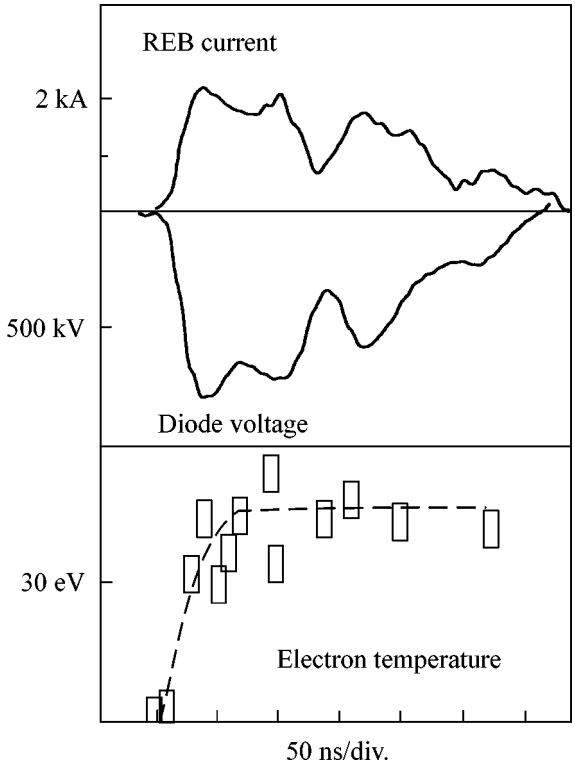

Fig. 6. Time-dependent (top) (middle) REB current, voltage at the beam-generating diode, and (bottom) temperature of the main plasma component obtained in a run of operating shots.

b. Electron Distribution Function

The temperature of the bulk of plasma electrons was measured by Thomson incoherent scattering in the course of electron-beam passage through plasma. The results of measurements, where each experimental point corresponds to a single shot, are presented in Fig. 6. One can see from the data in [32] that the electron temperature rises rapidly from 1–2 eV in the preplasma to 40–50 eV 50 ns after the REB injection began.

The spectrum of the radiation scattered by an angle of 90° at the instant the REB current reaches its maximum is shown in Fig. 7. One can clearly see the distinction between this spectrum and the Maxwellian spectrum shown in the figure by the straight line. However, we failed to get one above 500 eV for the energy of electrons detected on the 90°-detection system because of the perturbations introduced by intense background plasma radiation. Systematic studies of the nonequilibrium distribution function of plasma electrons were carried out using the 8°-scattering system, in which the background plasma radiation could relatively easily be suppressed. The densities obtained in each channel were averaged with allowance for the statistical straggling. The integrated absolute density of non-Maxwellian electrons, as determined from the scattering data, was found to be $n_h \approx 1.0 \pm 0.2 \times 10^{14}$ cm^{-3}, and their mean energy was $E_h = 420$ eV.

The overall distribution function obtained from the data of the three methods (with the 90° and 8° scattering and with the foil analyzer) is presented in Fig. 8. It turned out that the results fit best to the power law $n_h(E) \propto E^{-2.7}$ [24, 34]. This value of the exponent is close to the value obtained earlier on the other setup

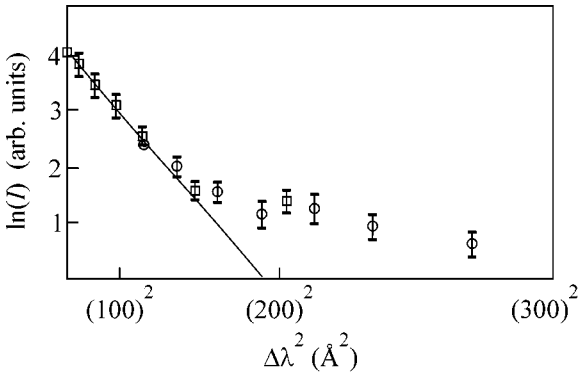

Fig. 7. Scattered radiation spectrum detected by the 90° system. The symbols □ and ○ correspond to two different shots.

under similar conditions [35]. The angular distribution of hot electrons was also analyzed using the 8° system. Except for a factor of 1.5, the distribution was found to be isotropic. The distinction between this result and the result obtained earlier under different conditions in [10], where the distribution was found to be anisotropic, is explained by the difference in the distances between the point of REB injection into plasma and the section where the Thomson scattering measurements were taken. In the experiments [10], this distance was approximately an order of magnitude larger, so that the anisotropy was probably caused by the flow of hot electrons crossing the diagnostic beam on their way from the region of the most efficient LT pumping near the REB injection section to the exit face of the system. On the other hand, virtually isotropic angular distribution of fast electrons, obtained in our experiments, need not necessarily be a consequence of their isotropic formation. The combined action of the rapid escape of electrons with velocities predominantly parallel to the REB together with the slower generation of electrons with transverse velocities because of the anisotropy of the Landau damping in a magnetic field may also lead to the experimentally observed uniform angular distribution of the accelerated electrons.

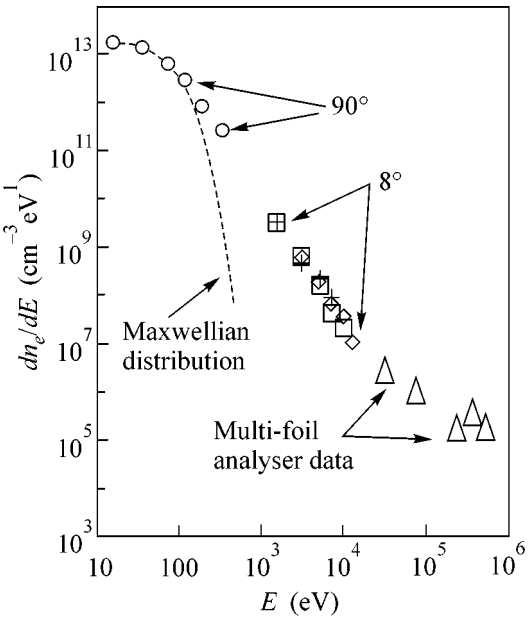

Fig. 8. Electron distribution function constructed from the data of Thomson scattering and face foil analyzer.

c. Ion-sound Turbulence

Spectral measurements for the low- frequency component of scattered radiation by the technique with an ammonia filter [23] showed that the satellite frequency was shifted by (2 ± 1) GHz. This value corresponds to the ion-sound oscillation frequency; under our conditions, it equals 1.8 GHz for a scattering angle of 14°. This frequency shift is strongly different from the frequencies of all other oscillation branches, except for the lower hybrid waves $\omega_{LH} \approx (\omega_{ce}\omega_{ci})^{1/2}$ ($\omega_{LH}/2\pi \approx$ 1.6 GHz). However, since the lower hybrid waves are excited almost normally to the magnetic field, they cannot be detected in our geometry, because it is tuned to the observation of waves propagating at an angle of 45° to the magnetic field. From this fact, it was concluded in [23] that the scattering occurs from the ion-sound oscillations.

The spatial spectrum of ion-sound oscillations [23] is shown in Fig. 9. The values on the ordinate axis are averaged over 5–7 shots. The characteristic feature of this spectrum is that the oscillation level is high and exceeds its thermal value by five orders of magnitude, while the spatial spectrum shows a maximum of $W_{\mathbf{k}}^S$ in the wavenumber region $kv_b/\omega_{pe} \approx 20$. This allows one to identify the region where the ion-sound oscillations are generated in the phase space. Despite the fact that the absolute signal value changes 2–2.5 times from one shot to another, the scatter of relative values in different shots does not exceed 20% (Fig. 9). The accuracy of the absolute value of energy spectral density is determined

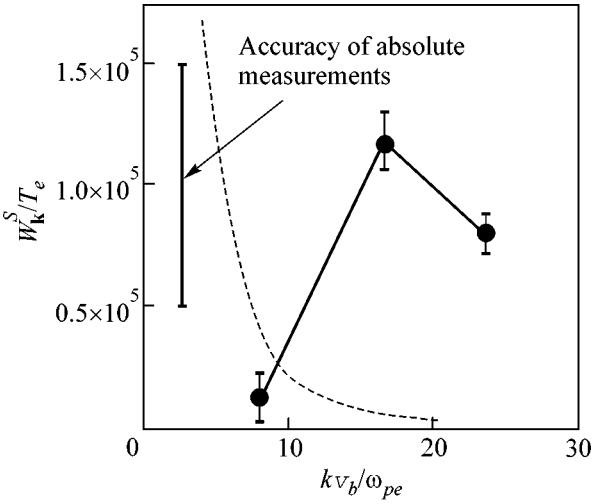

Fig. 9. Energy spectral density of ion-sound oscillations as a function of the wave vector. The dotted line is for the spectral density of ion-sound waves, as calculated for the process of Langmuir wave decay.

by the error of absolute calibration (45%). The typical $W_{\mathbf{k}}^S$ value averaged over the experimental results is $W_{\mathbf{k}}^S/T_e \approx 10^5$ at its maximum. Assuming that the ion-sound oscillations are isotropic, one obtains the value $W^S/n_eT_e \approx 1\%$ for the integrated level of detected turbulence, which corresponds to the relative low-frequency density fluctuations $\delta n_S/n_e \approx \sqrt{W^S/n_eT_e} \approx 10\%$.

4. DISCUSSION

a. Spectrum and Structure of Pumping and Absorption of Langmuir Waves

The experimentally measured Langmuir oscillation spectrum and electron distribution function can be used to analyze the angular and energy dependences of the LT energy density and of the pump and absorption power densities of Langmuir oscillations. The following general expressions were used:

$$A(\theta_m) = 2\pi \int_1^{k_{\max}} \int_0^{\theta_m} A(k, \theta) k^2 \sin(\theta) d\theta dk, \qquad (2)$$

for the integrated energy and pump power densities in the angular range 0°–θ_m about the electron beam direction;

$$A(\theta) = 2\pi \int_0^{k_{\max}} A(k, \theta) k^2 \sin(\theta) dk, \qquad (3)$$

for the spectral dependences on the angle between the wave-propagation direction and the direction of electron-beam injection; and

$$A(k) = 2\pi \int_0^{\pi} A(k, \theta) k^2 \sin(\theta) d\theta, \qquad (4)$$

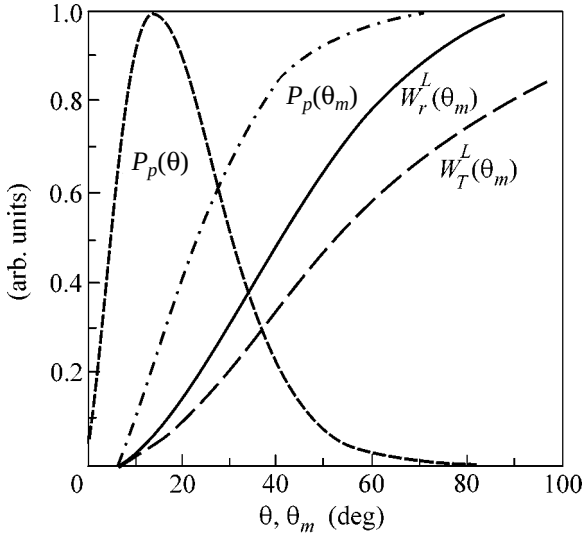

Fig. 10. Fractions of energy density of the Langmuir oscillations propagating in a cone with angle θ_m to the external magnetic field: $W_r^L(\theta_m)$ is for the resonance oscillations and $W_T^L(\theta_m)$ is for the total energy of Langmuir oscillations. The curves $P_p(\theta)$ and $P_p(\theta_m)$ are, respectively, the spectral and total pump power densities.

for the wavenumber spectrum. The resonance oscillation spectrum $W_r^L(k, \theta)$ and the total Langmuir oscillation spectrum $W_T^L(k, \theta) = W_r^L(k, \theta) + W_n^L(k, \theta)$ were obtained by fitting smooth functions to the experimental data and then used as integrands $A(k, \theta)$. The pump power was calculated using the expression $P_p(k, \theta) = W_r^L(k, \theta)\Gamma(k, \theta)$. The beam instability growth rate was not measured directly, so that it was estimated using its theoretical linear value [36]

$$\Gamma(k, \theta) = \frac{2\pi^2 e^2 \omega_{pe}}{k^2} \times \sum_{n=-N}^{N} \int d\mathbf{p} \delta(\omega_{pe} - k\cos(\theta) v \cos(\theta') - n\omega_{ce}\gamma^{-1}) \times J_n^2\left(\frac{k\sin(\theta) v \sin(\theta')}{\omega_{ce}\gamma^{-1}}\right) \times \left(\frac{1}{v}\frac{\partial f}{\partial p} + \frac{\omega_{pe}\cos(\theta') - k\cos(\theta) v}{\omega_{pe} p v \sin(\theta')}\frac{\partial f}{\partial \theta'}\right), \qquad (5)$$

where the axially symmetric electron-beam distribution function f was taken as a Gaussian distribution over the longitudinal momentum and the angle θ' with, respectively, FWHMs $\Delta p/p = 3\%$ and $\Delta\theta' = 5°$, and $N \geq 10$.

The quantity $W^L(k)$ together with the experimentally determined electron velocity distribution function $f_{ev}(v)$ can be used to obtain the power density absorbed by plasma electrons as a result of Landau damping of Langmuir waves:

$$P_d(k) = W^L(k)\gamma^L(k), \qquad (6)$$

where

$$\gamma^L(k) = \frac{\pi\omega_{pe}^3}{2k^2}\frac{d f_{ev}(v)}{dv}\bigg|_{v=\omega/k}. \qquad (7)$$

The energy content for electrons with the characteristic energy E_e was determined using the energy distribution function $f_{ee}(E)$:

$$E_a(E_e) = \int_{E_{e/1.2}}^{1.2E_e} f_{ee}(t) t dt. \qquad (8)$$

The angular dependences of the energy density of resonance waves [$W_r^L(\theta_m)$] and of the total energy density of Langmuir waves [$W_T^L(\theta_m)$] are shown in Fig. 10. It is seen from the figure that the waves propagating inside a cone with angle $\theta'_m = 53°$ to the magnetic field (cone angle 106°) account for one half of the total energy density. On the other hand, the same cone contains about 70% of the energy density of resonance

waves. Being obviously anisotropic, the spectrum of waves directly interacting with the beam is far from one-dimensional, although the latter is often used to approximate the spectrum of waves excited by an electron beam in a magnetic field. The turbulence level obtained by the integration of surfaces fitted to the experimental points W^L/n_eT_e amounts to 8% for the nonresonance waves and to 16% for the resonance waves. The total level is the sum of these values and equals 24%. The accuracy of this value is determined by the error of absolute calibration of the scattering system. Our calibration was performed with an accuracy of a multiplier of two.

One can see from Fig. 10 that the pump power is maximal for the oscillations directed at an angle of 15% to the axis. The directivity of the pump power $P_T(\theta_m)$, as determined using the value of linear increment, is narrower than the directivity of the density power of resonance waves $W_r^L(\theta_m)$. This effect can be explained both by the fact that the oscillations propagating at relatively small angles to the axis leave the resonance region in the k space faster than the other oscillations and also by the decrease in the excitation rate of these oscillations because of a small longitudinal plasma inhomogeneity. This item will be discussed in section 4c.

The spectra of pumping Langmuir oscillations and their absorption by plasma electrons are presented in Fig. 11 in arbitrary units. Two abscissa scales are used; the lower scale of the relative wavenumbers and the upper energy scale. On this scale, the wave number k corresponds to the energy of an electron with a velocity equal to the phase velocity of the wave with $v_p = \omega_{pe}/k$.

One can see from this figure that the power pumped into plasma electrons is almost constant over a rather broad interval. This picture of wave-energy dissipation in the strong LT differs appreciably from the widely accepted picture typical of Maxwellian plasma [6, 37], where only the waves with vastly greater wavenumbers are noticeably absorbed. Although the pump-power spectral density of oscillations appreciably exceeds their damping power spectral density, as is seen from the figure, the total powers integrated over the spectrum and turbulence volume prove to be close to each other and to the electron-beam power. One can see from the figure that the energy content in the hot electrons of the plasma decreases with increasing their energy. This is more likely due to the fact that hot electrons leave the observation region with higher velocity. The spectral region occupied by the Langmuir oscillations due to the waves nonresonant to REB is appreciably broader than the pump region, providing a broad interval for heating plasma electrons. The presence of a broad region of oscillations nonresonant to the electron beam signifies that there should be an efficient mechanism which provides wave transfer along the spectrum from the resonance to the nonresonance region. The modulation instability manifesting itself over the entire interval of

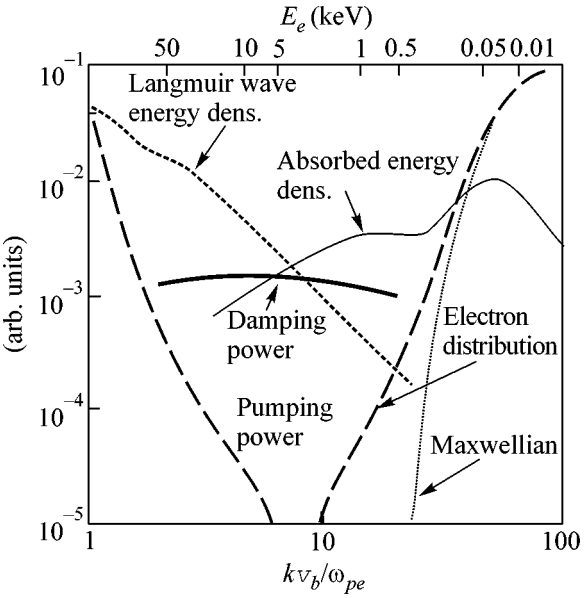

Fig. 11. Structure of pumping and absorption of Langmuir oscillations: Langmuir oscillations $W_k^L(k)$; absorbed power $P_d(k)$; pump power $P_k(k)$; electron distribution $f_{ee}(E)$; and electron energy content $E_a(E)$.

studied spatial scales $1 < kv_b/\omega_{pe} < 20$ seems to be the most probable process leading to this transfer.

Indeed, the measured spectrum of Langmuir oscillations can be characterized in terms of its stability to the modulation perturbations. This is also important for the discrimination between the strong and weak turbulence regimes. The simplest estimate $W^L/n_eT_e \gg (\omega_{ce}\omega_{pe})^2$ of the modulation instability threshold in a magnetic field is valid for the narrow spectrum and does not take into account the anisotropy of the magnetic term in the dispersion law of Langmuir oscillations and, thus, is too crude for our experiments. The most adequate approach to calculating the modulation instability threshold for a broad spectrum of Langmuir oscillations is presented in [38]. The spectrum, whose width far exceeds the modulation instability growth rate, is said to be a broad spectrum. Our case is at the boundary of the applicability of this condition:

$$\frac{1}{2}(\omega_{ce}/\omega_{pe})^2 \geq (m_eW^L/m_in_eT_e)^{0.5}, \qquad (9)$$

where $\gamma_m/\omega_{pe} \approx (m_eW^L/m_in_eT_e)^{0.5}$ is the supersonic modulation instability growth rate. Moreover, there is an additional broadening which is caused by the finite lifetime of a Langmuir wave. This gives us grounds to use the results obtained with the help of the kinetic equations for Langmuir oscillations. When determining the

modulation instability threshold, the effective temperature is introduced [38]:

$$T_{\text{eff}} = -\frac{\omega_{pe}^2}{4\pi}\int\frac{\boldsymbol{\kappa}\cdot d\mathbf{W}_{\mathbf{k}}^L/d\mathbf{k}}{\omega_{pe}\cdot\boldsymbol{\kappa}\cdot\mathbf{v}_g}d\mathbf{k}, \quad (10)$$

where $\boldsymbol{\kappa} = \mathbf{q}/|\mathbf{q}|$ is the unit vector along the disturbance propagation direction.

In the general case, T_{eff} is a complex quantity, so that the condition for modulation instability has the form $|T_{\text{eff}}| > T_e$. For the experimentally measured spectrum of Langmuir oscillations, it was shown that T_{eff} is strongly anisotropic and is maximal for the modulation perturbations directed perpendicular to the external magnetic field. This inference is valid for a broad wave spectrum and is opposite to the result obtained for the monochromatic Langmuir wave, for which the modulation instability growth rate is maximal along the field [39]. The value $(T_{\text{eff}}/T_e)_\perp \approx 30$ obtained for the relative transverse effective temperature [32] gives evidence that the modulation instability threshold is far exceeded in our case. The considerations presented in [38] apply only to the long-wavelength perturbations, $q \gg \omega_{pe}/c$. The fact that the modulation instability threshold is far exceeded in our case also follows from the well-known criterion for the threshold in plasma with a broad oscillation spectrum in the absence of a magnetic field [7]: $Q_m > 1$, where

$$Q_m = (12r_d^2\gamma)^{-1} \times 2\pi\int_0^\pi W_T^L(k,\theta)\sin(\theta)d\theta dk. \quad (11)$$

In our case, $Q_m \approx 60$ and, according to this criterion, the modulation instability threshold is far exceeded. Note that there are no limitations on the wavelength of modulation disturbance in criterion (11). In real situations, the development of modulation instability becomes even more easy because of the presence of background low-frequency plasma-density fluctuations induced by the ion-sound turbulence [40].

The LT level obtained above by the integration of the measured Langmuir oscillation spectrum can be estimated independently from the heating of the main plasma electron component. The dynamics of electron temperature is described by the equation

$$\frac{3}{2}N_e\frac{dT_e}{dt} = \frac{j^2}{\sigma} + \nu_{ei}W^L - Q_{ei}, \quad (12)$$

where j is the beam-current density, σ is the conductivity, ν_{ei} is the electron–ion collision frequency, W^L is the LT energy density, and Q_{ei} are the residual-gas ionization losses. The first term on the right-hand side accounts for the ohmic heating by return current; the latter is negligible under conditions of our experiments. The second term accounts for the electron heating due to the collisional damping of Langmuir oscillations; this term provides an independent estimate of the integrated LT level. The use of Eq. (10) for calculating the turbulence level in the first 50 ns yields the value $W^L/n_eT_e \approx 12\%$ if all possible losses are ignored. This is slightly smaller than the value obtained using Thomson scattering of the CO_2 laser radiation. However, even this level, if it had been maintained during the subsequent 100–150 ns of REB injection, would have led to a considerably greater increase in temperature than was detected in the experiment. This discrepancy can be explained by the energy expenditure on the ionization of residual gas. Indeed, measurements show that plasma density increases by 30–50% during the REB injection. Heat conduction losses do not play any significant role, as is evident from the decrease in T_e after the termination of REB injection. Note that the spectroscopic measurements suggest that plasma contains detectable carbon and other impurities. For this reason, the energy losses may also be caused by the double and triple ionization of impurity atoms. Taking into account all these facts, one finds that the time dependence of electron temperature is in a reliable agreement with the calculations. Fast electron heating and relatively slow coulombic equalization of the electron and ion temperatures (≥ 10 μs) also suggest that plasma remains nonisothermal ($T_e \gg T_i$) practically over the entire LT lifetime.

b. Mechanisms of Ion-Sound Formation

In plasma with LT, ion-sound oscillations can be excited due to the nonlinear interaction of waves. Evidence for the existence of processes typical of both strong and weak turbulence can be found in theory and in experiment [41, 42]. Three-wave decay $l_1 \longrightarrow l_2 + s$ of the Langmuir waves is the main weak-turbulence process that generates the ion-sound oscillations in nonisothermal plasma with $T_e \gg T_i$. The experimentally measured Langmuir oscillation spectrum was used to calculate the energy spectral density for the ion sound. The corresponding value was determined from the steady-state balance equation [31], in which the energy growth of ion-sound waves is due to the decay of Langmuir oscillations, while the damping is due to the absorption by the resonance particles in plasma and to the reverse coalescence process $l_1 + s \longrightarrow l_2$. In our case, the dispersion law was additionally taken into account for the Langmuir oscillations in a magnetic field. The dotted line in Fig. 9 is the energy spectral density calculated as a function of the wavenumber for the ion-sound oscillations under typical experimental conditions (H = 25 kG, T_e = 35 eV, T_i = 2 eV, and $n_e = 1.5 \times 10^{15}$ cm^{-3}). The corresponding characteristic value in the wavenumber range $kv_b/\omega_{pe} \sim 20$ was found to be $W_{\mathbf{k}}^S/T_e \approx 10^3$. This is much smaller than the value experimentally measured for the same wave vector.

Consequently, the Langmuir oscillation decay cannot be responsible for the ion-sound wave spectrum detected in the experiment.

The ion-sound oscillations can be excited as a result of the current instability of return current when injecting high-current REB into plasma. The return current arises under the action of the induction field at the instant the REB is injected into plasma, after which it flows inside the REB, provided that the current compensation condition is fulfilled. The density of return current is equal to the beam current density. The current velocity of return current is comparable to the sound velocity, suggesting that ion-sound instability can develop. To test for the possibility of the ion sound being excited by the return current, an additional experiment was conducted. In this experiment, the REB was injected into plasma through a titanium foil with a thickness of 50 μm. The beam current density in this experiment was 2–3 times higher than its value under standard conditions. Due to the foil, the angular divergence of the generated REB increases to 20°. Since the beam instability growth rate in the kinetic approximation is inversely proportional to the square of beam angular divergence, the interaction of REB with plasma becomes much less efficient. In the experiment, the intensity of beam-excited Langmuir oscillations was detected simultaneously with the energy density of ion-sound oscillations. The injection of an electron beam with large angular divergence into plasma leads to a sharp decrease in the scattering signals from both ion-sound and Langmuir oscillations. However, if the beam sound is excited by the return current, the scattering signal due to ion sound must increase with increasing REB current density. It should be noted that the degree of plasma nonisothermality was the same in both experiments to within a factor of 2. A decrease in the second term in Eq. (12) upon a decrease in the LT level was compensated to a large measure by the increase in the ohmic heating with increasing return current density. This experiment indicates that ion-sound oscillations are not excited by the back REB current.

Theoretically, the operating mode can be compared with the enhanced-current mode using the expressions for the current instability growth rate [43] and the ion damping rate [44]. The term accounting for the collisional damping [45] is also added to the damping rate. The computational results are presented in Fig. 12. One can see that the conditions for excitation of ion-sound oscillations in plasma by the return current are not fulfilled with a margin of more than an order of magnitude for the operating mode and are near the threshold for the test experiment. The inclusion of a possible current cross-sectional inhomogeneity (a factor less the 2) cannot alter the situation. In principle, the sound oscillations can be excited in the test experiment. However, it follows from the experiments reported in [46] that these oscillations are excited by the current instability in a shorter-wavelength region, so that, most probably, they

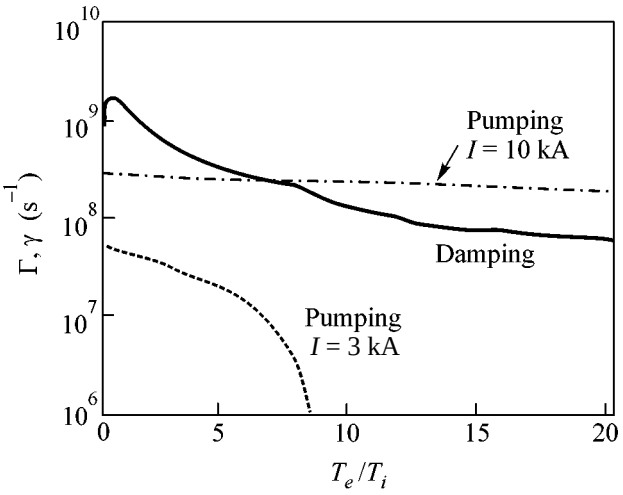

Fig. 12. Ion-sound instability pumping increments for beam currents of 10 kA (REB injection through a 50-μm titanium foil) and 3 kA (standard foilless injection), and the damping rate of the ion sound vs. the degree of plasma nonisothermality.

cannot be observed with our geometry of collective scattering.

The third source of intense ion-sound oscillations can be provided by the mechanisms characteristic of strong turbulence and associated with the nonlinear stage of modulation instability. As demonstrated at the beginning of this section, the threshold for the long-wavelength low-frequency perturbations of Langmuir oscillations is far exceeded. This may result in the transition of the modulation instability to the nonlinear collapse stage. At the collapse final stage, the Langmuir oscillations trapped into cavities are absorbed by plasma electrons, while the cavities become a source of diverging sound waves [47].

Since the LT level in our experiments is rather high, the collapse should be supersonic ($W^L/n_eT_e \gg m_e/m_i$) from almost the very beginning. For the exceeding of the threshold as considerable as that calculated above, the large-sized cavity is unstable to the short-wavelength perturbations from the very beginning and they can break the collapse development. A high LT level observed in the experiments also allows the modulation instability effect directly in the short-wavelength region at $k_{\max} \sim r_D^{-1} \sqrt{W^L/n_eT_e}$ [48]. The value of $k_{\max}$ exceeds the characteristic wavenumber of the observed short-wavelength sound more than threefold. For this reason, the modulation instability threshold is far exceeded in this region, especially when it is considered that the background density variations induced by already existing ion-sound oscillations additionally depress the instability threshold [40]. The development of modulation instability can also result in the generation of ion-sound waves even at the beginning stage, because the instability develops nonadiabatically. The transition of

the nonlinear stage of modulation instability to a full-scale collapse in this spectral region is hampered, because the absorption of oscillations by the non-Maxwellian electrons rapidly increases with wavenumber. The spectral density of the sound turbulence studied in the experiment has a maximum near $kv_b/\omega_{pe} \sim 20$. This corresponds to the maximal transfer rate of long-wavelength Langmuir oscillation to the same spectral region, where they are absorbed resonantly by the electrons with energies of ≈800 eV.

c. Spectral Transfer and Absorption of the Energy of Langmuir Oscillations

In nonisothermal plasma, the ion-sound oscillations are weakly damped and, being accumulated, also induce the short-wavelength modulation of Langmuir oscillations, thereby opening the damping channel for the fast Langmuir waves. The rate of this process, referred to as conversion by the authors of [8], is given by the expression [49, 50]

$$\gamma_c = \int\left(\frac{\delta n_S(k_S)}{n_e}\right)^2 \frac{\gamma^L(k_S)}{2}\left(\left(\frac{2\gamma^L(k_S)}{\omega_{pe}}\right)^2 + 9(k_s r_D)^4\right)^{-1} dk_S, \quad (13)$$

where k_s is the characteristic wave vector in the absorption region. The conversion growth rate $\gamma_c = 0.01\omega_{pe}$ is equal to the modulation instability growth rate $\gamma_m \approx \omega_{pe}\sqrt{(m_e/m_i)(W_T^L/n_eT_e)} = 0.01\omega_{pe}$ and is close to the maximum of the linear beam-instability growth rate $\Gamma_{\max} = 0.02\omega_{pe}$. From these estimates, it follows that the conversion can provide spectral transfer and absorption of the Langmuir oscillations excited by the electron beam. The conversion can also compete with the modulation instability, because the rates of both processes are close.

The sound-induced conversion rate of Langmuir oscillations remains unchanged along the spectrum, whereas the beam instability growth rate decreases with increasing k. This fact gave us grounds to conclude in our earlier work [32] that, under steady-state conditions, these two processes cannot be responsible for the formation of the experimentally observed spectrum. However, in the real experiment, even a small longitudinal plasma inhomogeneity should lead to the time-dependent wave vector of Langmuir oscillations and to their escape from the resonance region [51]. This effect should be particularly pronounced where the resonance region in the $k_\parallel$ direction is narrow (i.e., at small $k_\perp$), and this should lead to a decrease in the effective pumping increment in the region $k_\perp < k_\parallel$. The presence of a small plasma-density gradient in the direction from the point of beam injection into the plasma was observed experimentally. As was pointed out above, modulation instability may also play an important role in the energy transfer from the resonance region. This effect should be more pronounced for a more narrow spectrum corresponding to smaller $k_\perp$. All of these effects can substantially modify the spectral dependences of pumping and oscillation escape from the resonance region. The intense short-wavelength ion-sound turbulence discussed above and experimentally observed after publication [32] is the most important fact counting in favor of conversion.

Another mechanism of oscillation transfer from the resonance to the nonresonance spectral region can be due to the nucleation process, namely, trapping of Langmuir oscillations in the local dips of plasma density. In our case of intense ion-sound turbulence, these dynamic dips should arise as a result of the interference of chaotically distributed ion-sound waves. The characteristic wavenumber $k \approx 20$–$30\omega_{pe}/v_b$ of the trapped wave packets [6, 37] falls within the experimentally observed region of ion-sound turbulence. Due to a drastic difference between the group velocity of Langmuir waves and the sound velocity in this region ($v_g/v_s = 10$), the trapping of rapidly propagating wave packets in relatively slowly moving dips is appreciably hampered [52]. Among the additional factors destroying the localized states are the high non-Maxwellian-electron-induced damping rate of Langmuir oscillations in this region and the rather high level of low-frequency density fluctuations ($\delta n_S/n_e \approx W_T^L/n_eT_e$), resulting in the conversion-induced oscillation transfer competing with the nucleation [53].

The fact that the experimentally measured plasma background radiation power near $2\omega_{pe}$ is consistent with the spontaneous emission power of plasma calculated from the Langmuir oscillation spectrum serves as an indirect confirmation of the notion that the main portion of energy density of Langmuir waves is not trapped in the dips. The duration of the radiation pulse proved to be close to the duration of the electron beam, while the generation power [0.5 W/(cm^3 sr)] coincided, by an order of magnitude, with the theoretical estimate made using Eq. (1). This result counts in favor of the conclusion that the main portion of LT energy is not in the localized states, otherwise the radiation power would be far in excess of the spontaneous emission level [54, 55]. Equation (1) describes the quadrupole radiation corresponding to a weakly turbulent process $l + l \longrightarrow t$. In the case of the $l + l \pm s \longrightarrow t$ process, the dipolar radiation starts to dominate when the cavity sizes become $\Delta l_m < \delta n_S \pi c/n_e\omega_{pe}$ [56]. This corresponds to the sizes $\Delta l_m < 50$ μm of the bunches of Langmuir oscillations. According to the experimental LT spectrum, this spatial scale contains a negligibly small fraction of the energy density of Langmuir waves.

One more argument in favor of the absence of localized states is provided by the experiments with diagnostics of dips by Thomson incoherent scattering. These experiments did not detect dynamic dips with depths $\delta n_e/n_e = W^L/n_eT_e$ or more during the LT lifetime [24]. The parameters of the measuring setup described

in section 2 allow the detection of dips whose sizes are greater than $\Delta l_m = 200$ μm and whose lifetimes $\tau > \Delta l_m/v_s \approx 4$ ns. The corresponding spectral range $\omega_{pe}/v_b < k < 2\pi/\Delta l_m$ contains 75% of the energy density of all experimentally detected Langmuir oscillations.

5. CONCLUSIONS

An experimental technique ("cold" high-current relativistic electron beam and diagnostic methods) has been devised for the investigation of strong Langmuir turbulence under conditions of nonisothermal plasma with a considerable component of non-Maxwellian electrons.

The detailed integrated turbulence characteristics have been measured: spectra of high- and low-frequency oscillations of turbulent plasma and plasma-electron distribution function.

The spatial spectra of Langmuir oscillations demonstrate a power-law decrease toward the short wavelengths, and the hot-electron distribution function is characterized by a power-law decrease toward the higher-energy electrons. The total level of the Langmuir turbulence is $W^L/n_eT_e \approx 24\%$ and that of the short-wavelength ion-sound turbulence is $W^S/n_eT_e \approx 1\%$; the energy content in the non-Maxwellian electrons is close to that of the plasma main component, $n_eT_e \approx n_hE_h$, where $E_h \approx 400$ eV is the mean energy of the non-Maxwellian electrons.

The obtained data suggest that the main portion of the LT oscillations is not trapped in the localized states and that the main mechanism of energy transfer from the long-wavelength Langmuir oscillations to the plasma electrons consists of their conversion induced by the short-wavelength ion-sound waves.

This work was supported in part by the Russian Foundation for Basic Research (project nos. 93-02-16913, 95-02-03764, 98-02- 17788, and 01-02-17492).

REFERENCES

1. V. E. Zakharov, Zh. Éksp. Teor. Fiz. **62**, 1745 (1972) [Sov. Phys. JETP **35**, 908 (1972)].
2. A. G. Litvak, in *Reviews of Plasma Physics*, Ed. by M. A. Leontovich (Atomizdat, Moscow, 1980; Consultants Bureau, New York, 1986), Vol. 10.
3. A. S. Kingsep, Itogi Nauki Tekh., Fiz. Plazmy **4**, 48 (1983).
4. V. D. Shapiro and V. I. Shevchenko, *Basic Plasma Physics*, Ed. by A. A. Galeev and R. N. Sudan (Énergoatomizdat, Moscow, 1984; North-Holland, Amsterdam, 1984), Vol. 2.
5. G. D. Doolen, D. F. DuBois, and H. A. Rose, Phys. Rev. Lett. **54**, 804 (1985).
6. P. A. Robinson and D. L. Newman, Phys. Fluids B **2**, 2999 (1990).
7. L. I. Rudakov and V. N. Tsytovich, Phys. Rep. **40**, 1 (1978).
8. A. A. Galeev, R. Z. Sagdeev, V. D. Shapiro, and V. I. Shevchenko, Pis'ma Zh. Éksp. Teor. Fiz. **24**, 25 (1976) [JETP Lett. **24**, 21 (1976)].
9. B. N. Breĭzman and V. I. Erofeev, Fiz. Plazmy **11**, 387 (1985) [Sov. J. Plasma Phys. **11**, 223 (1985)].
10. A. V. Arzhannikov, A. V. Burdakov, V. S. Koidan, *et al.*, in *Proceedings of the International Conference on Plasma Physics, Lausanne, 1984*, p. 285.
11. V. S. Burmasov, I. V. Kandaurov, E. P. Kruglyakov, and O. I. Meshkov, IEEE Trans. Plasma Sci. **23**, 952 (1995).
12. L. N. Vyacheslavov, V. F. Gurko, V. F. Zharov, *et al.*, Fiz. Plazmy **24**, 211 (1998) [Plasma Phys. Rep. **24**, 183 (1998)].
13. J. Sheffield, *Plasma Scattering of Electromagnetic Radiation* (Academic, New York, 1975; Mir, Moscow, 1978).
14. O. Bohmer and M. Racter, Phys. Rev. Lett. **16**, 1145 (1966).
15. Yu. G. Kalinin, D. N. Lin, V. D. Ryutov, and V. A. Skoryupin, Zh. Éksp. Teor. Fiz. **55**, 115 (1968) [Sov. Phys. JETP **28**, 61 (1969)].
16. W. Birkmayer, T. Hagfors, and W. Kofman, Phys. Rev. Lett. **57**, 1008 (1986).
17. B. Amini and F. F. Chen, Phys. Rev. Lett. **53**, 1441 (1984).
18. C. E. Clayton, C. Joshi, C. Darrow, *et al.*, Phys. Rev. Lett. **54**, 2343 (1985).
19. K. L. Backer, R. P. Drake, A. M. Rubenchik, *et al.*, Phys. Rev. Lett. **77**, 67 (1996).
20. C. M. Surko, R. E. Slusher, D. R. Moler, and M. Porkolab, Phys. Rev. Lett. **29**, 81 (1972).
21. M. Kornher, G. Decker, M. Keilhacker, and F. Lindenberger, Phys. Lett. A **39**, 95 (1972).
22. L. N. Vyacheslavov, E. P. Kruglyakov, M. V. Losev, *et al.*, Rev. Sci. Instrum. **64**, 1398 (1993).
23. V. S. Burmasov, L. N. Vyacheslavov, I. V. Kandaurov, *et al.*, Fiz. Plazmy **23**, 142 (1997) [Plasma Phys. Rep. **23**, 126 (1997)].
24. L. N. Vyacheslavov, V. F. Gurko, V. F. Zharov, *et al.*, Fiz. Plazmy **24**, 223 (1998) [Plasma Phys. Rep. **24**, 195 (1998)].
25. L. N. Vyacheslavov, V. F. Gurko, V. F. Zharov, *et al.*, Preprint No. IYaF 99-25, IYaF SO RAN (Budker Institute of Nuclear Physics, Siberian Division, Russian Academy of Sciences, Novosibirsk, 1999).
26. *Radiation Processes in Plasmas*, Ed. by G. Bekefi (Wiley, New York, 1966; Mir, Moscow, 1971).
27. G. C. A. M. Janssen, E. H. A. Granneman, and H. J. Hopman, Phys. Fluids **27**, 736 (1984).
28. A. Dovrat and G. Benford, Phys. Fluids **31**, 2026 (1988).
29. L. N. Vyacheslavov, L. M. Gorbach, I. V. Kandaurov, *et al.*, Fiz. Plazmy **20**, 51 (1994) [Plasma Phys. Rep. **20**, 45 (1994)].
30. A. V. Arzhannikov and V. T. Astrelin, Prikl. Mekh. Tekh. Fiz. **6**, 3 (1979).
31. V. N. Tsytovich, *Theory of Turbulent Plasma* (Atomizdat, Moscow, 1971; Plenum, New York, 1974).
32. L. N. Vyacheslavov, V. S. Burmasov, I. V. Kandaurov, *et al.*, Phys. Plasmas **2**, 2224 (1995).
33. G. V. Sholin, Dokl. Akad. Nauk SSSR **195**, 589 (1970) [Sov. Phys. Dokl. **15**, 1040 (1970)].

34. L. N. Vyacheslavov, V. S. Burmasov, I. V. Kandaurov, *et al.*, in *Proceedings of the International Workshop "Strong Microwaves in Plasmas", Nizhni Novgorod, 1999*, Vol. 2, p. 405.
35. A. V. Arzhannikov, A. V. Burdakov, V. S. Koidan, *et al.*, in *Proceedings of the XVII International Conference on Phenomena in Ionized Gases, Budapest, 1985*, Vol. 1, p. 216.
36. B. N. Breĭzman, in *Reviews of Plasma Physics*, Ed. by B. B. Kadomtsev (Énergoatomizdat, Moscow, 1987; Consultants Bureau, New York, 1990), Vol. 15.
37. P. A. Robinson, Rev. Mod. Phys. **69**, 507 (1997).
38. R. Pozzoli and D. Ryutov, Phys. Fluids **22**, 1782 (1979).
39. V. V. Krasnosel'skikh and V. I. Sotnikov, Fiz. Plazmy **3**, 872 (1977) [Sov. J. Plasma Phys. **3**, 491 (1977)].
40. E. N. Kruchina, Fiz. Plazmy **10**, 1307 (1984) [Sov. J. Plasma Phys. **10**, 756 (1984)].
41. S. L. Musher, A. M. Rubenchik, and V. E. Zakharov, Phys. Rep. **252**, 178 (1995).
42. G. Thejappa and R. J. MacDowall, Astrophys. J. **498**, 465 (1998).
43. A. I. Akhiezer, I. A. Akhiezer, R. V. Polovin, *et al.*, *Plasma Electrodynamics*, Ed. by A. I. Akhiezer (Nauka, Moscow, 1974; Pergamon, Oxford, 1975).
44. F. Chen, *Introduction to Plasma Physics and Controlled Fusion* (Plenum, New York, 1984), Vol. 1.
45. A. F. Alexandrov, L. S. Bogdankevich, and A. A. Rukhadze, *Principles of Plasma Electrodynamics* (Vysshaya Shkola, Moscow, 1988; Springer-Verlag, Berlin, 1984).
46. R. E. Slusher, C. M. Surko, and D. R. Moler, Phys. Rev. Lett. **36**, 674 (1976).
47. Yu. S. Sigov and Yu. V. Khodyrev, Dokl. Akad. Nauk SSSR **229**, 833 (1976) [Sov. Phys. Dokl. **21**, 444 (1976)].
48. R. Z. Sagdeev, V. D. Shapiro, and V. I. Shevchenko, Fiz. Plazmy **6**, 377 (1980) [Sov. J. Plasma Phys. **6**, 207 (1980)].
49. P. K. Kaw, A. T. Lin, and J. M. Dawson, Phys. Fluids **16**, 1967 (1973).
50. E. V. Mishin and K. Schlegel, J. Geophys. Res. **99** (A6), 1391 (1994).
51. A. A. Vedenov and D. D. Ryutov, in *Reviews of Plasma Physics*, Ed. by M. A. Leontovich (Atomizdat, Moscow, 1972; Consultants Bureau, New York, 1975), Vol. 6.
52. P. A. Robinson, M. J. Wouters, and N. G. R. Broderick, Phys. Plasmas **3**, 122 (1996).
53. P. A. Robinson and G. I. de Oliveira, Phys. Plasmas **6**, 3057 (1999).
54. H. P. Freund and K. Popadopoulos, Phys. Fluids **23**, 732 (1980).
55. K. Akimoto, H. L. Rowland, and K. Popadopoulos, Phys. Fluids **31**, 2185 (1988).
56. V. I. Petviashvili and V. Ya. Yan'kov, in *Reviews of Plasma Physics*, Ed. by B. B. Kadomtsev (Énergoatomizdat, Moscow, 1985; Consultants Bureau, New York, 1987), Vol. 14.

Translated by V. Sakun

JETP Letters, Vol. 75, No. 1, 2002, pp. 5–8. From Pis'ma v Zhurnal Éksperimental'noĭ i Teoreticheskoĭ Fiziki, Vol. 75, No. 1, 2002, pp. 7–10.

On the Contribution of Three-Body Forces to *Nd* Interaction at Intermediate Energies[1]

Yu. N. Uzikov

Joint Institute for Nuclear Research, Dubna, Moscow oblast, 141980 Russia

e-mail: uzikov@nusun.jinr.dubna.su

Received November 19, 2001

Available data on large-angle nucleon–deuteron elastic scattering $Nd \longrightarrow dN$ below the pion threshold give a signal for three-body forces. The problem exists of the separation of possible subtle aspects of these forces from off-shell effects in two-nucleon potentials. By considering the main mechanisms of the process $Nd \longrightarrow dN$, we show qualitatively that in the quasi-binary reaction $N + d \longrightarrow (NN) + N$ with the final spin singlet nucleon–nucleon pair in the S-state, the relative contribution of the three-nucleon forces differs substantially from the elastic channel. It gives a new testing basis for the problem in question. © *2002 MAIK "Nauka/Interperiodica".*

PACS numbers: 25.40.Cm; 25.40.Dn; 21.45.+v

The existence of three-nucleon forces (3*NF*s) is not doubted both in the standard meson-exchange picture [1] and in chiral perturbation theory [2]. Their strength and detailed structure are still under discussion [3]. An often used model of a 3*NF* is the 2π exchange in the form called the Tucson–Melbourne (TM-3*NF*s) parametrization [1] (Fig. 1). At present, nucleon–nucleon (*NN*) forces underestimate binding energies of light nuclei [4]. The 3*NF*s allow one to partially fill the gaps. Another signal for 3*NF*s gives elastic *Nd* scattering below 200 MeV. Recent experimental and theoretical investigations [5–9] show that a rich set of spin observables in this process gives a real opportunity to study various aspects of 3*NF* effects. Therefore, the measured cross section, which is underestimated at the scattering angles $\theta_{cm} = 60°–180°$ by the data-equivalent modern *NN* forces, is excellently reproduced by three-body calculations with the TM-3*NF*s. The deuteron analyzing power A_y^d is also well reproduced [10]. However, the nucleon analyzing power A_y^p is still under discussion [11, 12]. Furthermore, the same approach fails to explain tensor analyzing powers from the precise *dp* scattering data [10]. From this observation, the authors of [10] conclude that there are deficiencies in the spin structure of the TM-3*NF*s.

However, one should note that off-shell properties of *NN* forces contribute simultaneously with the 3*NF*. The problem is that these ambiguous aspects of *NN* forces can be studied in the 3*N* or many nucleon systems only (see a recent discussion in [12]). A noticeable *NN* input dependence was observed in [10, 13]. In this connection, the authors of [13] proposed measuring the zero point of the longitudinal asymmetry in the $\vec{n}\vec{d}$ total cross section in order to get a more clear signal for 3*NF* effects. This paper is another step in that direction; namely, to separate more definitely the *NN* and 3*NF* effects in the elastic *Nd* scattering, one should investigate supplementary processes at almost the same kinematics but with a different relative role of the *NN* forces and 3*NF*s. As shown here, a substantially different

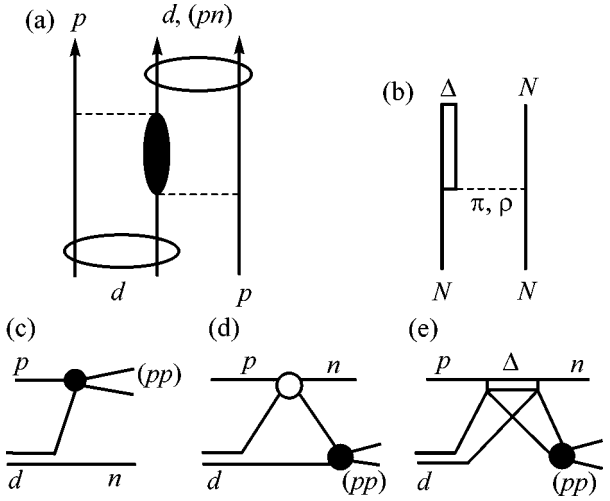

Fig. 1. Mechanisms of the reaction $p + d \longrightarrow (NN) + N$: (a) the Born 3*NF* amplitude of the $pd \longrightarrow (pn)p$ and $pd \longrightarrow dp$ reactions, (b) $\pi + \rho$ exchange for the $NN \longrightarrow N\Delta$ amplitude; (c) one nucleon exchange, (d) single scattering, (e) Δ-isobar excitation

[1] This article was submitted by the author in English.

NN-to-3*N* ratio occurs in the *pd*-interaction with the formation of the spin-singlet *NN*-pair in the final $^1S_0$ state. Here, we propose studying the reactions

$$p + d \longrightarrow (pp) + n \tag{1}$$

and $n + d \longrightarrow (nn) + p$ at a large cm scattering angle of the secondary nucleon and low relative energy of two protons (*pp*) or neutrons (*nn*)$E_{NN} < 3$ MeV, when the $^1S_0$ state dominates. Reaction (1) has not yet been investigated experimentally. At present, complete theoretical analysis of this reaction is possible at energies below the pion threshold (214 MeV) in the framework of rigorous 3*N*-scattering approaches [14, 15]. As shown by Fadeev's calculation, at initial energies below about 200 MeV, rescattering of a higher order is very important. However, around 300 MeV, the first two terms in the multiple scattering expansion are sufficient to describe the total *nd* cross section [7]. Therefore, the first Born approximation can be used as a qualitative estimation near the pion threshold. Within this approximation one cannot find the exact contribution of the 3*NF*s. Nevertheless, we can show qualitatively that the relative role of the *NN* forces and 3*NF*s differs in this reaction considerably from that in the elastic *Nd* scattering. First, using isospin invariance, we show that the Born 3*NF* amplitude (Fig. 1a) of the reaction with the singlet $pn(^1S_0)$ pair is suppressed by a factor of one-third with respect to the 3*NF* amplitude with the deuteron. However, the Born term of the one-nucleon exchange (*ONE*) mechanism (Fig. 1c), related to the *NN* forces, is not affected by isospin factors. Second, the *ONE* contribution is modified considerably due to suppression of the higher orbital momenta $l \neq 0$ in the final *NN*-system at low E_{NN}, this is not the case for the 3*NF*s. In addition, an important modification of the single scattering (*SS*) mechanism (Fig. 1d) occurs in reaction (1) in comparison with the $pd \longrightarrow dp$.

The dynamics of reaction (1) is discussed here by analogy with known mechanisms of the backward elastic pd-scattering [16, 17] (see Fig. 1). As we show below, the *ONE* + *SS* sum dominates in the $pd \longrightarrow dp$ process at energies $T_p \sim 0.2$–0.3 GeV. At higher energies $T_p = 0.4$–1.0 GeV, the double *pN*-scattering (Fig. 1e) with the Δ-excitation (Δ) gives the main contribution [16, 18]. For the $NN \rightleftharpoons \Delta N$ amplitude we use here the π + ρ exchange model [19] depicted in Fig. 1b. This model describes the measured cross section of the $pp \longrightarrow pn\pi^+$ reaction [20] in the Δ-region. Since the Δ mechanism is an important ingredient of the 3*NF* amplitude [21], we identify here the Δ contribution with the 3*NF* one. The Δ-isobar is considered as a stable baryon, that is, appropriate below the pion-production threshold.

Let us discuss the isotopic spin factors for the Born 3*NF* term of the $pd \longrightarrow (np)_{s,t}p$ amplitude depicted in Fig. 1a. The 2π exchange mechanism contains two terms corresponding to different values of the total isospin of the intermediate meson-nucleon system, $T = \frac{1}{2}$ and $\frac{3}{2}$:

$$\begin{aligned} A(pd \longrightarrow (pn)_s p) &= A^s_{T=1/2} + A^s_{T=3/2}, \\ A(pd \longrightarrow (pn)_t p) &= A^t_{T=1/2} + A^t_{T=3/2}, \end{aligned} \tag{2}$$

where the spin singlet (*s*) and triplet (*t)* states of the final pn-pair correspond to the isospin $T_{pn} = 1$ and 0, respectively. The isospin structure of the amplitudes $A^{s,t}_T$ is given by

$$\begin{aligned} A^{s,t}_T(pd \longrightarrow (pn)p) &= (2T+1)\sqrt{2(2T_{pn}+1)} \\ &\times \left(T_{pn0}\frac{1}{2}\frac{1}{2}\middle|\frac{1}{2}\frac{1}{2}\right)\begin{Bmatrix} 1 & \frac{1}{2} & \frac{1}{2} \\ 1 & \frac{1}{2} & T \end{Bmatrix}\begin{Bmatrix} \frac{1}{2} & \frac{1}{2} & T_{pn} \\ \frac{1}{2} & \frac{1}{2} & 1 \end{Bmatrix} B^{s,t}_T. \end{aligned} \tag{3}$$

The Clebsh–Gordan coefficients and 6*j*-symbols are used here in standard notations. The dynamical factor B_T in Eq. (3) does not depend on *z*-projections of the isotopic spins. Assuming the spatial parts of the singlet and triplet wave functions of the *pn* pair to be the same, i.e., $B^s_T = B^t_T$, one can find from Eq. (3) the following ratios:

$$r = \frac{A^s_{T=1/2}}{A^t_{T=1/2}} = \frac{A^s_{T=3/2}}{A^t_{T=3/2}} = -\frac{1}{3}. \tag{4}$$

After substituting Eq. (4) into Eq. (2), one finds

$$R^{iv}_I = \frac{A(pd \longrightarrow (pn)_s p)}{A(pd \longrightarrow (pn)_t p)} = -\frac{1}{3}. \tag{5}$$

We stress that, owing to Eq. (4), ratio (5) does not depend on the unknown relative phase nor on the ratio of the amplitudes $A_{1/2}$ and $A_{3/2}$ of the virtual process $\pi N \longrightarrow \pi N$ in Eq. (2). As was found in [22], the result given by Eq. (5) is valid not only for the Δ-mechanism (Fig. 1e). In fact, all intermediate states of the meson–nucleon system both for the isotopic spin $T = 3/2$ and $T = 1/2$ are taken into account in Eq. (5) including the Δ and *N** poles and the π*N* continuum. Obviously, relation (5) is valid also for the sum of the diagrams in Fig. 1a with different combinations of the isovector mesons (ππ, πρ, ρρ, …), as well as for the reaction $pd \longrightarrow dN^*$.

For the isoscalar meson exchange (ω, η, η', …), we find the ratio $R^{is}_I = 1$. The same ratio is valid for the *ONE* mechanism, $R^{ONE}_I = 1$. It is impossible to write a definite isotopic factor for the *SS*-mechanism, because

in this case the *s*/*t* ratios are different for the isoscalar ($r = 1$) and isovector $\left(r = \frac{1}{3}\right)$ *NN*-amplitudes, which are mixed with an unknown relative phase in the upper vertex of the diagram in Fig. 1d.

A detailed formalism for the amplitude of the reaction $pd \longrightarrow (NN)N$ in the framework of the *ONE* + *SS* + Δ model can be derived from the $pd \longrightarrow dp$ formalism of [16, 18]. For this aim one should make the following substitution into the matrix elements:

$$|\varphi_d\rangle \longrightarrow \sqrt{m}|\Psi_{\mathbf{k}}^{(-)}\rangle, \qquad (6)$$

where $|\varphi_d\rangle$ is the deuteron final state in the $pd \longrightarrow dp$ and $|\Psi_{\mathbf{k}}^{(-)}\rangle$ is the scattering state of the final *NN*-system at the relative momentum **k** in the $N + d \longrightarrow (NN) + N$ reaction. Since the *S*-wave gives the main contribution to the *NN*-state at $E_{NN} < 3$ MeV, one should omit the *D*-component of the final deuteron state $|\varphi_d\rangle$ in the $pd \longrightarrow dp$ formalism [16, 18] when making substitution (6). Thus, one has to insert into the upper vertex of the *ONE* diagram (Fig. 1c) the half-off-shell amplitude of *pn*-scattering in the $^1S_0$ state, $t_s(q, k)$. This amplitude, as a function of the off-shell momentum *q*, is very close in its shape to the deuteron *S*-wave function in the momentum space, $u(q)$, and has a node at the point $q \sim 0.4$ GeV/c. The node is caused by the short-range repulsion in the *NN* potential. A similar node available in the wave function $u(q)$ can be connected to the null of the deuteron charge form factor $G_C(Q)$ at the transferred momentum $Q \sim 4.5$ fm^{-1} [23]. The node of $u(q)$ has not yet been observed directly in any reactions with the deuteron due to the large contribution of the deuteron *D*-state. An important feature of reaction (1) is the possibility to display the node of the amplitude $t_s(q, k)$ directly in the cross section at T_p = 600–700 MeV and $\theta_{cm} = 180°$ [24, 25]. At initial energies 100–300 MeV, this node makes the *ONE* contribution vanishing at $\theta_{cm} = 100°$–$130°$.

The results of our calculations performed within the *ONE* + *SS* + Δ model with the Paris *NN*-potential are shown in Fig. 2 for the $pd \longrightarrow dp$ process and in Fig. 3 for reaction (1). The model describes rather well the $pd \longrightarrow dp$ cross section at T_p = 150–250 MeV and $\theta_{cm} > 120°$. The Δ(≡3*NF*) contribution strongly depends on the cutoff parameters $\Lambda_{\pi,\rho}$ in the $NN \rightleftharpoons \Delta N$ amplitude. We use here the values $\Lambda_\pi = 0.6$ GeV and $\Lambda_\rho = 0.7$ GeV obtained from the fitting of the data on $pp \longrightarrow pn\pi^+$ and $pd \longrightarrow dp$ [19, 18]. The sum *ONE* + *SS* underestimates the cross section at $\theta_{cm} = 110°$–$130°$, but this discrepancy is eliminated by adding the Δ-contribution (Fig. 2a), as was observed in [6, 21]. The calculated analyzing powers A_y^p, A_y^d, and A_{yy} are only in qualitative agreement with the data (Figs. 2b–2d).

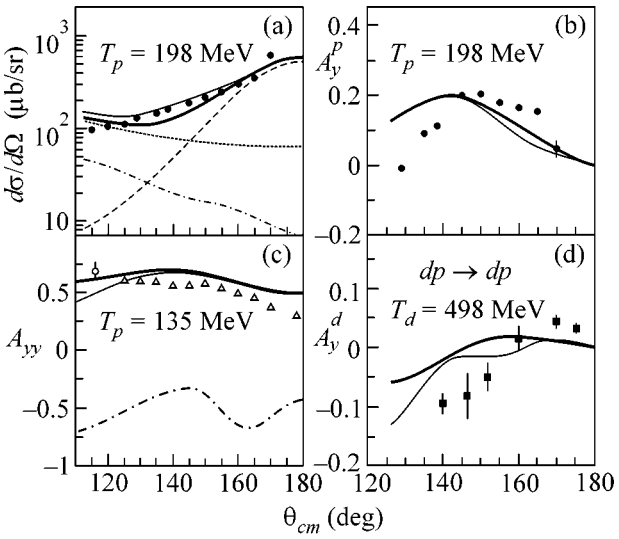

Fig. 2. The cm cross section (a) and analyzing powers A_y^p (b), A_y^d (d), A_{yy}^d (c) in the pd-elastic scattering in the backward hemisphere at different initial energies of the proton T_p and the deuteron T_d $\left(T_p = \frac{1}{2}T_d\right)$. The results of calculations with the different mechanisms are compared with the experimental data from [26] (●), [27] (filled squares), and [10] (open triangles and circles): *ONE* (dashed line), *SS* (dotted line), Δ (dashed-dotted line), *ONE* + *SS* (full thick), *ONE* + *SS* + Δ (full thin)

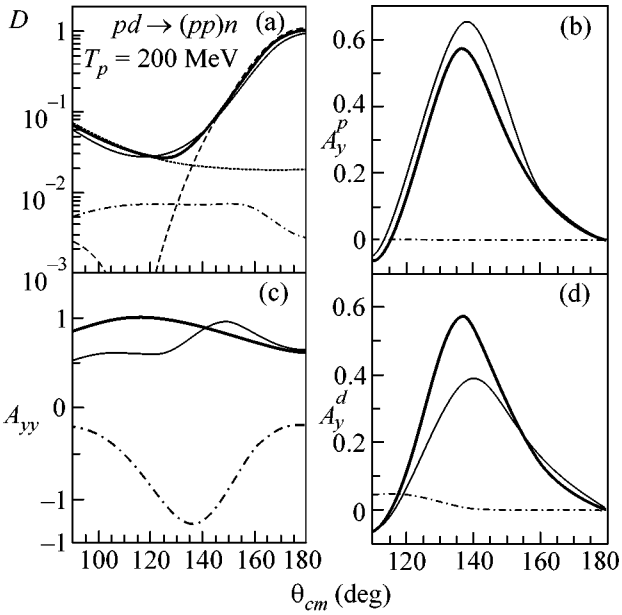

Fig. 3. The same as in Fig. 2 but for the reaction $p + d \longrightarrow (pp)_s + n$ at T_p = 200 MeV and relative energy of two protons E_{pp} = 3 MeV versus the neutron scattering angle θ_{cm}^n. $D = d^5\sigma/dp_1 d\Omega_1 d\Omega_2$ (mb/(GeV/c)sr^2).

In contrast to the $pd \longrightarrow dp$ process, the influence of the Δ mechanism in reaction (1) is rather weak in the cross section, but more pronounced in the analyzing powers (Fig. 3). At the minimum of the cross section, $\theta^n_{cm} = 120°–140°$, the role of 3*NF*s increases due to (i) vanishing of the *ONE* amplitude and (ii) a rather fast decrease of the *SS* contribution (Fig. 3a). Outside this region, the Δ contribution to reaction (1) is smaller than in the elastic *pd*-scattering owing to the isospin relations. Note, within the *ONE* + *SS* approximation, the behavior of the vector analyzing powers A^p_y and A^d_y is considerably different in reaction (1) as compared to the $pd \longrightarrow dp$ process (Figs. 3b, d). The reason is the modified structure of the *SS*-mechanism. Indeed, only the pn-scattering at small angles contributes to the upper vertex of the *SS*-mechanism in the reaction (1) [24]. On the contrary, both the charge exchange process $pn \longrightarrow np$ and the *pp* elastic scattering at small angles contribute to the $pd \longrightarrow dp$ process [16]. The Δ mechanism taken into account, in addition to the *ONE* + *SS* sum, noticeably changes the analyzing powers (Fig. 3c, 3d).

In conclusion, the *ONE* + *SS* + Δ model allows one to understand qualitatively the main features of the $pd \longrightarrow dp$ observables at $T_p \sim 200$ MeV. Within this model, we found that the relative contribution of the 3*NF*s in the reaction $N + d \longrightarrow (NN)(^1S_0) + N$ differs considerably from the elastic *pd*-scattering. A sizable modification of the analyzing powers is expected in reaction (1) in comparison to the $pd \longrightarrow dp$, in particular, due to the 3*NF* effects. Future experimental study of reaction (1) near the pion threshold and rigorous three-body calculations, complementing the process $pd \longrightarrow dp$, may give more insight into 3*NF*s.

REFERENCES

1. S. A. Coon, M. D. Scadron, P. C. McNamee, *et al.*, Nucl. Phys. A **317**, 242 (1979).
2. L. J. Friar, D. Hüber, and U. van Kolck, Phys. Rev. C **59**, 53 (1999).
3. A. Kievsky, Phys. Rev. C **60**, 034001 (1999).
4. J. Carlson and R. Schiavilla, Rev. Mod. Phys. **70**, 743 (1998).
5. H. Witala, D. Hüber, and W. Glöckle, Phys. Rev. C **49**, R14 (1994).
6. H. Witala, W. Glöckle, D. Hüber, *et al.*, Phys. Rev. Lett. **81**, 1183 (1998).
7. H. Witala, H. Kamada, A. Nogga, *et al.*, Phys. Rev. C **59**, 3035 (1999).
8. R. V. Cadman, J. Brack, W. J. Cummings, *et al.*, nucl-ex/0010006.
9. R. Bieber, W. Glöckle, J. Golak, *et al.*, Phys. Rev. Lett. **84**, 606 (2000).
10. H. Sakai, K. Sekiguchi, H. Witala, *et al.*, Phys. Rev. Lett. **84**, 5288 (2000).
11. D. Hüber and J. L. Friar, Phys. Rev. C **58**, 674 (1998).
12. L. Canton and W. Schadow, Phys. Rev. C **62**, 044005 (2000); **64**, 031001 (2001).
13. H. Witala, W. Glöckle, J. Golak, *et al.*, Phys. Lett. B **447**, 216 (1999).
14. W. Glöckle, H. Witala, D. Hüber, *et al.*, Phys. Rep. **274**, 107 (1996).
15. M. Viviani, Nucl. Phys. A **631**, 111c (1998).
16. L. A. Kondratyuk, F. M. Lev, and L. V. Shevchenko, Yad. Fiz. **33**, 1208 (1981) [Sov. J. Nucl. Phys. **33**, 642 (1981)].
17. A. Boudard and M. Dillig, Phys. Rev. C **31**, 302 (1985).
18. Yu. N. Uzikov, Fiz. Élem. Chastits At. Yadra **29**, 1405 (1998) [Phys. Part. Nucl. **29**, 583 (1998)].
19. O. Imambekov and Yu. N. Uzikov, Yad. Fiz. **47**, 1089 (1988) [Sov. J. Nucl. Phys. **47**, 695 (1988)].
20. J. Hudomaly-Gabitzsch *et al.*, Phys. Rev. C **18**, 2666 (1978).
21. S. Nemoto, K. Chmielevsky, S. Oryu, *et al.*, Phys. Rev. C **58**, 2599 (1998).
22. O. Imambekov and Yu. N. Uzikov, Izv. Akad. Nauk SSSR, Ser. Fiz. **51**, 947 (1987).
23. D. Abbott, A. Ahmidouch, H. Anklin, *et al.*, Phys. Rev. Lett. **84**, 5053 (2000).
24. O. Imambekov and Yu. N. Uzikov, Yad. Fiz. **52**, 1361 (1990) [Sov. J. Nucl. Phys. **52**, 862 (1990)].
25. A. V. Smirnov and Yu. N. Uzikov, Yad. Fiz. **61**, 421 (1998) [Phys. At. Nucl. **61**, 361 (1998)].
26. R. E. Adelberger and C. N. Brownet, Phys. Rev. D **5**, 2139 (1972).
27. J. Arvieux, S. D. Baker, R. Beutrey, *et al.*, Nucl. Phys. A **431**, 613 (1984).

JETP Letters, Vol. 75, No. 1, 2002, pp. 9–14. Translated from Pis'ma v Zhurnal Éksperimental'noĭ i Teoreticheskoĭ Fiziki, Vol. 75, No. 1, 2002, pp. 11–16.

Autowaves in Double-Wire Lines with the Exponential-Type Nonlinear Active Element

V. M. Zhuravlev

Institute of Theoretical Physics, Ul'yanovsk State University, Ul'yanovsk, 432700 Russia

e-mail: zhuravl@sv.univen.ru

Received November 1, 2001; in final form, November 23, 2001

The regimes corresponding to the appearance of localized excitation pulses in a nonlinear double-wire line with an exponential-type active element similar to that occurring in the distributed *p–n* junctions and nerve fibers are studied on the basis of exact solutions. It is shown that the line of this type is described by the nonlinear telegraph equation if there is a running inductance and by the one-dimensional nonlinear diffusion equation if it is absent. The main properties of the excitation waves and conditions for their appearance are examined. © *2002 MAIK "Nauka/Interperiodica".*

PACS numbers: 84.40.-x; 87.17.Nn; 84.30.-r; 02.30.Jr

1. Double-wire lines with an active distributed element and running parameters depending on the voltage at a given line section are frequently used as models of real distributed physical and biological systems. Examples can be provided by various waveguide systems for transmission electromagnetic microwaves and by nerve fiber, which can also be described, in a simplified form, as a double-wire line with an active element (see [1] and bibliography cited therein). The wave dynamics in such systems is highly diversified and depends on the dominance of one or another physical factor in the line. Among these are the dispersion, dissipative, and nonlinear factors or their combinations. The most impressive progress in studying the autowave models (and also of all types of nonlinear systems) was achieved in those cases where it was possible to find a way for constructing exact solutions to the equations describing the processes occurring in these models. Traditionally, these were the steady-state solutions [2, 3] and the self-similar solutions accounting for the similarity properties of these systems [1, 3]. A rich class of solutions arise if the equations can be reduced to the equations which are integrable by the method of the inverse scattering problem (ISP), for example, to the sine-Gordon (SG) equation [1, 4]. However, the ISP method does not apply if the dissipative of diffusion processes play an important role in the dynamics of the system. In these situations, one is forced to resort to the other methods of analysis. An approach of this kind was suggested in [5–7], where the method of quadratic forms was used to find exact solutions to the set of equations of the "reaction–diffusion" type, which were called the Toda diffusion chains in the cited works. For the purposes of this work, the investigation of a two-dimensional nonlinear diffusion equation (NDE2) [5]

$$u_t - D\Delta \ln u - \lambda u = 0, \tag{1}$$

was the most useful example of application of the method of quadratic forms. This equation appears in a number of hydrodynamic problems (see bibliography in [5]), and, in a more general context, it describes the models with stimulated diffusion [8]. In this work, the problem of describing waves in the nonlinear double-wire lines with a distributed active element is considered. The description of such systems is reduced to the solution of the one-dimensional nonlinear diffusion equation (NDE1) and the nonlinear telegraph equation (NTE), which is closely related to NDE1 and NDE2 (1); see below. The systems described by this equation are close to the practically encountered double-wire lines with an active element [1]. The main purpose of this work is to construct the exact solutions to the equations for the double-wire lines and analyze the wave processes occurring in them. In particular, it will be shown that these systems exhibit a number of intriguing effects.

2. The equations for the active double-wire line, whose equivalent scheme is shown in Fig. 1, can be written in the form

$$\begin{aligned} \frac{\partial i}{\partial x} + C(u)\frac{\partial u}{\partial t} + j(u) &= 0, \\ \frac{\partial u}{\partial x} + L(u)\frac{\partial i}{\partial t} + R(u)i &= 0. \end{aligned} \tag{2}$$

Here, $i = i(x, t)$ is the current at the point with coordinate x of the line at time t; $u = u(x, t)$ is the voltage at the same section of the line; $C(u)$ and $L(u)$ are the running capacitance and inductance of the line, respectively; $R(u)$ is the running resistance depending on the voltage at this section; and $j = j(u)$ is the current–voltage characteristic of the active element. The corresponding scheme of the line is shown in Fig. 1.

0021-3640/02/7501-0009$22.00

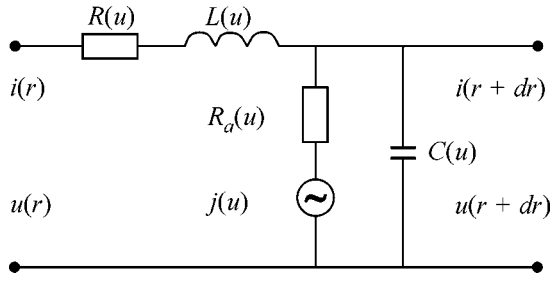

Fig. 1. Equivalent scheme of a double-wire line with active element.

Let us consider a model of physical processes for the situation where the voltages and currents are such that the running parameters R, C, and L are constant along the line and independent of the voltage at a given section. The current–voltage characteristic of the active element can often be approximated by the exponential function

$$j(u) = re^{u/u_0} - j_0. \tag{3}$$

The current–voltage characteristic of this type is typical of the p–n junctions and biological membranes in certain regimes of their functioning (see [1, 9] and bibliography cited therein). Note that, at room temperature, $u_0 = kT/e \sim 25$ mV for both p–n junctions and biological membranes (e is electron charge, k is the Boltzmann constant, and T is absolute temperature) [1, 9].

After the elimination of current i in the linear running element of the line, the line equation obeying Eqs. (2) can be written as

$$\left(\frac{\partial^2}{\partial x^2} - LC\frac{\partial^2}{\partial t^2}\right)u + Rj(u) + (RC - j'(u))\frac{\partial u}{\partial t} = 0.$$

The equation in this form makes allowance for the nonzero running inductance in the line. The authors of [11–13] suggested that it can be applied to the biological membranes (see also [1]). Substituting the expression for $j(u)$ from Eq. (3) into this equation, one gets

$$\left(\frac{\partial^2}{\partial x^2} - \frac{1}{V_0^2}\frac{\partial^2}{\partial t^2}\right)u + Rre^{u/u_0} - Rj_0 + \left(RC - \frac{r}{u_0}e^{u/u_0}\right)\frac{\partial u}{\partial t} = 0. \tag{4}$$

The quantity $V_0 = 1/\sqrt{LC}$ is equal to the wave velocity in the linear hyperbolic regime. We are mainly interested in the case for which the quantities RJ_0 and RC in Eq. (4) can be ignored compared to the exponential terms in the corresponding coefficients. The quantity $1/RC$ is the duration of a discharge through the resistance R for a capacitor with capacity C. The neglect of RC means that the discharge mainly proceeds not through the resistance of the line but through its active element. The quantity Rj_0 is the voltage drop on the resistance owing to the back conduction current. Both these quantities may be turned small by choosing the appropriate line operating point. Physically, this corresponds to a constant positive bias between the line wires. In the equations, this bias is equivalent to the substitution $u = \tilde{u} + U_0$, where $U_0 = \text{const}$. In this case, the equations do not change their form:

$$\left(\frac{\partial^2}{\partial x^2} - \frac{1}{V_0^2}\frac{\partial^2}{\partial t^2}\right)u + Rre^{U_0/u_0}e^{u/u_0} - Rj_0 + \left(RC - \frac{r}{u_0}e^{U_0/u_0}e^{u/u_0}\right)\frac{\partial u}{\partial t} = 0. \tag{5}$$

Here the sign ~ is omitted. Inasmuch as this transformation leads to the appearance of the dimensionless multiplier $m = \exp\{U_0/u_0\}$ in the corresponding coefficients, the conditions $Rrm \gg Rj_0$ and $rm/u_0 \gg RC$ can be fulfilled through the appropriate choice of U_0. This justifies the possibility of the above approximation being used for a double-wire line with the active element of type (3). Note that, because the multiplier m increases exponentially, these conditions can be met even if U_0 exceeds u_0 only by a factor of two or three. In this case, $m \sim 10$–20. The line operating regime with $m \gg 1$ will be called active regime. For large negative voltages, the current through the active element becomes close to the back conduction current. This regime will be called inactive regime. In this case, Eq. (5) becomes equivalent to the conventional telegraph equation. As in the case of the regime with the active element, the line with small RC operates in the hyperbolic regime obeying the D'Alembert equation. This fact should be particularly emphasized. It will be shown in what follows that, in the active regime, the pulses generated in the line can propagate to the region where the line operates in the inactive regime close to the hyperbolic one. However, the main property of the hyperbolic regime is that the wave dynamics is dispersionless. In this regime, the pulse propagates without severe distortions. Therefore, since the approximation considered relates only to a certain isolated section of a line operating in the active regime, it can be adjusted to the line as a whole by matching the solutions obtained below with the solutions corresponding to the inactive regime and obeying either the D'Alembert or the telegraph equation.

The approximation corresponding to the active regime is of interest, because it allows the use of methods for analysis which were already developed for Eq. (1) in [5]. As for the equation describing a physical situation, where one cannot set $RC \sim 0$ and $Rj_0 \sim 0$, it does not possess special properties and does not allow one to use the superposition principle considered below. The dynamics of such systems is more complicated.

Let us transform Eq. (4) by introducing the dimensionless conical coordinates

$$\xi = (x + V_0 t)x_0^{-1}, \quad \eta = (x - V_0 t)x_0^{-1},$$

where V_0 is the wave velocity in the linear approximation and x_0 is the characteristic length scale of the line. After introducing the new auxiliary function ϕ and setting $u(x, t) = -u_0 \ln\phi$, the equation of the model in these variables takes the form

$$D\frac{\partial^2}{\partial\xi\partial\eta}\ln\phi - \frac{\Lambda}{\phi} + \frac{1}{\phi^2}\left(\frac{\partial\phi}{\partial\xi} - \frac{\partial\phi}{\partial\eta}\right) = 0. \qquad (6)$$

In what follows, this equation is referred to as NTE. In this model, the constant dimensionless parameters Λ and D are related to the parameters of the model by

$$\Lambda = \frac{Rx_0}{V_0}, \quad D = \frac{4u_0}{x_0 r V_0}.$$

Note that the model considered is also of interest for the case where the running inductance is small and can be ignored. In this case, the NTE will be not the telegraph equation but the NDE1. As was pointed out above, it is these models which were originally considered as mathematical models of nerve fiber, and only after the publication of works [11–13] were the models modified so as to include inductance.

3. The multiplication of the simplest types of solutions for the systems considered will be performed by the method based on the special superposition principle analogous to that found in [5] for Eq. (1). We demonstrate this superposition principle by the example of two different solutions to Eq. (6). Let ϕ_1 and ϕ_2 be two linearly independent solutions of this equation:

$$D\frac{\partial^2}{\partial\xi\partial\eta}\ln\phi_i - \frac{\Lambda}{\phi} + \frac{1}{\phi_i^2}\left(\frac{\partial\phi_i}{\partial\xi} - \frac{\partial\phi_i}{\partial\eta}\right) = 0, \quad i = 1, 2.$$

By combining equations for ϕ_1 and ϕ_2, one obtains

$$D\frac{\partial^2}{\partial\xi\partial\eta}\ln(\phi_1\phi_2) - \Lambda\left(\frac{1}{\phi_1} + \frac{1}{\phi_2}\right)$$
$$-\left(\frac{\partial}{\partial\xi} - \frac{\partial}{\partial\eta}\right)\left(\frac{1}{\phi_1} + \frac{1}{\phi_2}\right) = 0.$$

Let us assume that the condition

$$\phi_1 + \phi_2 = f(\xi)g(\eta), \qquad (7)$$

where $f(\xi)$ and $g(\eta)$ are arbitrary differentiable functions of a single argument (ξ and η, respectively), is fulfilled. Then, taking into account that

$$\frac{\partial^2}{\partial\xi\partial\eta}\ln(f(\xi)g(\eta)) = 0,$$

one finds that the function

$$\Phi = \phi_1\phi_2/(\phi_1 + \phi_2)$$

satisfies the same Eq. (6):

$$D\frac{\partial^2}{\partial\xi\partial\eta}\ln\Phi - \frac{\Lambda}{\Phi} + \frac{1}{\Phi^2}\left(\frac{\partial\Phi}{\partial\xi} - \frac{\partial\Phi}{\partial\eta}\right) = 0.$$

The function Φ satisfies condition

$$1/\Phi = 1/\phi_1 + 1/\phi_2,$$

which represents the superposition principle with constraint (7). Furthermore, by analogy with the nonlinear diffusion equation (1) [5], this superposition principle can be generalized by considering r linearly independent solutions ϕ_i ($i = 1, \ldots, r$) to the initial Eq. (6), which satisfy the condition

$$\sum_{k=1}^{r}\prod_{i=1,\,k\neq i}^{r}\phi_i = f(\xi)g(\eta). \qquad (8)$$

If this condition is met, then the function Φ related to ϕ_i by

$$\frac{1}{\Phi} = \sum_{i=1}^{r}\frac{1}{\phi_i}, \qquad (9)$$

is again the solution to the initial equation. The number r will be called the rank of the superposition solution.

4. For the superposition principle to be practically implemented, it is necessary that there should be solutions obeying conditions (7) and, in the more general case, conditions (8). Such simplest solutions can be found within the framework of the method of quadratic forms suggested in [5–7]. The solutions found in this way may be of two types. The first of these can be represented in the form

$$\phi = -D\Lambda BCe^{\Lambda(\xi-\eta)} + Be^{\Lambda\xi} + Ce^{-\Lambda\eta}, \qquad (10)$$

where B and C are the arbitrary real constants. Solution (10), when recalculated for the voltage u in the line, is nonsingular if ϕ has no zeros in the whole domain of definition. This condition is met if the inequalities $B > 0$, $C > 0$, and $\Lambda < 0$ are simultaneously fulfilled.

The second, more complex, type of solution can be represented in the form

$$\phi = -DBC\Lambda\exp\{2\Lambda\xi - \Lambda\eta\}$$
$$-\frac{B}{4DC\Lambda}\exp\{2\Lambda\xi + \Lambda\eta\} \qquad (11)$$
$$+ B\exp\{2\Lambda\xi\} + C\exp\{-\Lambda\eta\},$$

where B, C, and Λ are real constants. This solution is nonsingular, e.g., if $\Lambda < 0$, $B > 0$, and $C > 0$. Another domain of parameters where the solution for the voltage is nonsingular can easily be found if it is represented in the following form:

$$\phi = B\exp\{2\Lambda\xi\}(1 - \cosh\{\Lambda\eta + \chi\})$$
$$+ C\exp\{-\Lambda\eta\},$$

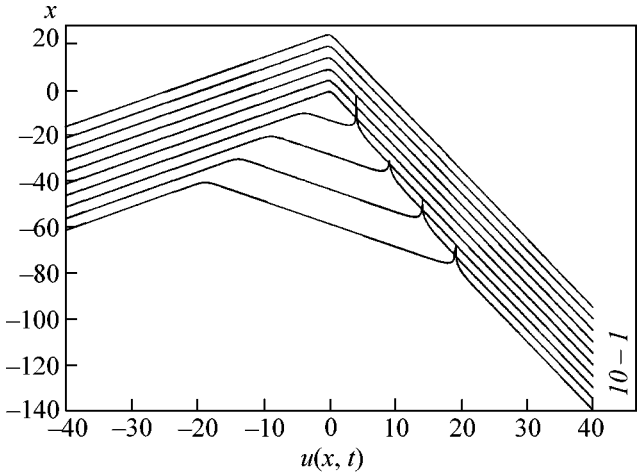

Fig. 2. Voltage distribution along the line for the solution of Eq. (11).

where $\chi = \ln\{2DC\Lambda\}$. It follows that this solution is also positive if $B < 0$ and $C > B$, provided that $C\Lambda > 0$.

Although the superposition solutions can be constructed for both classes of simple solutions, nevertheless, the solutions of the second type are of the greatest interest. The solutions of the first type describe the voltage evolution without appearance of the autowave pulse. The graphs of solutions of the second type demonstrate that the autowave pulse appears if the critical voltage level is reached at a certain point of the line. The graphs of these solutions are presented in Fig. 2, where the instantaneous voltage distributions are shown for $B = -1$, $C = 2$, $\Lambda = 1$, $D = 0.1$, and $V = 0.5$ and the successive instants of time from (*1*) $t = -50$ to (*10*) $t = 40$ with the step $\Delta t = 10$. Initially, there are two regions with almost constant voltage gradients. Then, after the pulse is formed, a new region is formed between the point of pulse generation and the running point. The voltage gradient in this region is almost constant, and the size of this region is equal to the distance traversed by the pulse. It is worth noting that the pulse is generated in the region where the voltage is close to zero. This corresponds to the active region, according to the classification given above. Then, the pulse propagates to the region with large negative voltages, i.e., to the region with hyperbolic regime. The dynamics in this region is described by the telegraph equation and, thus, can be analyzed only after solving this equation. Next, one should match both solutions. This procedure is rather cumbersome and is not considered in this work.

5. The superposition solutions enable one to obtain the models with a more complex autowave dynamics in the line. Let us first consider the superposition solutions of the first type.

For concision, we introduce notation $X = e^{\Lambda\xi}$ and $Y = e^{-\Lambda\eta}$. Let us consider r solutions of type (10). For a fixed value of parameter Λ, they take the following form:

$$\phi_i = -A_iXY + B_iX + C_iY, \quad i = 1, \ldots, r, \qquad (12)$$

where $A_i = D\Lambda B_iC_i$. For $r = 2$, the condition for existence of the superposition solution is given by Eq. (7). For this relationship to be satisfied, it is sufficient that one of the following algebraic conditions is satisfied:

$$C_1 = -C_2; \qquad (13)$$

$$B_1 = -B_2. \qquad (14)$$

Let the first of these conditions be met; then the superposition solution has the following form:

$$\Phi = \frac{\phi_1\phi_2}{\phi_1 + \phi_2} = \frac{[D\Lambda B_1C_1XY + B_1Y + C_1Y][-D\Lambda B_2C_1XY + B_2Y - C_1Y]}{X[(B_2 + B_1)C_1D\Lambda Y + B_1 + B_2]}. \qquad (15)$$

If the second condition is chosen, the solution has a similar form, in which X is replaced by Y and Y is replaced by X. Let us consider two particular cases of this general formula. The first case corresponds to the situation where both conditions (13) and (14) are met. In this case, the superposition solution takes the form

$$\Phi = \frac{\phi_1\phi_2}{\phi_1 + \phi_2} = \frac{[D\Lambda B_1C_1XY]^2 - [B_1X + C_1Y]^2}{[2B_1C_1D\Lambda XY]}. \qquad (16)$$

One more variant of the solution corresponds to the situation where C_1, C_2, B_1, and B_2 are the complex constants. If one chooses $C_1 = i\kappa = -C_2$ and $B_2 = B_1^* = \alpha + i\beta$ (the asterisk * denotes complex conjugation), then the solution will be real and take the following form:

$$\Phi = \frac{|D\Lambda B_1C_1XY + B_1Y + C_1Y|^2}{X[2\beta\kappa D\Lambda Y + 2\alpha]} = \frac{(-D\Lambda\beta\kappa XY + \alpha X)^2 + (D\Lambda\alpha\kappa XY + \beta X + \kappa Y)^2}{X[2\beta\kappa D\Lambda Y + 2\alpha]}. \qquad (17)$$

The superposition solutions of ranks $r > 2$ are constructed in an analogous way.

The superposition of the solutions of the second type gives new solutions describing more intriguing

regimes of autowave propagation in the lines. To obtain them, it is necessary to consider r solutions of type (11):

$$\begin{aligned}\phi_i &= -DB_iC_i\Lambda\exp\{2\Lambda\xi - \Lambda\eta\} \\ &\quad - \frac{B_i}{4DC_i\Lambda}\exp\{2\Lambda\xi + \Lambda\eta\} \\ &\quad + B_i\exp\{2\Lambda\xi\} + C_i\exp\{-\Lambda\eta\}, \\ &\quad i = 1, \ldots, r.\end{aligned} \tag{18}$$

For $r = 2$, the coefficients C_1 and C_2 satisfy the following relations:

$$C_1 = -C_2 = C.$$

The coefficients B_1 and B_2 remain arbitrary. The superposition solutions corresponding to $r = 2$ can be written in the form

$$\begin{aligned}\Phi &= \phi_1\phi_2\exp\{2\Lambda\xi\} \\ &\times\left\{\left[-DC\Lambda\exp\{-\Lambda\eta\} - \frac{1}{4DC\Lambda}\exp\{\Lambda\eta\}\right]\right. \\ &\left.\times(B_1 - B_2) + B_1 + B_2\right\}^{-1}.\end{aligned} \tag{19}$$

Among these solutions, there is a real solution with purely imaginary parameter $C = ik$ and real $B_1 = B_2 = b$.

One of the graphs corresponding to the nonsingular solution of Eq. (19) is shown in Fig. 3. Contrary to the solution shown in Fig. 2, the solution consists initially of three regions with almost constant voltage gradients. As in the preceding case, the pulse is generated when the voltage in the maximum becomes zero. In the figure, the instantaneous distributions in the line are given for $B_1 = -3$, $B_2 = -4$, $C = 2$, $\Lambda = 1$, and $D = 0.1$ and successive instants of time from (*1*) $t = -40$ to (*9*) $t = 40$ with step $\Delta t = 10$.

The superposition solutions with ranks $r = 3$ and 4 for the first type and, at least, with $r = 3$ for the second type can be obtained in a similar manner. For higher ranks, the set of equations for the constant coefficients of simple solutions proves to be overdetermined. Because of the nonlinearity of this system, one cannot prove, without additional analysis, whether the superposition solutions with $r > 4$ exist or not.

6. The obtained exact solutions give an indication of the new autowave phenomena, which can occur in real systems and are modeled in this work by the active double-wire lines. As is mentioned above, the model suggested accounts for the behavior of the line only in the region of the active regime and cannot be related to the whole line. However, the pulses are generated precisely in this region, after which they are channeled through the regions operating in the inactive hyperbolic mode. The pulse generation and its transformation upon

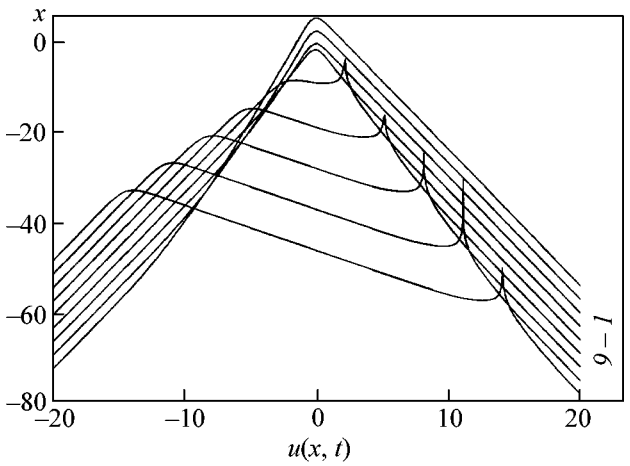

Fig. 3. Voltage distribution along the line for the superposition solution of rank $r = 2$.

reaching certain critical values of line parameters (in the case at hand, these are the global voltage minima) are typical of the autowave systems. At certain conditions, these phenomena can adequately model the phenomena accompanying the functioning of biological membranes and nerve fiber. These processes can be regarded as elements of regulator mechanisms in biological systems. Indeed, the pulse generated in the line signalizes that the voltage at a certain point of the line reached the minimal or the maximal (depending on the particular situation) critical value. The pulse movement in the line is accompanied by the formation of a new region with an almost constant voltage gradient between the point where the pulse was generated and its running position; i.e., the system "remembers" the point where the pulse arose. The more complex phenomena corresponding to the solutions of ranks $r > 2$, which were not considered in this work, are also possible. We note in conclusion that the obtained solutions demonstrate the possibility of the technical implementation of pulse generators operating according to the model considered in this work. As was pointed out in item *1*, the double-wire lines can be implemented on the basis of distributed *p–n* junctions.

This work was supported in part by the Russian Foundation for Basic Research, project no. 00-01-00260.

REFERENCES

1. A. Scott, *Active and Nonlinear Wave Propagation in Electronics* (Wiley, New York, 1970; Sov. Radio, Moscow, 1977).

2. Yu. N. Svirzhev, A. A. Gigauri, and V. N. Razzhevatkin, in *Nonlinear Waves. Self-organization*, Ed. by A. V. Gaponov-Grekhov (Nauka, Moscow, 1983), p. 32.

3. A. A. Samarskiĭ and A. P. Mikhaĭlov, *Mathematical Modeling* (Nauka, Moscow, 1997).
4. S. P. Novikov, S. V. Manakov, L. P. Pitaevskii, and V. E. Zakharov, *Theory of Solitons: the Inverse Scattering Method* (Nauka, Moscow, 1980; Consultants Bureau, New York, 1984).
5. V. M. Zhuravlev, Teor. Mat. Fiz. **124**, 3 (2000).
6. V. M. Zhuravlev, Pis'ma Zh. Éksp. Teor. Fiz. **65**, 285 (1997) [JETP Lett. **65**, 300 (1997)].
7. V. M. Zhuravlev, Zh. Éksp. Teor. Fiz. **114**, 1897 (1998) [JETP **87**, 1031 (1998)].
8. Ya. A. Fedotov, *Principles of Physics of Semiconductor Devices* (Sov. Radio, Moscow, 1964).
9. V. I. Talanov, in *Nonlinear Waves. Self-organization*, Ed. by A. V. Gaponov-Grekhov (Nauka, Moscow, 1983), p. 47.
10. M. Elsenberg, J. E. Hall, and C. F. Mead, J. Membr. Biol. **11**, 1 (1973).
11. H. M. Leiberstein, Math. Biosci. **1**, 45 (1967); **1**, 181 (1967).
12. S. W. Brady, Proc. Jpn. Acad. **39**, 721 (1963).
13. C. D. Isaacs, Math. Biosci. **7**, 305 (1970).

Translated by V. Sakun